EMPIR – 14IND02 PlanarCal

Best Practice Guide for Planar S-Parameter Measurements using Vector Network Analysers

Uwe Arz, Thorsten Probst, Karsten Kuhlmann, **PTB**
Nick Ridler, Xiaobang Shang, **NPL**
Faisal Mubarak, **VSL**
Johannes Hoffmann, Michael Wollensack, Markus Zeier, **METAS**
Gia Ngoc Phung, Wolfgang Heinrich, **FVB**
Konstantin Lomakin, Gerald Gold, Klaus Helmreich, **FAU**
Roger Lozar, **FhG**
Gilles Dambrine, Kamel Haddadi, **Univ-Lille1**
Marco Spirito, **TUD**
Roland Clarke, **ULE**

The EMPIR initiative is co-funded by the European Union's Horizon 2020 research and innovation programme and the EMPIR Participating States

`https://planarcal.ptb.de`

September 2018

This Guide has been produced within the EURAMET project entitled *Microwave measurements for planar circuits and components*. More information about this collaborative research project can be found on the project's website `https://planarcal.ptb.de` .

Disclaimer

Any mention of commercial products within this Guide is for information only; it does not imply recommendation or endorsement by the partners in this project.

The views expressed in this Guide are those of the authors and of the EMPIR 14IND02 project team.

Acknowledgement of funding

The production of this Guide was funded by the European Metrology Programme for Innovation and Research (EMPIR). The EMPIR initiative is co-funded by the European Union's Horizon 2020 Research and Innovation Programme and the EMPIR Participating States.

Authorship

Preparation of this Guide was led by Uwe Arz of the Physikalisch-Technische Bundesanstalt (PTB), Braunschweig (Germany) with extensive input from all members of the EMPIR 14IND02 project team. The discussion and input of all the partners in the project and their colleagues are greatly appreciated.

Suggestion for the quotation of the references

Arz, Uwe ; Probst, Thorsten ; Kuhlmann, Karsten ; Ridler, Nick ; Shang, Xiaobang ; Mubarak, Faisal ; Hoffmann, Johannes ; Wollensack, Michael ; Zeier, Markus ; Phung, Gia Ngoc ; Heinrich, Wolfgang ; Lomakin, Konstantin ; Gold, Gerald ; Helmreich, Klaus ; Lozar, Roger ; Dambrine, Gilles ; Haddadi, Kamel ; Spirito, Marco ; Clarke, Roland. Best Practice Guide for Planar S-Parameter Measurements using Vector Network Analysers : EMPIR — 14IND02 PlanarCal, 2018. Physikalisch-Technische Bundesanstalt (PTB).

DOI: `https://doi.org/10.7795/530.20190424B`

Best Practice Guide for Planar S-Parameter Measurements using Vector Network Analysers

Contents

Preface **4**

1 Introduction **6**
1.1 Probe and Calibration Substrate Selection 6
1.2 Selection of Calibration Algorithm 8
1.2.1 Selection Between Basic Calibration Algorithms 8
1.2.2 Calibration algorithm involving eigenvalue problems 8
1.3 Selection of Measurement Boundary Conditions 9
1.4 VNA Characterization 9
1.4.1 Noise Floor/Trace Noise 9
1.4.2 Linearity 10
1.4.3 Error Term Drift 10
1.5 Cable Movement 11
1.6 Connection Repeatability 11
1.7 DUT Uncertainty/Crosstalk 11

2 On-wafer measurements up to 110 GHz **13**
2.1 Results from a three-party on-wafer measurement intercomparison 13
2.1.1 Influence of probe pitch 13
2.1.2 Importance of measurement speed/instrument drift 14
2.2 Limits of established techniques for transferring uncertainties 15
2.2.1 Substrate permittivity compensation 15
2.2.2 Residual error correction 20
2.3 Transfer of uncertainties with the aid of ISS 24

3 On-wafer measurements above 110 GHz **30**
3.1 Recommended good practice for making on-wafer measurements at higher frequencies 30
3.2 Summary of high-frequency parasitic effects 31
3.3 Surface roughness effects 32
3.4 Importance of positioning accuracy 39

4 Nanodevice measurements **40**
4.1 Solving the impedance mismatch problem 40
4.2 Addressing the scale mismatch challenge 41
4.3 Interferometric methods 41
4.3.1 Passive methods 42
4.3.2 Active Methods 44

5 Uncertainties in on-wafer measurements **48**
5.1 Introduction 48
5.2 VNA Tools II on-wafer example 49
5.2.1 Introduction 49
5.2.2 New project and basic definitions 49
5.2.3 Measurements 50
5.2.4 Calibration configuration 53
5.2.5 Error correction 53
5.2.6 Data Explorer 53
5.3 Uncertainty budget examples 56
5.3.1 Expanded uncertainties 56
5.3.2 Uncertainty budgets 57

6 Conclusions and Outlook **58**

7 Acknowledgements **58**

References **59**

Preface

In the European project PlanarCal [1] a major effort has been undertaken to characterise components and devices for eventual use in high-speed and microwave applications (e.g. wireless communications, automotive radar and medical sensing) with known measurement uncertainties. It is the purpose of this Best Practice Guide to give an overview of the major outcomes of this project together with useful information on recommended measurement practice, different sources of uncertainty and the determination of uncertainties. This Best Practice Guide is not intended to replace available literature such as [2], [3], or [4] – just to name a few. All these textbooks offer comprehensive introductions to the subject of on-wafer measurements and deembedding, which are suitable for beginners as well as advanced users in industry and academia. Such information will not be replicated in this Guide. Instead, this Guide aims to present useful best practice recommendations together with key takeaways developed from the research performed in PlanarCal during the project's lifetime from 2015 until 2018.

The research in PlanarCal has been focussed on passive one- and two-port on-wafer measurements on typical microwave substrates such as GaAs, Al_2O_3 (alumina) and fused silica for frequencies up to 325 GHz, including nanodevice measurements. To this end, parasitic modes as well as effects occurring at higher frequencies such as radiation, dispersion and surface roughness have been investigated together with the impact of the probe itself and its neighborhood. The influence of the neighborhood on coplanar waveguides (CPWs) used as standards for multiline Thru-Reflect-Line (TRL) calibrations [5] was demonstrated for CPWs on GaAs and alumina substrates in [6] and [7], respectively. The latter investigation included different probe geometries and suggested measures to suppress the occurrence of substrate modes. In [8], a similar investigation was performed for thin-film microstrip lines. The impact of radiation losses due to multimode propagations on TRL calibrations in the WR10 band was described in [9]. All the investigations confirmed that the measurement result depends on the environment as well as on the specific combination of substrate material, planar waveguide type, and probes. Only for such fully specified combinations, and only when single-mode propagation is ensured, reliable uncertainties for on-wafer S-parameters can be stated.

This Best Practice Guide is organized as follows. In the Introduction we give an overview of commonly used terminology and recommendations for the choice of measurement equipment. As Vector Network Analyzers (VNAs) are an indispensable part of each on-wafer measurement setup, we also give recommendations on how to characterize the performance of such instruments and give typical numbers for one specific setup.

In Section 2 we summarize key findings for on-wafer measurements performed in the frequency range up to 110 GHz. In this frequency range, traceability was recently demonstrated for devices fabricated in membrane technology [10]. At the end of the project, the methodology of [10] could also be extended to fused silica [11], paving the way to traceability for most commonly used microwave materials. The biggest challenge remains the transfer of the (supposedly low) uncertainties obtained on a reference substrate to a different substrate incorporating the devices under test (DUTs) to be measured. Some results from techniques developed to this end will also be given in this Section. Finally, the Section concludes with a recommendation for transferring uncertainties from a reference custom calibration to industrial DUT environments making use of commercially available impedance standard substrates (ISS).

In Section 3 we address the difficulties associated with measurements above 110 GHz. This includes the consideration of surface roughness, a short summary of high-frequency parasitic effects and an excursion on the importance of probe positioning accuracy. More details on high-frequency parasitic effects can be found in a different document developed in PlanarCal, named "Guidelines for the design of calibration substrates, including the sup-

pression of parasitic modes for frequencies up to and including 325 GHz", which is also publically available from the PlanarCal website [1].

Section 4 contains useful advice for characterizing nanodevices over a wide frequency range, looking both into the difficulties of size and impedance mismatch compared to ordinary on-wafer measurements. Also, an overview of interferometric methods is given.

Section 5 finally covers the subject of uncertainties in on-wafer measurements. Without dedicated software, it is virtually impossible to take into account all the relevant sources of uncertainty. To this end, the VNATools software package [12] developed by METAS has been extended to include uncertainties in on-wafer measurements. In this Section, also an introduction to the main features and use of VNATools is given. To achieve traceability, PTB has developed an uncertainy budget for multiline TRL calibrations in Matlab based on the same measurement model and uncertainty propagation engine [13] as the one used in VNATools. Typical examples from the uncertainty budget calculations are given in Section 5, illustrating the relative importance of the different sources of uncertainty in on-wafer measurements.

1 Introduction

Design and characterization of high frequency electronics relies upon accurately defining the reference plane of the calibration process, and in general placing it as close as possible to the DUT to remove all unwanted parasitic. In order to define such reference planes and remove all the systematic errors of the measurement setup (i.e., cable and receiver conversion losses, amplitude and phase tracking errors, and other errors), a calibration procedure [14] needs to be carried out prior to the measurement.

Calibration techniques for on-wafer measurements typically consist of a probe-level calibration (first-tier) performed on a low-loss substrate (i.e., alumina or fused silica) [15, 16, 17, 5]. This probe-level calibration is then transferred to the environment where the DUT is embedded in and often, to increase the measurement accuracy, this calibration is augmented with a second-tier on-wafer calibration or de-embedding step. This allows moving the reference plane as close as possible to the DUT, by de-embedding the parasitics associated to the contact pads and the device-access vias [18]. The process of transferring the first-tier calibration to another structure assumes that the delta capacitance introduced by changing the substrate under the probes (i.e., boundary conditions) is negligible. As it was shown in [19] this capacitance is dependent on the probe topology and substrate characteristic, creating a coupling which increases with frequencies. To remove the errors arising from neglecting or improperly removing this delta capacitance, the calibration kit should be implemented in the same environment of the DUT.

1.1 Probe and Calibration Substrate Selection

Calibration substrates are provided by different vendors to perform probe-level calibration (first-tier). The substrates are realized as a slab of a single material providing low dispersion (i.e., permittivity change versus frequency) and low dielectric losses. The models of the standards provided in most of the available calibration substrates are based on simple (i.e., frequency invariant) C, L and R, as shown in Fig. 1.

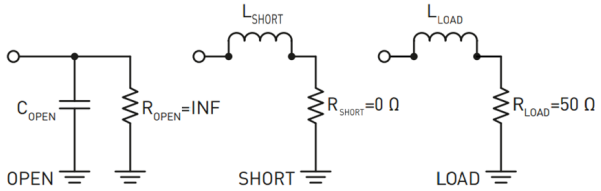

Figure 1 Equivalent circuits of the planar open, short and load standards.

When calibration techniques using full knowledge of the standards are employed (i.e., SOL based) the accuracy of the calibration can be improved by using more accurate (frequency dependent) standard models. This can be achieved using an experimental approach as shown in [20, 21, 22], or a simulation based (EM) one as shown in [23].

The choice for the optimum pitch of the probe to be employed in a given frequency range is dependent on the probe technology implementation and follows the same requirements of low dispersion used in CPW lines. For this reason, assuming that the final part of the probe transition is implemented as a CPW line design, as is the case for the Dominion probe shown in Fig. 2, the choice of the max tip to tip spacing is bounded by the $\lambda/4$ at the maximum desirable frequency of operation and the effective permittivity of the line section. When selecting micro-machined probes (i.e., using silicon as carrier) it is important to consider the high permittivity of the material (i.e., 11.9) when computing the effective permittivity of the CPW section.

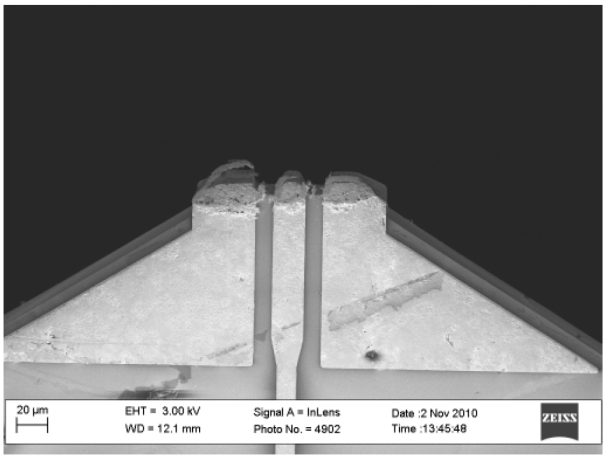

Figure 2 SEM images of the micro-machined probe tips after 3000 contacts (from [24]).

When some material properties of the probe tip are known the dispersion characteristics of a CPW versus gap width can be used as a tool to define the maximum probe pitch to be employed.

When selecting probes for a given test circuits few things should be kept in mind:

1. The skating area width and length extension are dependent on the probe make, and should be analysed and found compatible with the pad sizes available, or optimized when full custom designs are made (see Fig. 3).

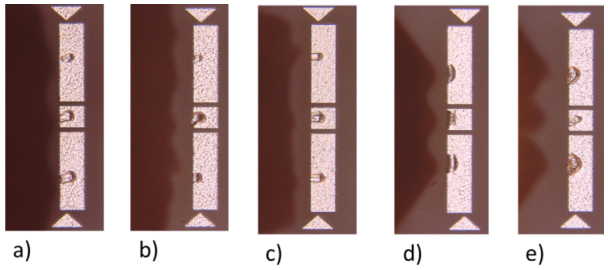

Figure 3 Landing area of probe model from company #1 for the WR10 a), WR5 b) and WR3 c) frequency band, probe model from company #2 for the WR3 d) and probe model from company #3 for the WR3 e).

2. When probing on aluminium pads special probe tip alloy should be used, i.e., nickel alloy probe tips, to reduce the contact resistance and improve the probe lifetime.

3. When using commercial technologies, the reduction of the effective pad opening due the scratch protection, as shown in the sketch given in Fig. 4, is reduced from the drawn pad dimension of 1-3um, depending on the technology.

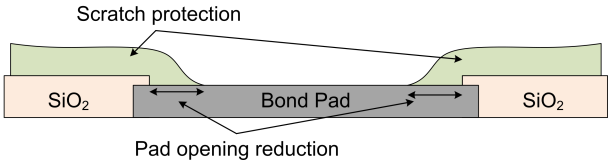

Figure 4 Cross sectional sketch view of pad opening and scratch protection.

1.2 Selection of Calibration Algorithm

Any on-wafer measurement requires the application of a calibration procedure to correct for unwanted but unavoidable perturbation of the data due to the environment, the probes, and the instrumentation itself. This calibration process is supposed to reveal the "true" performance of the DUT. In the following, basic and advanced calibration algortihms will be reviewed.

1.2.1 Selection Between Basic Calibration Algorithms

The term basic calibration algorithm refers to calibration algorithms which are simple to execute. The requirements in terms of standards are different for all considered methods and thus it is interesting to compare the field of application of each algorithm, the achievable accuracy and results. Another factor which has to be considered when choosing a calibration algorithm is the amount of real estate on the wafer required by each method.

The first calibration routine investigated in PlanarCal was the short open load thru (SOLT) routine. It requires, as the name insinuates, short, open, load and thru as standards. It can be quite easily applied for low frequencies ($\approx$15 GHz) down to DC. A crucial point is often the definition of the load standard. The SOLT technique is more robust against bad definitions of standards.

The second calibration algorithm investigated was the line reflect match (LRM) algorithm which requires a transmission line, a reflect (either open or short) and a load. In terms of frequency it has a similar range of application as the SOLT algorithm. Again a crucial point is the definition of the load standard. The LRM technique requires the least connections and standards compared to SOLT and LRRM techniques.

The third calibration algorithm was line reflect reflect match (LRRM). It requires a transmission line, a first reflect (e.g. an open), a second reflect (e.g. a short) and a load. The applicable range of frequencies is from medium frequencies ($\approx$40 GHz) down to DC. In this method an inductive component of the load is determined during calibration. This inductive component has its origin in the design of the load itself but as well in the length of the line leading to the load. This length is not easy to control because of probe skating when contacting the load. Thus for loads which are not well defined the LRRM technique can yield good results. Note that the implementation of the LRRM algorithm can differ between different software packages, e.g. VNA Tools II [25, 12] has a different implementation than WinCal [26].

The previous remarks are only applicable to situations where the definition of standards for the respective calibration comes from the manufacturer or from geometry and material properties. All three types of calibrations yield similar results in situations where the definition of standards is derived from another previous calibration.

1.2.2 Calibration algorithm involving eigenvalue problems

Calibration algorithms for VNAs which require only partially known standards pose problems for uncertainty calculation. Examples are LRM and TRL calibrations where the reflectivity of the line can not be specified because in the algorithm it is assumed that the line has a characteristic impedance of 50 Ω. In reality the line in use will not have exactly the required characteristic impedance and thus this needs to be taken into account for uncertainty computation. The algorithm presented in [27] is a generalization of calibration schemes with partly unknown standards, including [5]. The generalization consists of constructing an eigenvalue problem for each calibration scheme. One obvious advantage is that the same algorithm can be used for different schemes as TRM, LRM, TRL and LRL. Another advantage is that partly unknown lines can now be described with non-zero reflection and uncertainty, which is a clear improvement over the traditional TRL algorithm. Over-determined calibration with

several partly unknown lines is as well possible with this algorithm. This is an advantage if broad frequency ranges have to be covered. The propagation of uncertainties coming from instrument noise, instrument linearity, drift, cable stability, connection repeatability is fully supported by solving quadratic eigenvalue problems. This algorithm is analytic and thus can be used to generate starting values for an optimization calibration involving offset shorts or opens and multiple lines.

1.3 Selection of Measurement Boundary Conditions

With growing frequency the calibrated results become increasingly sensitive to parasitic effects such as radiation, multimode propagation, and substrate modes. The selection of proper measurement boundary conditions plays an important role in mitigating those unwanted effects. An inappropriate choice of chuck material can introduce parasitic substrate modes, which may lead to enhanced parasitic coupling to neighboring structures and radiation effects. For coplanar waveguides, the parasitic effects due to the propagation of the substrate mode are strongly dependent on the dielectric constants of the chuck material and the wafer. Substrate modes can propagate if the dielectric constant of the chuck material is lower than that of the substrate. These modes can degrade the accuracy of any on-wafer calibration. This was investigated with a focus on multiline TRL calibrations in [6], [7], and [8].

Substrate modes can be suppressed under the following conditions:

- If the dielectric constant of the chuck material is similar to that of the substrate. Then substrate and chuck form more or less a homogeneous medium and one has a two-layer structure, which does not support any substrate modes.
- If the dielectric constant of the chuck is larger than that of the substrate, this type of three-layer structure also does not support substrate modes.

Therefore, it is suggested to use a chuck material which has a permittivity value similar to the calibration substrate or larger than this value.

1.4 VNA Characterization

Figure 5 shows the on-wafer measurement setup used at PTB. Measurements are typically performed either on a ceramic chuck or on a metal chuck utilizing an Anritsu VectorStar VNA with mm-wave extension modules for frequencies up to 125 GHz, connected to ground-signal-ground microwave probes from various vendors with differing pitch sizes. To enable automated multiline TRL calibrations, a semi-automated wafer prober (Süss PA 200) with motorized x/y-positioner on the right-hand side is used.

To estimate the uncertainty contributions of the VNA, the measurement setup must be characterized. Procedures for this are given in [28] for coaxial lines and rectangular waveguides, and can be applied to some extent to on-wafer setups. In the following, the most relevant input quantities for the measurement process are listed with their respective values and/or uncertainties. The coverage factor is k=2 (95 % confidence level) unless indicated otherwise. Usually, the uncertainty contribution increase for higher frequency. But sometimes, due to the measurement setup itself (or internal VNA architecture), large uncertainty values arise for medium or even lower frequency ranges.

1.4.1 Noise Floor/Trace Noise

Table 1 shows the noise floor and trace noise uncertainties of the VNA used in Fig. 5. For noise contributions, $k = 1$ (68.3 % confidence level) is typically applied. This is due to historical reasons. In most data sheets of commercial measurement devices the noise

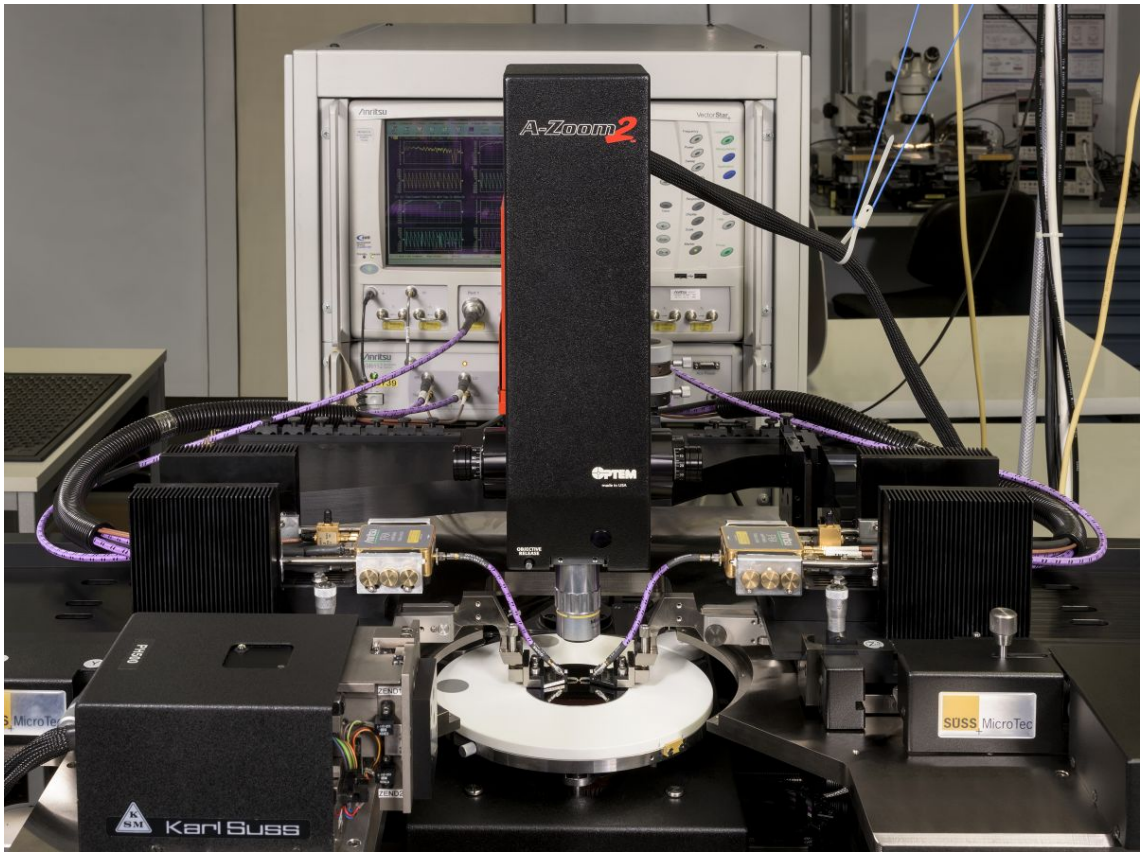

Figure 5 PTB on-wafer measurement setup.

contributions are stated for $k = 1$. The results given in Table 1 are based on repeated measurements of two VNA ports with attached shorts.

1.4.2 Linearity

For the VNA shown in Fig. 5 the uncertainty due to not perfectly linear receiver was estimated to 0.01 dB and 0.066 ° for the complete magnitude and frequency range. These values can be obtained with measurements of characterized attenuation devices (often step attenuators with very low measurement uncertainty), but good estimates are often given in the data sheet of the device manufacturer.

1.4.3 Error Term Drift

Drift of the measurement setup is often a major uncertainty contribution in VNA measurements. One can use different definitions: drift of raw values (perhaps even for different

Table 1 *Uncertainties due to noise (k=1).*

Frequency / GHz	Noise Floor / dB	Trace Noise Mag / dB rms	Trace Noise Phase (° rms)
00.000	-110	0.004	0.03
30.000	-120	0.003	0.04
30.001	-100	0.003	0.02
55.000	-100	0.002	0.01
55.001	-115	0.001	0.01
80.000	-120	0.001	0.01
80.001	-115	0.002	0.05
120.000	-100	0.004	0.03

nominal values of the connected DUT) or drift of the calibrated setup. Here, the results are given for the drift of the error terms (of the calibrated VNA), see [28]. Table 2 shows the drift results for the VNA of Fig. 5.

Table 2 *Uncertainties due to error term drift.*

Frequency	Switch	Direc-	Tracking		Symmetry		Match
	Term	tivity	Mag	Phase	Mag	Phase	
/ GHz	/ dB	/ dB	/ dB	/ °	/ dB	/ °	/ dB
0.000	-35	-35	0.07	0.6	0.025	0.4	-35
10.000	-35	-35	0.07	0.6	0.025	0.4	-35
10.001	-35	-35	0.03	1.0	0.01	0.2	-35
20.000	-35	-35	0.03	1.0	0.01	0.2	-35
20.001	-35	-35	0.06	1.4	0.03	0.2	-35
30.000	-35	-35	0.06	1.4	0.03	0.2	-35
30.001	-50	-50	0.03	0.8	0.01	0.3	-50
120.000	-50	-50	0.03	0.8	0.01	1.1	-50

1.5 Cable Movement

If cables are moved during measurements, an uncertainty contributions must be estimated for this movement. In Fig. 5, 1-mm cables are connected to the actual on-wafer probe, but they are not moved. Moved are the cables connected to the mm-wave extension modules. The movement of the cables between the VNA and the mm-wave extensions can sometimes be neglected, because the frequency is usually low ($< 20\,\mathrm{GHz}$). For the setup of Fig. 5, however, the cable effects are not negligible. They were determined by repeated measuring of coaxial shorts and matched devices following the procedures from [28]. The results are given in Table 3.

Table 3 *Uncertainties due to cable movement.*

Frequency	Reflection	Transmission	Transmission
/ GHz	stability / dB	stability Mag / dB	stability Phase / °
00.000	-50	0.05	0.1
30.000	-50	0.05	0.4
30.001	-60	0.01	0.1
120.000	-60	0.01	0.1

1.6 Connection Repeatability

The uncertainty due to limited connection repeatability has been considered with -60 dB in this study. The value was determined from repeated measurements ([28]) of several on-wafer devices and is only valid for one combination of probe and substrate. One has to be careful, not to include other uncertainty contributions (e.g. drift, cable movement), thus the measurements should be done quickly enough, but without moving any cables.

1.7 DUT Uncertainty/Crosstalk

Instead of applying the crosstalk correction of [29], the effect of crosstalk can also be modeled as uncertainty contribution with the DUT uncertainty approximation described in [30]. Here, crosstalk effects on reflections are neglected. The transmission uncertainty depends on the

frequency as well as on the reflection magnitude of the measured device, which is substrate-dependent. It was estimated from several measurements of structures on a fused silica substrate with different reflection magnitudes and is given in Table 4.

Table 4 *Transmission uncertainties due to crosstalk (in dB)*

Reflection Mag (lin. mag.)	Frequency (GHz) 0	20	50	120
0.0	-60	-55	-50	-45
0.2	-60	-55	-50	-45
0.8	-60	-40	-35	-20
1.0	-60	-40	-35	-20

2 On-wafer measurements up to 110 GHz

2.1 Results from a three-party on-wafer measurement intercomparison

In [31] we reported on initial results of a three-party on-wafer measurement intercomparison carried out on a custom-made alumina calibration substrate in the frequency range up to 110 GHz. The participants of the intercomparison were PTB, FVB, and FhG, all contributing with their individual measurement configuration. At PTB, for instance, measurements were performed VNA shown in Fig. 5 with millimetre-wave extension modules for frequencies up to 125 GHz, connected to GGB ground-signal-ground microwave probes with 100 and 150 μm pitch. The correction of the vector network analyzer measurement was performed for all participants with the highly-accurate multiline TRL calibration [5]. The focus of the investigation was on the influence of the measurement system, the probe geometry and operator skills.

2.1.1 Influence of probe pitch

The results of this first comparison showed that many factors have to be considered for the evaluation of on-wafer measurements. However, it is very difficult to isolate the factors leading to the differences observed between the different configurations. At the present state it is especially difficult to assign certain artifacts in the measurements to certain properties of the probe. Simulations indicated that main influences stem from the extension of the probe, the extension of any absorber around the probe and the extension and geometry of the needles. An important role plays also the region of the transition from the coaxial line to the needles.

As an example, Fig. 6 shows the difference between error-corrected measurements of an attenuator performed at PTB with GGB probes differing in the pitch width (100 μm versus 150 μm). The experiment was performed in a very controlled environment, using the same measurement setup, the same calibration structures, the same chuck material and, last but not least, the same operator. Nonetheless, a systematic deviation for frequencies above 50 GHz can be observed, which can almost certainly be attributed to the difference between the probe geometries. For probes from different vendors, even bigger deviations can occur.

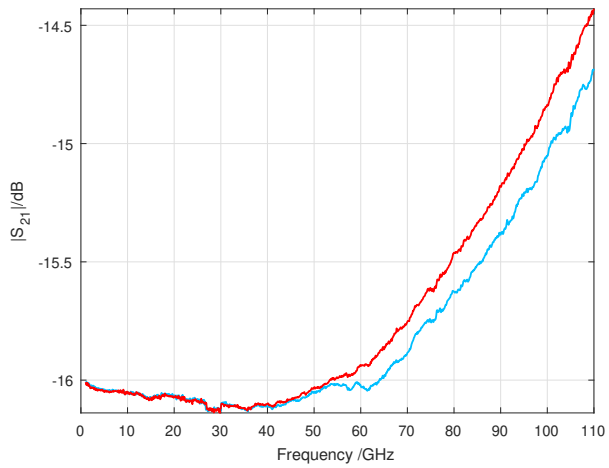

Figure 6 Influence of probe pitch width (blue - 100 μm, red - 150 μm) on transmission measurement of an attenuator.

2.1.2 Importance of measurement speed/instrument drift

As part of the intercomparison of [31] the partners agreed on the relevant measurement parameters and system settings such as IF bandwidth, frequency range, number of data points and the calibration substrate to rule out deviations. The devices to be measured were documented in a detailed measurement plan and in order to achieve an identical evaluation with a multiline TRL calibration, all partners were encouraged to acquire raw data. The calibration substrate was circulated between the partners. Each party was allowed to choose the on-wafer probes (pitch size according to the calibration substrate), chuck material and the operator individually. Within the given parameters, the measuring speed could only be varied by the on-wafer prober station (automatic / manual) and by the operator.

Within this three-party on-wafer measurement intercomparison a total of eleven datasets with different settings were evaluated. An essential result of the evaluation was that not the on-wafer prober type (semi automated / manual station) showed the biggest influence on the calibration results, but the operator with the overall measurement time. Artefacts caused by system drift and stability could be identified from the data resulting from longer measurement durations. In order to obtain reliable measurement results the operator should therefore try to measure with a continuously fast speed, this applies for the calibration standards as well as the DUTs. With a short overall measurement duration and a fast measurement process the system/instrument drift influence can be reduced significantly (see Fig. 7).

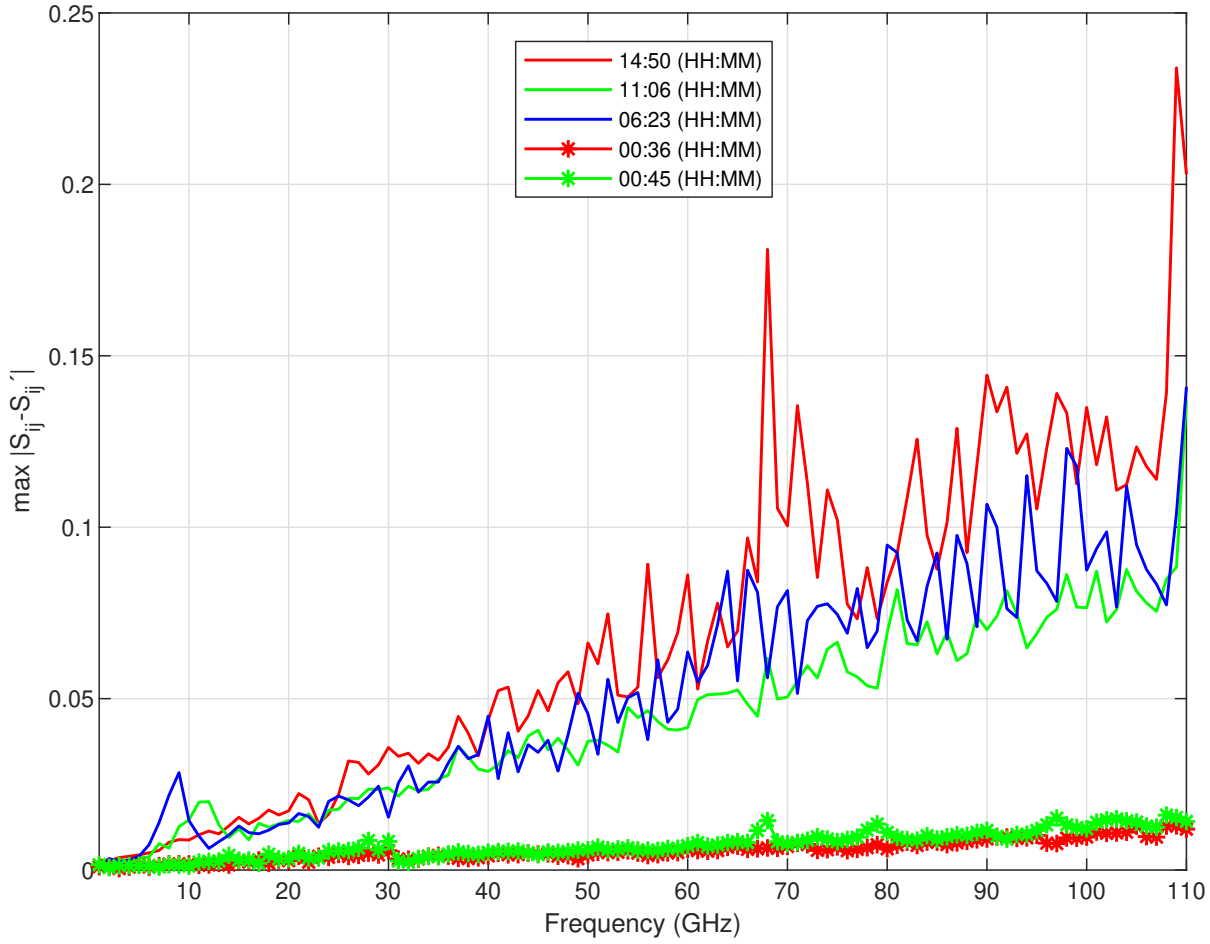

Figure 7 Drift as a function of measurement duration calculated as worst-case error bounds with the method of [32] (HH:MM is the total measurement time in hours:minutes).

2.2 Limits of established techniques for transferring uncertainties

In this section we report on methods to transfer uncertainties from reference calibration substrates to working calibration substrates. The aim is to preserve the low uncertainties in S-parameter measurements achieved on custom-made reference calibration substrates even when using low-cost working calibration substrates, such as e.g. impedance standard substrates, which can be purchased from several on-wafer vendors. Recommendations for the transfer of uncertainties will be given at the end of the section.

2.2.1 Substrate permittivity compensation

In [33], a simple capacitance model was developed to account for the effect of a change in substrate permittivity on coplanar waveguide TRL calibrations performed on different substrate materials. For all calibrations, the reference plane was moved to the probe tip and the reference impedance was set to 50 Ω. Whereas in [33] all cross-sectional dimensions of the CPWs on the different substrates were assumed identical, the investigation in [34] demonstrated that also the measurement error caused by differences in the conductor geometry can be accounted for. As the measurements in [33] and in [34] were limited to the 40 GHz frequency range, we investigated the performance of this compensation technique using custom-made fused silica and Al_2O_3 substrates up to 110 GHz.

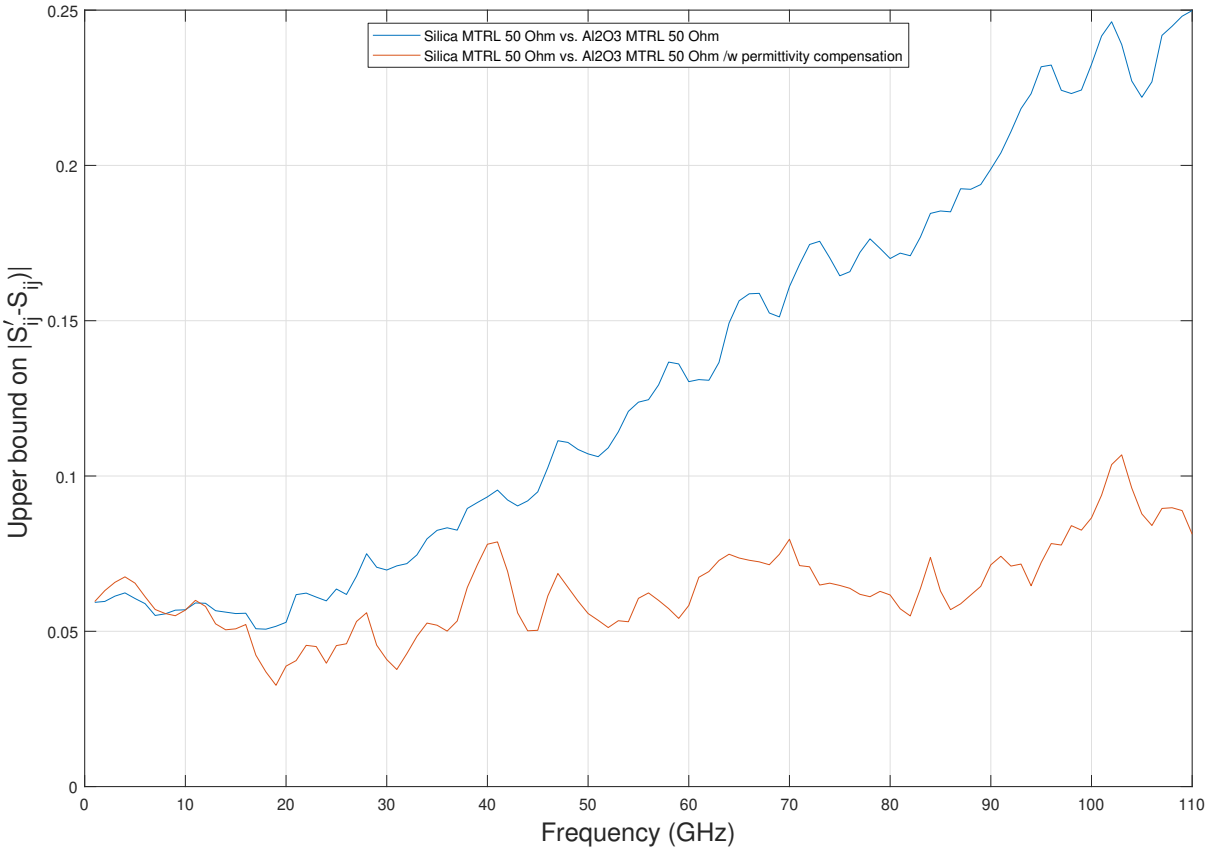

Figure 8 Worst-case error bounds calculated by calibration comparison method [32].

Figure 8 shows the worst-case error bounds calculated for multiline TRL calibrations using [32] on the two different wafers before (blue) and after (red) applying the substrate permittivity compensation technique of [33]. The red curve shows a significant reduction of the error bound after applying the permittivity compensation. As the calibration comparison technique [32] tends to overestimate the actual errors in the measurements, we decided to investigate the actual deviations from the reference measurement result before and after applying the substrate permittivity compensation.

To this end, we investigated measurements of different devices fabricated on the Al_2O_3 wafer in the frequency range from 1 to 110 GHz (see Figs. 9-13). The multiline TRL calibration on the Al_2O_3 wafer gives the most accurate result (black curves), while the multiline TRL calibration on the fused silica wafer (brown curves) will introduce a systematic error due to the differences in substrate permittivity and conductor geometries. The red curves show the result for the multiline TRL calibration on the fused silica wafer after applying the substrate permittivity compensation technique of [33]. In the following figures, the error-corrected reflection and transmission measurement are shown on the left-hand side, while the differences with regard to the reference calibration are shown on the right-hand side. In the case of one-port devices only the results for reflection are shown.

In Fig. 9, the results for an attenuator device are displayed. While the permittivity compensation only slightly improves the error in magnitude of S_{11} and S_{21}, there is a tangible improvement in the phase over the entire frequency range. For frequencies above 60 GHz, the errors in the magnitude of S_{21} cannot be compensated by the simple capacitance model of [33].

Figure 10 shows the results for a 11.4 mm long CPW line on Al_2O_3 substrate. For S_{11}, the permittivity compensation does not offer any notable improvement over the fused silica calibration. In the phase of S_{21}, there is a tangible improvement over the entire frequency range.

Figure 11 shows the results for a mismatched CPW line on Al_2O_3 substrate. Here, the permittivity compensation leads to an improvement in both S_{11} and S_{21}. As is evident from the left-hand side, the resonance frequencies of the black and red curve line up after

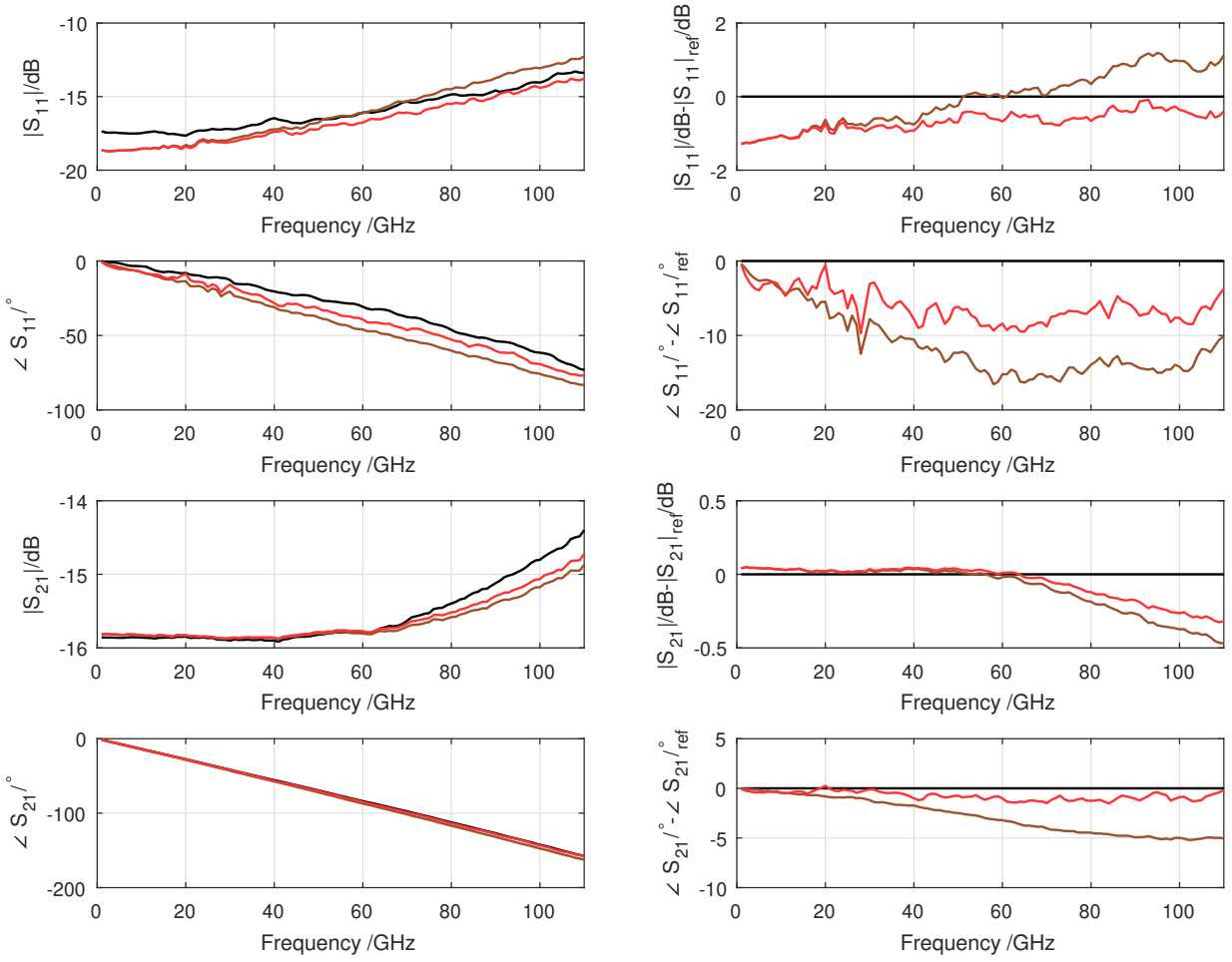

Figure 9 left: reflection and transmission measurement of attenuator device on Al_2O_3 substrate
right: measurement normalized to MTRL result on Al_2O_3
colors: MTRL on Al_2O_3 (black), on fused silica, on fused silica after perm. comp.

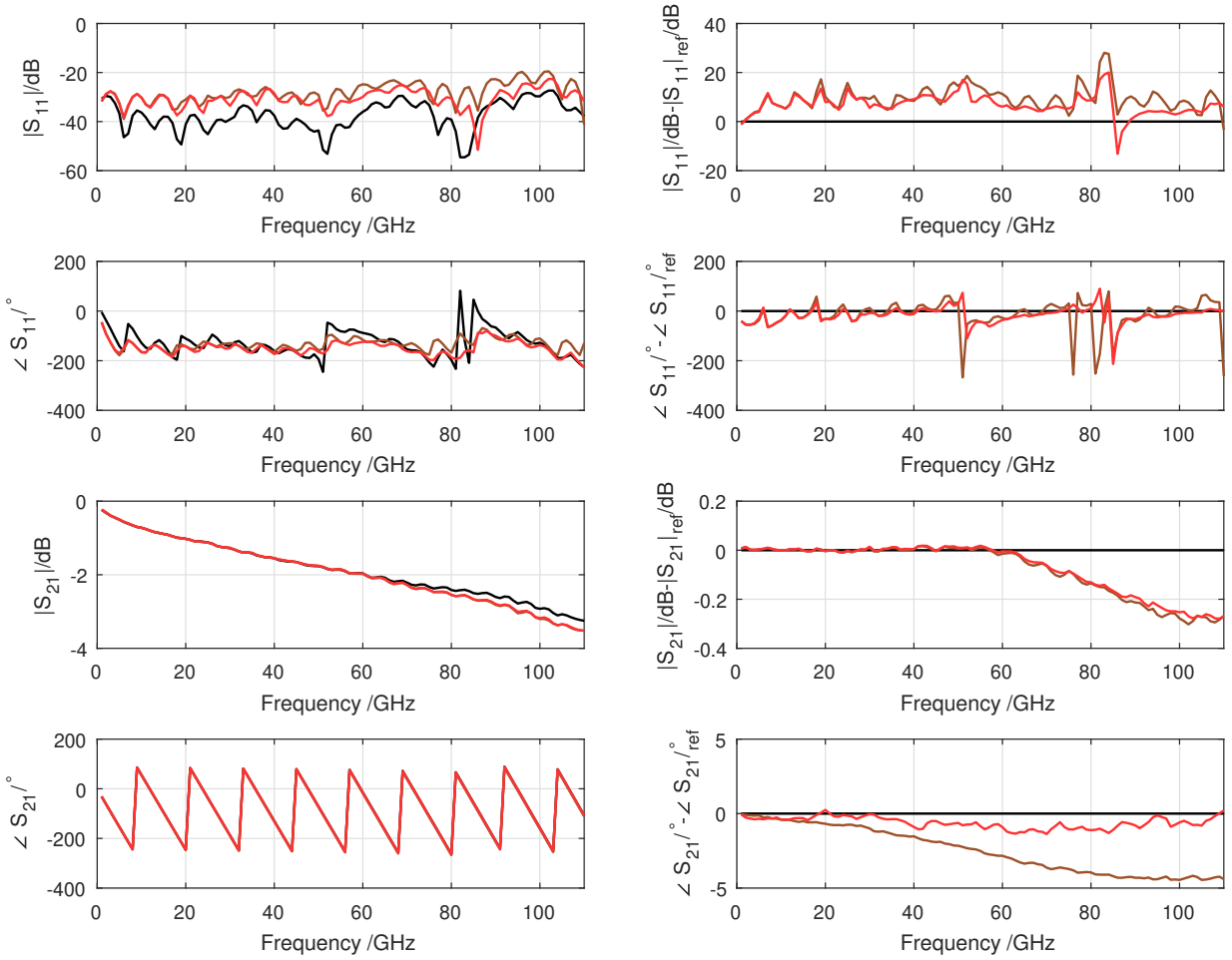

Figure 10 left: reflection and transmission measurement of 11.4 mm long CPW line on Al_2O_3
right: measurement normalized to MTRL result on Al_2O_3
colors: MTRL on Al_2O_3 (black), on fused silica, on fused silica after perm. comp.

applying the compensation. Again, the corrective effect of the permittivity compensation is more noteable in the phase, and for frequencies above 60 GHz, the errors in the magnitude of S_{21} cannot be compensated by the technique of [33].

Figure 12 shows the results for a one-port device, an offset open. The permittivity compensation only improves the phase of S_{11}. The compensation does not work for the magnitude of S_{11}, and again, for frequencies above 60 GHz, the systematic errors in the magnitude of S_{11} start to increase with frequency.

Figure 13 shows the results for a 0.4 mm long thru line on Al_2O_3 substrate. For S_{11}, the permittivity compensation hardly offers any improvement over the fused silica calibration. There is a tangible improvement in the phase of S_{21} over the entire frequency range. For frequencies above 60 GHz, the systematic errors in the magnitude of S_{21} cannot be compensated by the technique of [33].

In summary, one can state the permittivity compensation technique of [33] mostly improves on the phase error introduced by the off-wafer calibration on fused silica. The effect is generally more noteable in S_{21} compared to S_{11}. With regard to the magnitude error, which drastically increases for frequencies above 60 GHz in S_{21}, almost no improvement can be found.

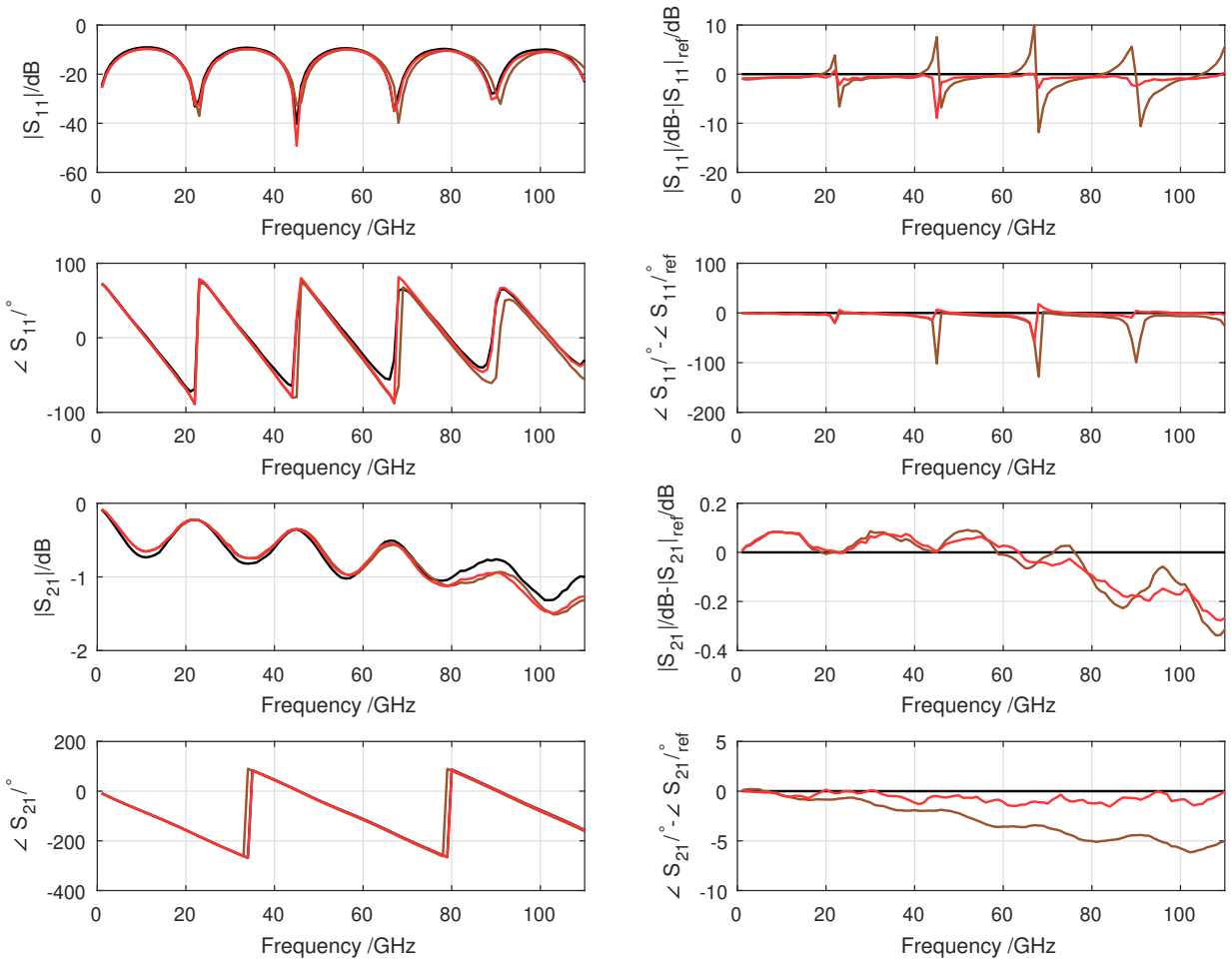

Figure 11 left: reflection and transmission measurement of mismatched line on Al_2O_3
right: measurement normalized to MTRL result on Al_2O_3
colors: MTRL on Al_2O_3 (black), on fused silica, on fused silica after perm. comp.

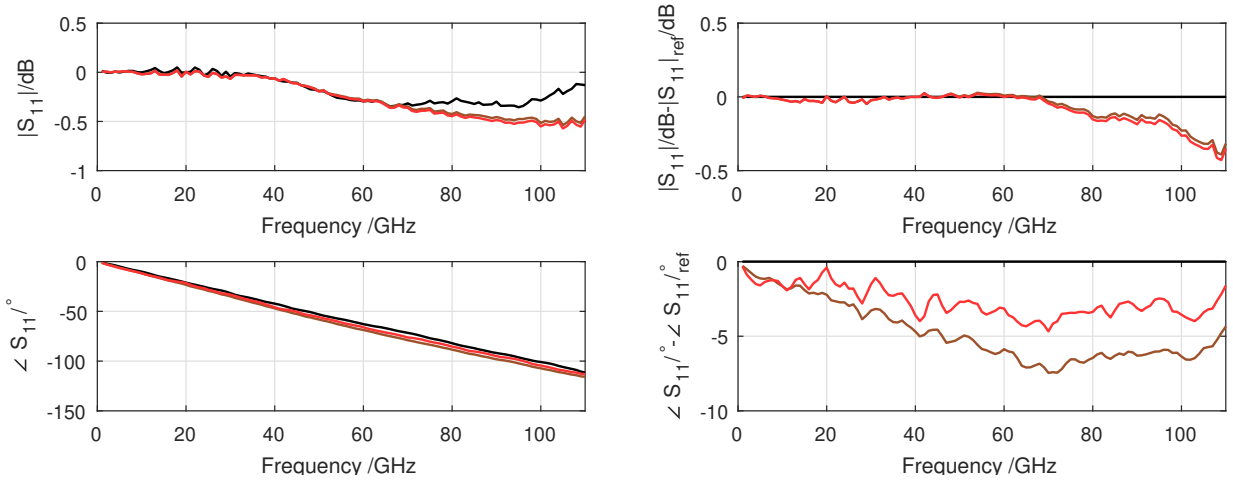

Figure 12 left: reflection and transmission measurement of open device on Al_2O_3
right: measurement normalized to MTRL result on Al_2O_3
colors: MTRL on Al_2O_3 (black), on fused silica, on fused silica after perm. comp.

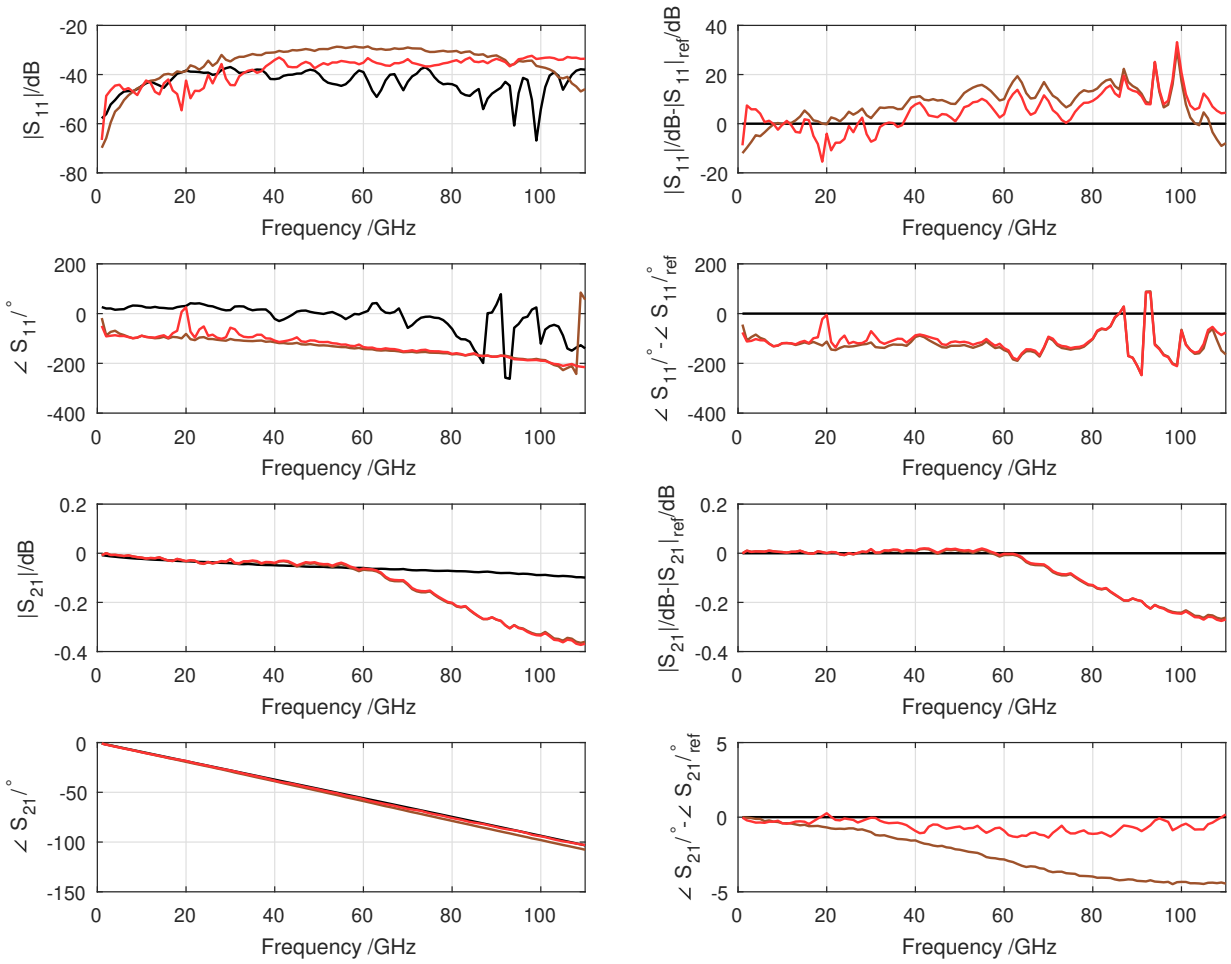

Figure 13 left: reflection and transmission measurement of thru line on Al_2O_3
right: measurement normalized to MTRL result on Al_2O_3
colors: MTRL on Al_2O_3 (black), on fused silica, on fused silica after perm. comp.

2.2.2 Residual error correction

A more general approach for compensating systematic errors introduced by the VNA calibration is the determination of residual errors and the application of a second-order error correction afterwards. In [35], a method for determining complex residual errors of two-port VNA calibrations was presented which makes use of a time-domain approach. The residual errors are extracted from a distance-frequency system model using a special estimation algorithm based on the quasi-optimal unscented Kalman filter. Since the method requires only three measurement conditions, it is particularly suited for on-wafer applications, as these conditions can be obtained from using only one verification line. In [36], the same measurement conditions are exploited, but since the residual error terms are now estimated by applying a least-mean-squares method the calculation time is significantly reduced.

Here, we determined the residual errors of calibrated two-port on-wafer measurements up to 110 GHz with the method of [36], utilizing the commercial calibration substrate GGB CS5 and GGB100 microwave probes. As verification line, line 10 with a length of 6600 μm was used. As DUTs lines of different lengths were used. By analyzing the error-corrected measurements of the DUTs, we compared the accuracy of SOLT calibrations with characterized standards to SOLT calibrations with manufacturer definitions and to second-order-corrected SOLT calibrations with manufacturer definitions. In the following figures, the error-corrected reflection and transmission measurement are shown on the left-hand side, while the differences with regard to the reference calibration (SOLT with characterized standards) are shown on the right-hand side.

Figures 14-16 show the results for lines with lengths in the range $550 \ldots 1500$ μm. One obvious disadvantage of the second-order error correction becomes apparent for frequencies below 10 GHz: additional errors are introduced leading to unphysical behavior in both reflection and transmission. For higher frequencies, however, the second-order correction is mostly working as expected. In the measured reflections, the second-order error correction is beneficial in both magnitude and phase, as can be seen from the red S_{11} curves approaching the black S_{11} curves in a range of approximately $20 \ldots 110$ GHz. In the measured transmission, there is almost no improvement for the magnitude of S_{21}, while the phase of S_{21} even deteriorates slightly by means of the second-order error correction.

In summary one can state that the second-order error correction of [36] shows some promise but is currently limited by the accuracy with which the residual errors can be determined. At the edges of the frequency range (ca. 5% of the frequency band), the error of the filtering algorithm increases. This applies to measurements of both transmission and reflection coefficients. In principle, the effect can be reduced by applying a verification line with a longer length.

The current study was limited by the number of DUTs and the verification line available on the commercial calibration substrate. Future investigations should try to extend the study to better understand and overcome the current limitations of the method of [36].

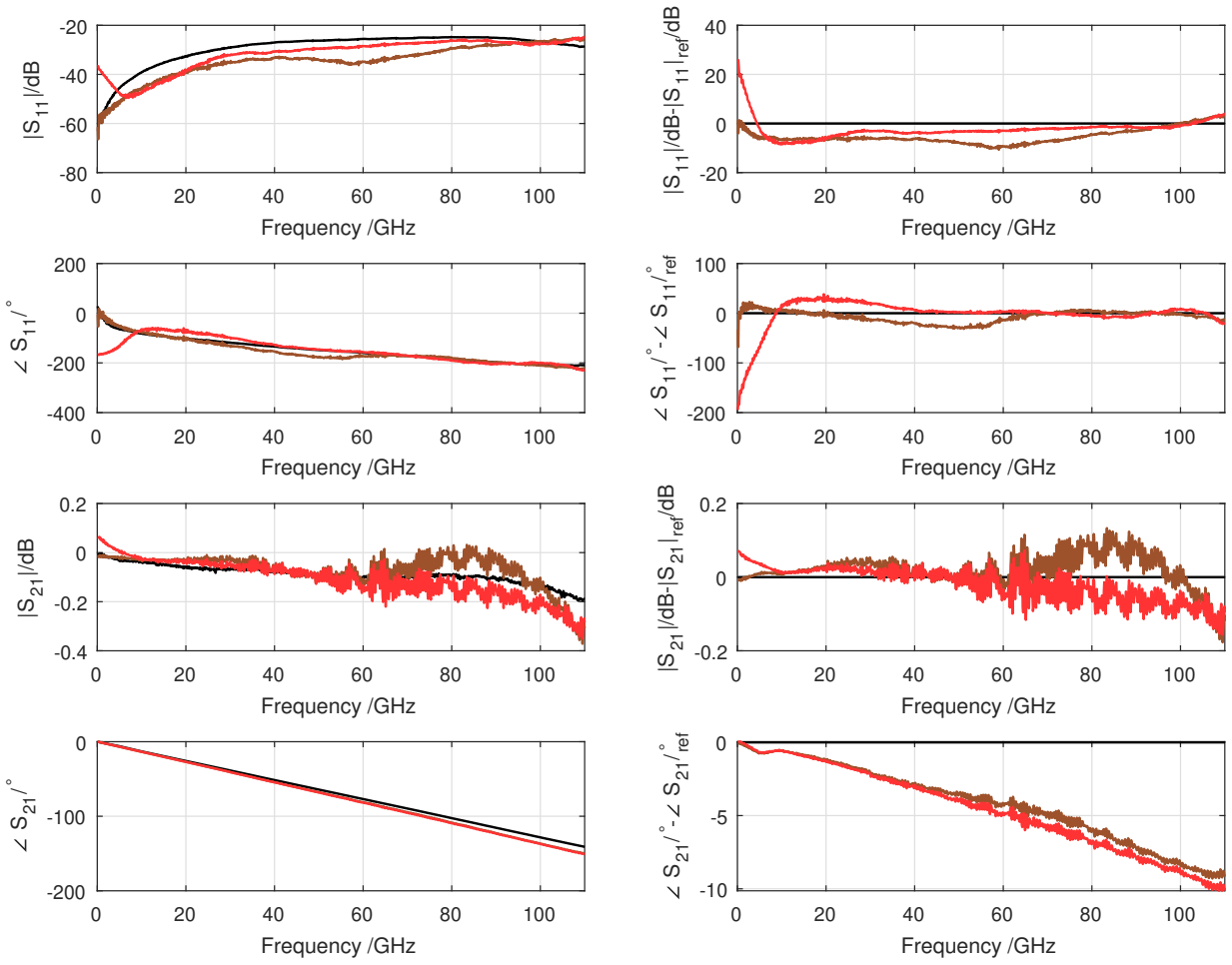

Figure 14 left: SOLT-corrected reflection and transmission of 550 μm long line on GGB CS5 right: measurement normalized to SOLT with characterized standards colors: characterized standards (black), manufacturer definitions, manufacturer definitions after residual error correction

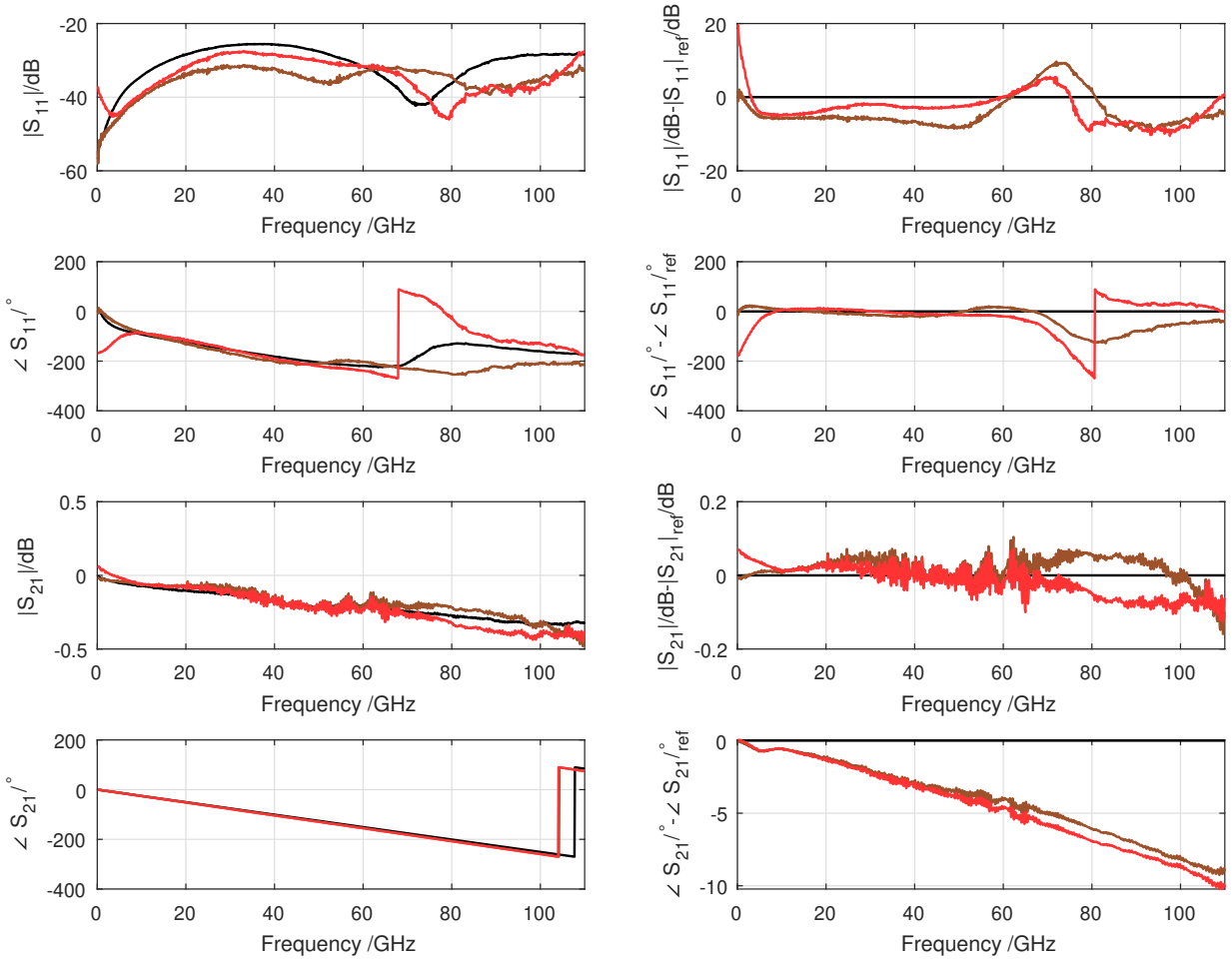

Figure 15 left: SOLT-corrected reflection and transmission of 1000 μm long line on GGB CS5
right: measurement normalized to SOLT with characterized standards
colors: characterized standards (black), manufacturer definitions, manufacturer definitions after residual error correction

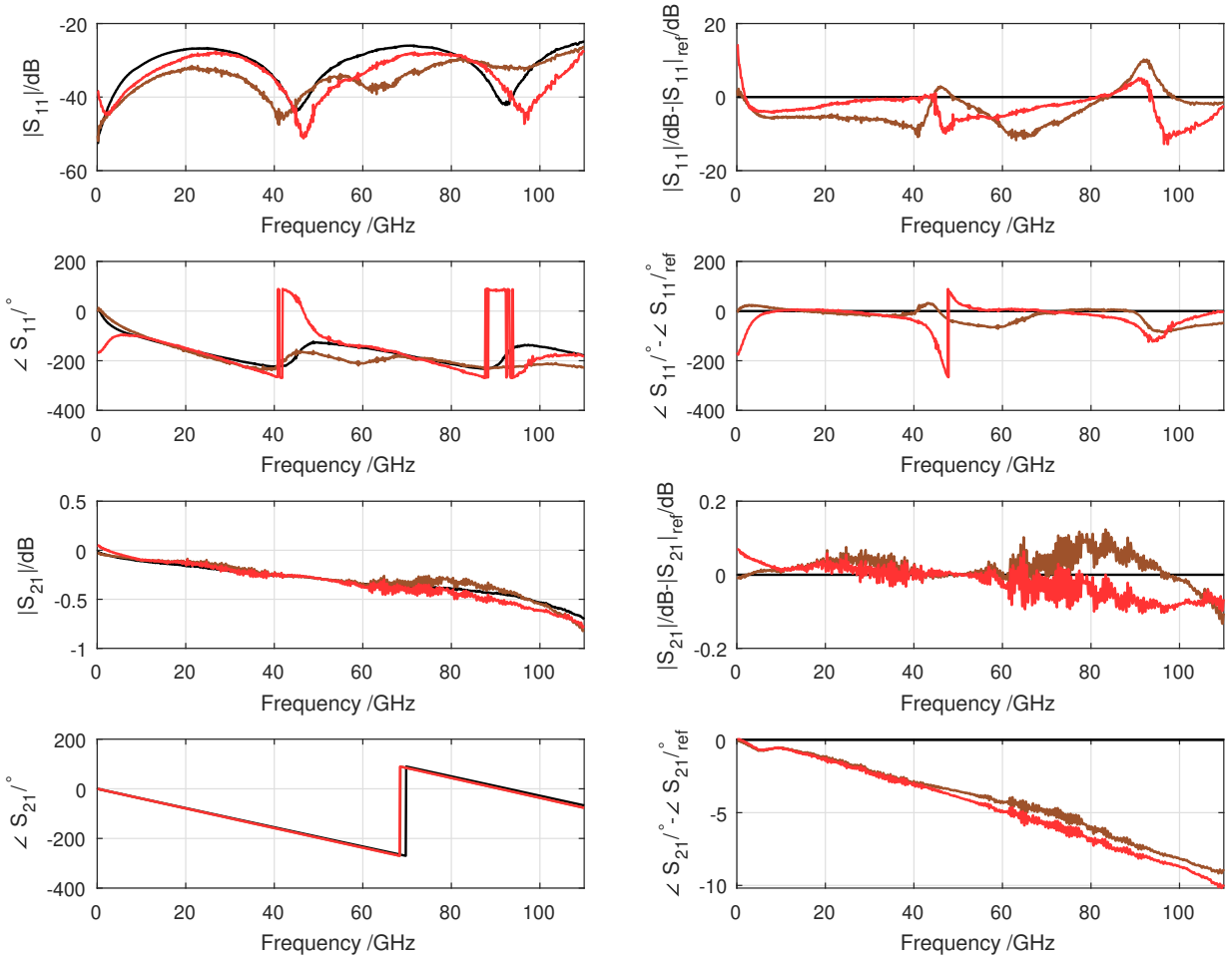

Figure 16 left: SOLT-corrected reflection and transmission of 1500 μm long line on GGB CS5
right: measurement normalized to SOLT with characterized standards
colors: characterized standards (black), manufacturer definitions, manufacturer definitions after residual error correction

2.3 Transfer of uncertainties with the aid of ISS

In [22] it was demonstrated that properly characterized standards can be used to account for differences between the commercial ISS and the target DUT measurement situation. The results of a reference MTRL calibration using custom standards were in essence duplicated with the aid of characterized ISS standards and a much simpler calibration, in this case SOLT. This constitutes a big improvement over any of the approaches discussed in the two previous subsections, where a systematic error with regard to the reference result remained.

Therefore, in order to transfer uncertainties to industrial applications where commercial ISS substrates and simple calibration algorithms have to be used, one has to first characterize the standards in a manner which is adequate for the target application. This requires building custom calibration standards on the target DUT wafer, which serve for characterizing the ISS calibration standards appropriately. In the following, we demonstrate this approach with the custom-made Al_2O_3 wafer as the target DUT wafer and the GGB CS5 calibration substrate as commercially available ISS substrate.

Recently, PTB developed a traceability path for on-wafer S-parameter measurements based on the MTRL calibration algorithm [10]. The methodology of [10] for establishing a comprehensive uncertainty budget can also be applied to other substrates, as long as the wideband material properties are known and single-mode propagation can be assumed. For the custom-made Al_2O_3 wafer used in our studies, the latter condition is strictly fulfilled only for frequencies below ca. 70 GHz. For higher frequencies, the effects of dispersion and interaction with higher-order and other parasitic modes are currently not fully captured in the uncertainty budget. Nonetheless we used this preliminary uncertainty budget and treated the Al_2O_3 wafer as reference calibration wafer for characterizing the standards on the GGB CS5 substrate.

Figures 17 and 18 show the result of characterizing the Open/Short/Load/Thru standards by means of a reference multiline TRL calibration on the custom-made Al_2O_3 wafer. The figures also show the expanded uncertainty intervals comprising the influences of MTRL calibration standard uncertainties, uncertainties from the instrumentation used, cabling influences and repeatability effects. It may appear surprising that some of the characterized standards show gain even though they are passive devices. This can easily be explained by the fact that the distance between the probe tips on the CS5 standards was smaller than the distance between the calibration reference planes on the Al_2O_3 wafer. Nonetheless the characterized CS5 standards can be used as transfer standards for accurately measuring DUTs on the Al_2O_3 wafer.

Fig. 19 compares the measurement results for an attenuator DUT and a mismatched line DUT fabricated on the Al_2O_3 wafer. The black curves show the reflection and transmission when using the reference MTRL calibration on the Al_2O_3 substrate, the red curves show the corresponding results for the SOLT calibration with the characterized CS5 standards. The shaded areas indicate the expanded uncertainty intervals. It can be clearly seen that the nominal values coincide for both calibrations, proving the consistency of the approach. The only differences appear in the expanded uncertainties, which are usually slightly increased for the calibration with the characterized standards.

Exemplary uncertainty budget values for the DUTs corrected via the SOLT calibration with characterized CS5 standards are given in the Tables 5-8. These tables show the uncertainty budget composition for the magnitude of S_{11} and the phase of S_{21} of the DUTs at a frequency of 65 GHz. The calibration standard uncertainties are designated with PTB_ML in the beginning, pointing to the fact that the characterization was performed with the PTB multiline calibration. The tables clearly show that the budgets are mostly dominated by the calibration standard uncertainties. For the phase of S_{21}, also cable effects and DUT uncertainty provide significant contributions to the total uncertainty at 65 GHz.

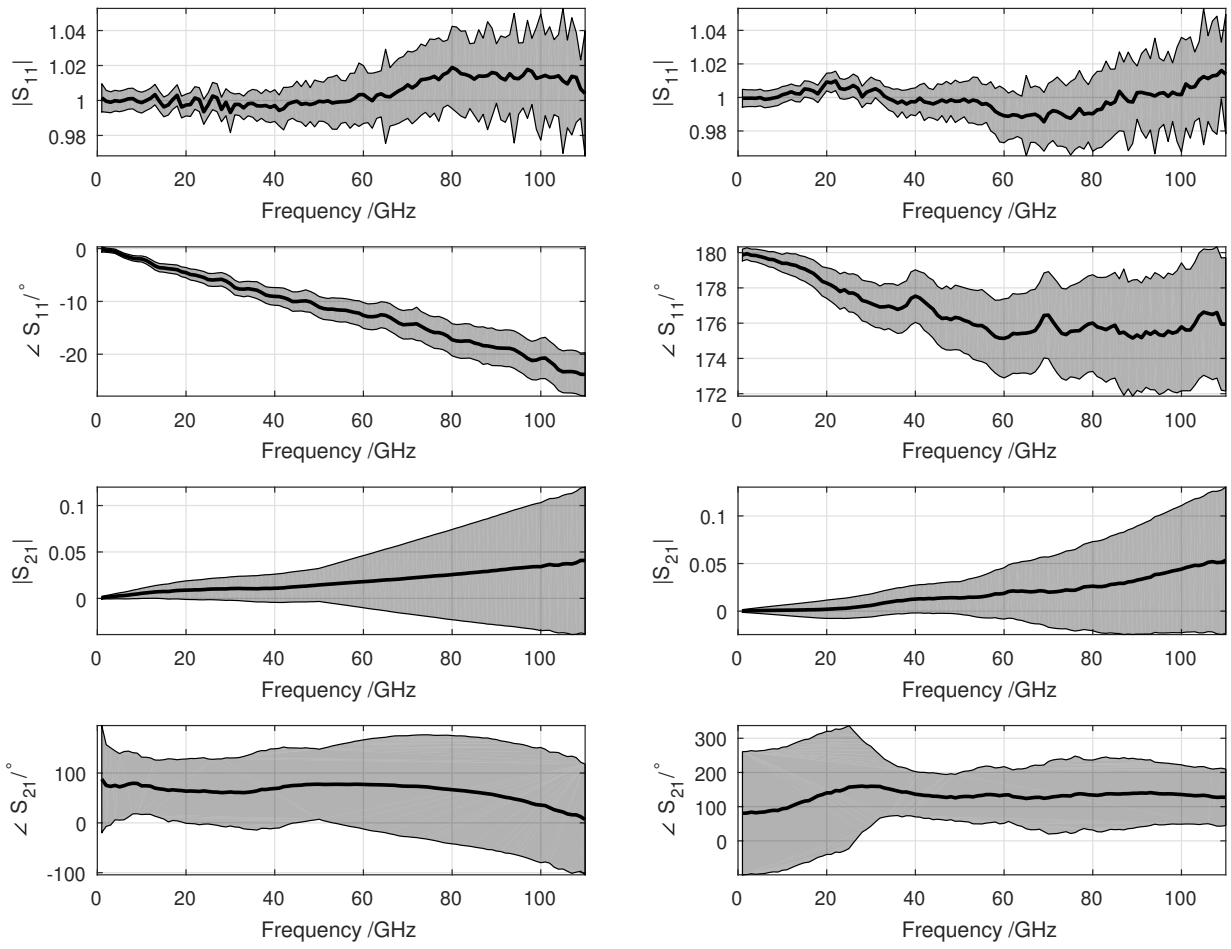

Figure 17 left: characterized Open standard on GGB CS5 substrate;
right: characterized Short standard on GGB CS5 substrate.

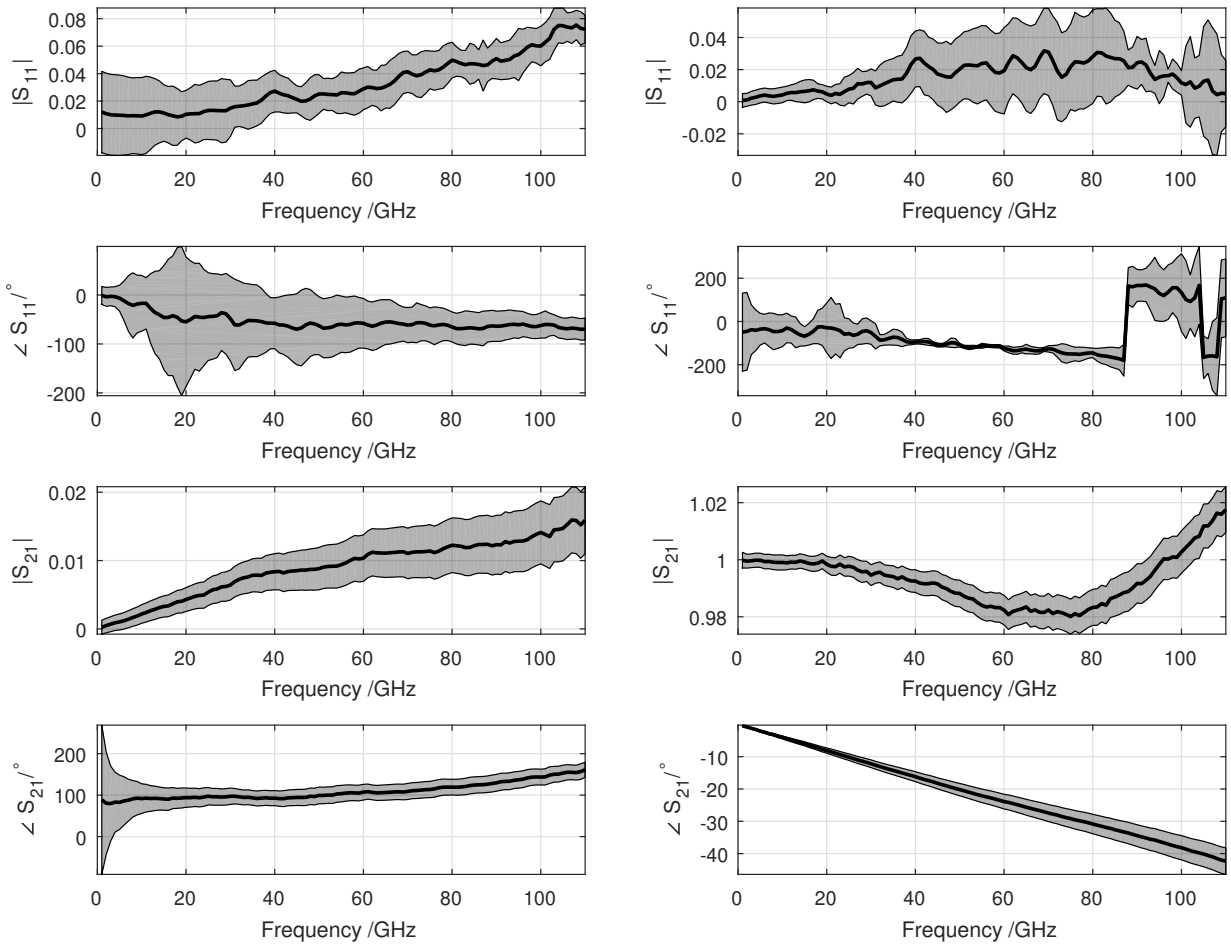

Figure 18 left: characterized Load standard on GGB CS5 substrate;
right: characterized Thru standard on GGB CS5 substrate.

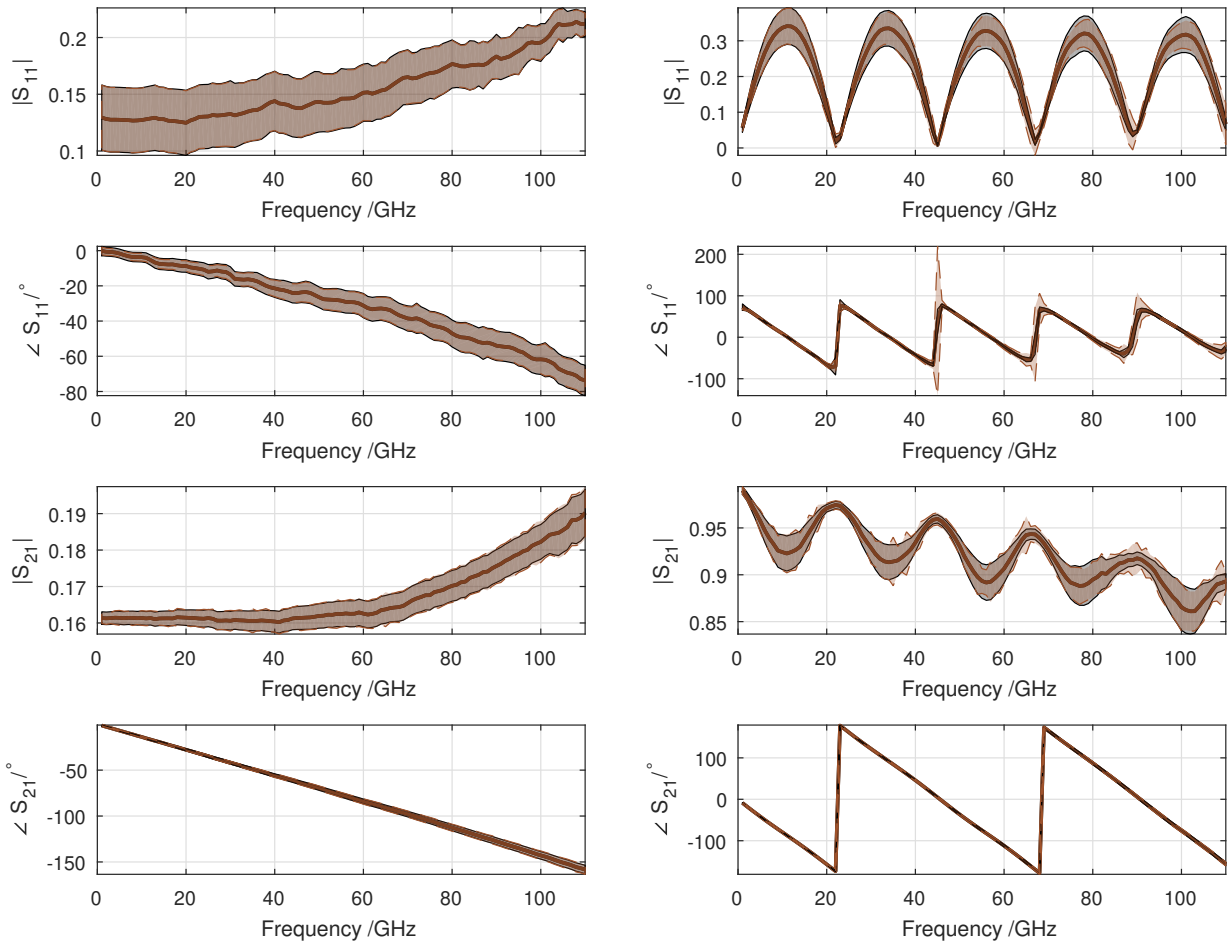

Figure 19 left: reflection and transmission measurement of attenuator on Al_2O_3
right: reflection and transmission measurement of mismatched line on Al_2O_3
colors: reference MTRL on Al_2O_3 (black), SOLT with characterized CS5 standards

Table 5 *Uncertainty budget for magnitude of S_{11} of attenuator at 65 GHz (in dB) .*

Description	Unc Component	Unc Percentage
Cable Stability	0.001450124	0.000
Calibration Standards:	0.670126203	99.592
⇒ PTB_ML_CS5_open_51 S11	0.058003624	0.746
⇒ PTB_ML_CS5_open_51 S22	0.001496587	0.000
⇒ PTB_ML_CS5_res_71_50 S11	0.666248662	98.443
⇒ PTB_ML_CS5_res_71_50 S22	0.002807877	0.002
⇒ PTB_ML_CS5_short_61 S11	0.038046580	0.321
⇒ PTB_ML_CS5_short_61 S22	0.001042205	0.000
⇒ PTB_ML_CS5_thr_81 S11	0.018936710	0.080
⇒ PTB_ML_CS5_thr_81 S12	0.000143966	0.000
⇒ PTB_ML_CS5_thr_81 S21	0.000143964	0.000
⇒ PTB_ML_CS5_thr_81 S22	0.000184802	0.000
Connector Repeatability	0.039950930	0.354
DUT Uncertainty	0.000055924	0.000
VNA Drift (Ideal VNA correlated)	0.015253581	0.052
VNA Linearity	0.000000000	0.000
VNA Noise	0.002606109	0.002
Value: -16.245	Std Unc: 0.671	U95: 1.342

Table 6 *Uncertainty budget for phase of S_{21} of attenuator at 65 GHz (in °) .*

Description	Unc Component	Unc Percentage
Cable Stability	0.713390544	19.585
Calibration Standards:	1.289100271	63.949
⇒ PTB_ML_CS5_open_51 S11	0.232294374	2.077
⇒ PTB_ML_CS5_open_51 S22	0.020862472	0.017
⇒ PTB_ML_CS5_res_71_50 S11	0.140175758	0.756
⇒ PTB_ML_CS5_res_71_50 S22	0.083127246	0.266
⇒ PTB_ML_CS5_short_61 S11	0.168673048	1.095
⇒ PTB_ML_CS5_short_61 S22	0.014458089	0.008
⇒ PTB_ML_CS5_thr_81 S11	0.114784009	0.507
⇒ PTB_ML_CS5_thr_81 S12	0.025697228	0.025
⇒ PTB_ML_CS5_thr_81 S21	1.232926518	58.497
⇒ PTB_ML_CS5_thr_81 S22	0.134985406	0.701
Connector Repeatability	0.022867158	0.020
DUT Uncertainty	0.642461555	15.884
VNA Drift (Ideal VNA correlated)	0.119556724	0.550
VNA Linearity	0.000000000	0.000
VNA Noise	0.018006836	0.012
Value: -90.9098	Std Unc: 1.612	U95: 3.224

Table 7 *Uncertainty budget for magnitude of S_{11} of mismatched line at 65 GHz (in dB) .*

Description	Unc Component	Unc Percentage
Cable Stability	0.058828227	0.083
Calibration Standards:	2.039187357	99.639
⇒ PTB_ML_CS5_open_51 S11	0.023740527	0.014
⇒ PTB_ML_CS5_open_51 S22	0.070263207	0.118
⇒ PTB_ML_CS5_res_71_50 S11	1.883437737	85.000
⇒ PTB_ML_CS5_res_71_50 S22	0.125927050	0.380
⇒ PTB_ML_CS5_short_61 S11	0.049882933	0.060
⇒ PTB_ML_CS5_short_61 S22	0.058699120	0.083
⇒ PTB_ML_CS5_thr_81 S11	0.763456399	13.966
⇒ PTB_ML_CS5_thr_81 S12	0.006792718	0.001
⇒ PTB_ML_CS5_thr_81 S21	0.006792700	0.001
⇒ PTB_ML_CS5_thr_81 S22	0.026407654	0.017
Connector Repeatability	0.106121881	0.270
DUT Uncertainty	0.001340632	0.000
VNA Drift (Ideal VNA correlated)	0.014373846	0.005
VNA Linearity	0.000000000	0.000
VNA Noise	0.011795602	0.003
Value: -19.804	Std Unc: 2.043	U95: 4.086

Table 8 *Uncertainty budget for phase of S_{21} of mismatched line at 65 GHz (in °) .*

Description	Unc Component	Unc Percentage
Cable Stability	0.724837607	21.922
Calibration Standards:	1.357885718	76.936
⇒ PTB_ML_CS5_open_51 S11	0.192502364	1.546
⇒ PTB_ML_CS5_open_51 S22	0.008051523	0.003
⇒ PTB_ML_CS5_res_71_50 S11	0.360163455	5.413
⇒ PTB_ML_CS5_res_71_50 S22	0.296612500	3.671
⇒ PTB_ML_CS5_short_61 S11	0.149293085	0.930
⇒ PTB_ML_CS5_short_61 S22	0.015031594	0.009
⇒ PTB_ML_CS5_thr_81 S11	0.075873173	0.240
⇒ PTB_ML_CS5_thr_81 S12	0.011439288	0.005
⇒ PTB_ML_CS5_thr_81 S21	1.247369834	64.922
⇒ PTB_ML_CS5_thr_81 S22	0.068567305	0.196
Connector Repeatability	0.028056880	0.033
DUT Uncertainty	0.151966164	0.964
VNA Drift (Ideal VNA correlated)	0.056212422	0.132
VNA Linearity	0.000000000	0.000
VNA Noise	0.018249220	0.014
Value: -512.689	Std Unc: 1.548	U95: 3.096

3 On-wafer measurements above 110 GHz

3.1 Recommended good practice for making on-wafer measurements at higher frequencies

The subject of recommended good practice for making on-wafer measurements above 110 GHz is still relatively new. One reason for this is that the hardware for making such measurements has been either scarce or not available at all. However, this situation has been changing in recent years, particularly with VNA extender heads becoming available at these frequencies. In fact, these extender heads are now commercially available at all frequencies to at least 1 THz.

The rollout of these VNA extender heads has been closely followed by the availability of on-wafer probes and calibration standards (on-wafer impedance standard substrates). The current state of the art is S-parameter measurements at all frequencies to 1.1 THz. However, there is very little published information available of the use of this on-wafer hardware at these frequencies – particularly, with regard to determining the quality and reliability of on-wafer measurements obtained at these frequencies.

The recently completed European research project, PlanarCal [1], has been a very valuable resource in this respect. This project included a substantial amount of work looking at making on-wafer measurements above 110 GHz. In this work, it was first noted that metrological traceability, as defined in [37], for on-wafer measurements above 110 GHz is not currently available anywhere in the world. Traditionally, it is the role of National Measurements Institutes (NMIs) such as PTB (Germany), NPL (UK), etc, to make available facilities that provide metrological traceability to end-users in industry and elsewhere. However, to establish such capabilities usually requires a large sustained effort – such an effort has yet to be made, by the NMI community, with regard to on-wafer measurements above 110 GHz.

When traceability does exist, it is relatively straightforward for end-users to determine the quality and reliability of measurements, simply by comparing their measurements with traceable references coming from the NMI community. These NMI measurements are ultimately linked back to the base units of the International System of units (SI). However, when traceability does not exist (as is the case for on-wafer measurements above 110 GHz), it is often useful for measurement laboratories to undertake repeatability and reproducibility studies in order to determine the main sources of variability (and hence the quality, reliability, etc) in such measurements [38].

Some preliminary studies of repeatability and reproducibility have been conducted during the PlanarCal project [39, 40]. These studies involved the participating laboratories in making measurements using their usual measurement setups – i.e. VNA/extender heads, probe stations, on-wafer probes, calibration techniques, calibration substrates and calibration standards. The different choices of these aspects of the measurement process help to expose the effect these aspects have on the measurement results that are obtained during the study.

Different probe designs will interact with the calibration substrate to produce parasitic elements that may not be the same as those on the DUT wafer, leading to systematic errors [41]. At higher millimetre-wave frequencies, the ground-signal-ground (GSG) probe pitch can become an appreciable fraction of the signal wavelength [42]. The use of GSG pitches of 75 μm or less is recommended.

Other major issues with measurements at high millimetre-wave frequencies and above concern isolation/crosstalk, the presence of parasitic modes (e.g. higher-order modes and substrate modes) and the effects due to neighbouring structures (i.e. other components) found close to the calibration standards on the calibration wafer. These issues were also investigated during the PlanarCal project. Some of the outcomes from these investigations have been reported in [43].

Coplanar waveguide structures, such as those typically fabricated on DUT wafers, will

exhibit higher-order modes above 50 GHz, depending on the boundary conditions above and below the substrate. It is good practice to use an absorbing material (with similar dielectric constant as the substrate) between the metallic wafer chuck and the DUT, which will suppress unwanted modes. The DUT is effectively a different structure (electromagnetically) with and without this absorber, and measurement results can differ widely depending on whether or not it is used.

Sometimes the presence of systematic errors in the measurements can be detected especially when non-physical behaviour is observed – e.g. when the observed linear magnitude of the reflection coefficient is greater than unity. This is indicative of an inappropriate reference standard used during calibration. Additionally, the presence of significant ripple on some measurement traces suggest perhaps the use of an inferior calibration technique. Generally, the choice of reference calibration substrate can have a major impact on the achieved measurements. This is because the different calibration substrates provide different calibration reference values (e.g. due to the use of different substrate materials for the calibration substrate). This means that even the same uncorrected measurement data for a given device under test (DUT) will give rise to different corrected S-parameter values due to different reference values being used during the calibration process. This occurs when a VNA is calibrated using standards found on one wafer (e.g. a commercial impedance standard substrate), and then measurements are made subsequently of DUTs on another wafer (e.g. the wafer containing the devices that need testing). For this reason, when making on-wafer S-parameter measurements that are not SI traceable, it is very important to state what references were used during calibration. In fact, as a general rule, it is good practise to state everything about the measurement setup that might have an impact on the obtained measurement results – e.g. VNA, probes (including probe pitch) and associated calibration hardware and software (i.e. the calibration substrate, the calibration method and the calibration standards used).

Whenever possible, it is preferable to fabricate some appropriate reference standards on the same wafer as the DUT. As a minimum, some lengths of CPW line and some high-reflecting standards (usually short-circuits) are needed. These enable the use of one of the calibration techniques derived from the TRL approach [44, 5] which make use of the CPW lines to acquire a reference value which is determined by the properties of the DUT substrate material. These techniques are generally superior to the more conventional Short-Open-Load-Thru (SOLT) technique, and are less dependent on accurate and repeatable probe-placement. For manual probe stations, this can be a significant source of error at higher frequencies if the calibration method requires known values for the phase of the calibration standards.

3.2 Summary of high-frequency parasitic effects

When operating in the mm-wave frequency range (i.e., in the context of this section above 110 GHz), the calibration errors arising from the inaccuracy of standard models and multimode propagation start to severely impact the calibration accuracy that can be achieved. For this reason a guideline to inform the reader on these potential problems and the means to minimize them was compiled in the EMPIR PlanarCal project, namely, “Guidelines for the design of calibration substrates, including the suppression of parasitic modes for frequencies up to and including 325 GHz ”. The interested reader is invited to familiarize himself with these effects using the above mentioned document. In the following a selection of the suggestions provided in the document is given:

Choice of substrate thickness (Guideline #1)

Compute the critical frequency (f_c) of parasitic modes (e.g. higher order modes and substrate modes) [45] of the calibration substrate employed in the given configuration (i.e., metallic

or dielectric chuck) and select those in which f_c is outside the calibration frequency or only occurs in the upper calibration range, to avoid excessive coupling of power to unwanted modes.

Impact of ground-to-ground spacing in CPWs (Guideline #4)

The influences of CPW ground width and of ground-to-ground spacing, are contributing to parasitic effects in the calibrated results, in this case a dip in S-parameters at a certain frequency. Total CPW width determines the frequency where this dip occurs, and ground-to-ground spacing influences the strength of the dip behavior. Thus, the best way to mitigate the impact of this dip is to keep the total CPW width smaller than the formula given in [45], which requires a tradeoff between the CPW total width, the used material and the upper frequency limit f_{max}.

Chuck topology (Guideline #5)

Using for the chuck a material which has a permittivity value similar to the calibration substrate reduces the effects which contribute to the degradation of the accuracy of CPW mTRL calibrations. Further investigations have shown that this is true also for a chuck material with a permittivity larger than that of the wafer, because such a layered structure does not support surface waves either.

Influence of in-line and side-way neighbouring structures (Guideline #6)

One should keep sensitive regions of the probe shadow free of structures to avoid probe coupling to neighboring structures, as shown in the figure below (investigations performed up to 70 GHz).

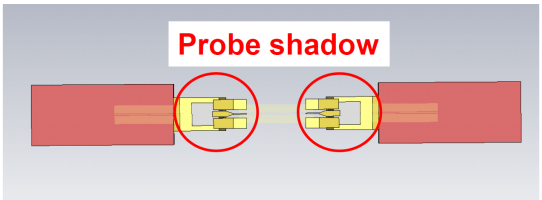

Custom designed TRL kit (Guideline #8)

When designing custom kits for LRM/TRL calibration the reflect should be realized as an offset one, keeping the minimum distance between the effective reflect and the center of the thru line (intrinsic calibration plane) to avoid requiring sign changes in the solution of the calibration equations.

3.3 Surface roughness effects

Surface roughness is one among different parasitic effects that affect signal integrity of propagating signals on transmission lines. While radiation mainly increases the attenuation α, dispersion effects have a direct influence on the phase velocity v_{ph} and only indirectly affect attenuation by increasing the line capacitance and thus, dielectric loss. In contrast thereto, surface roughness has shown to directly impacting on both, attenuation and phase velocity. The impact magnitude depends on the actual roughness on the one hand and the operation frequency on the other. Although it is a an inevitable property of real surfaces and can be appropriately taken into account by modeling and simulation, for many practical applications an impact of only little surface roughness causing deviations between rough and

smooth responses within $< 5\,\%$ in attenuation α and $< 0.5\,\%$ in phase coefficient β may be considered as negligible.

Table 9 *Frequency Bands and Waveguide Definitions.*

Band	Waveguide	Frequency Limits
W	WR10	$75 - 110\,\mathrm{GHz}$
F	WR08	$90 - 140\,\mathrm{GHz}$
D	WR06	$110 - 170\,\mathrm{GHz}$
G	WR05	$140 - 220\,\mathrm{GHz}$
Y	WR04	$170 - 260\,\mathrm{GHz}$
Y	WR03	$220 - 325\,\mathrm{GHz}$
Y	WR02	$325 - 500\,\mathrm{GHz}$
Y	WR01.5	$500 - 750\,\mathrm{GHz}$

For this purpose, this section provides margins for the root-mean-square (RMS) roughness R_q which meet these requirements over the frequency bands from W- to Y-Band as shown in Table 9 in terms of both, a general consideration and specific application to certain transmission lines.

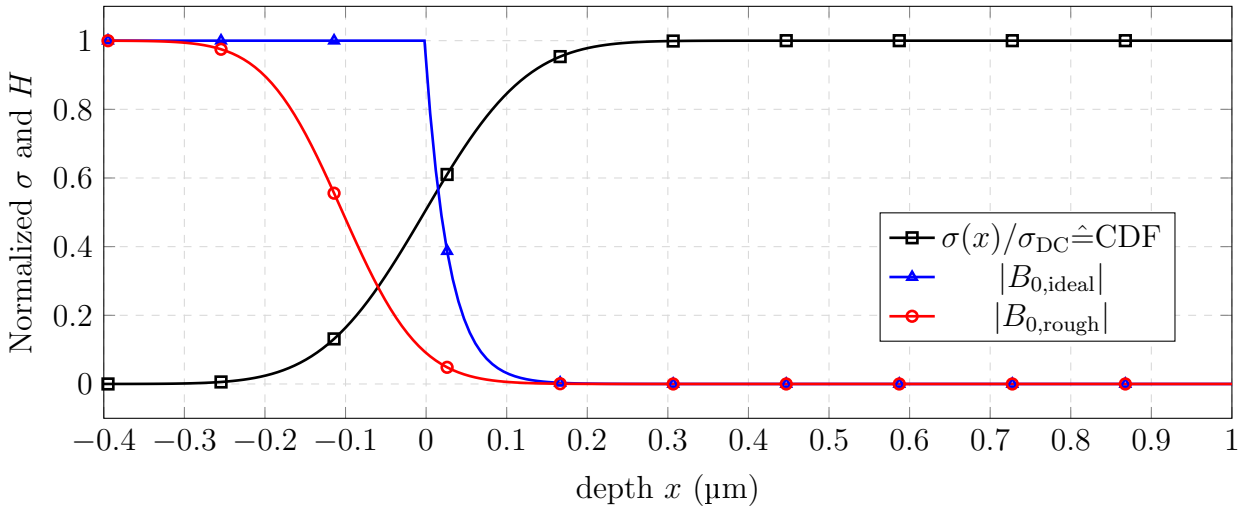

Figure 20 Conductivity profile and skin effect on smooth and rough surface at 50 GHz with $R_q = 1\,\mu\mathrm{m}$

By making use of the Gradient Model [46], the penetrating magnetic field can be calculated for a given surface which is represented either by a measured bearing area curve (BAC) or R_q as shown in Fig. 20. As explained in [46], these responses may be used to derive effective material parameters which in turn account for the impact of surface roughness in transmission line models such as e.g. [45] for a CPW or [47] for rectangular waveguides (RWG).

While the magnitude and ratio of surface roughness impact on α and v_{ph} depend on the type, specific cross section geometry and materials of the transmission line, the surface impedance as described in [46] provides an independent approach for illustration and comparison:

$$Z_{\square} = \frac{1}{\sigma_{\mathrm{eff}}\delta\left(\sigma_{\mathrm{eff}}\right)} + j\frac{1}{\sigma_{\mathrm{DC}}\delta\left(\mu_{\mathrm{r,eff}}\right)} = \sqrt{\frac{\pi\mu_0\mu_{\mathrm{r}}f}{\sigma_{\mathrm{eff}}}} + j\sqrt{\frac{\pi\mu_0\mu_{\mathrm{r,eff}}f}{\sigma_{\mathrm{DC}}}} = R_{\square} + j\omega L_{\mathrm{i},\square} \qquad (1)$$

where σ_{DC} is the bulk conductivity as a material property of the conductor (e.g. 58 MS/m in case of bulk copper) and σ_{eff} and $\mu_{\mathrm{r,eff}}$ denote effective, frequency dependent material

parameter values derived from the Gradient Model approach which represent the impact of surface roughness. While the real part of $Z_\square$ affects the attenuation and is therefore related to $R_\square$, its imaginary part influences v_{ph} and is related to $L_{\mathrm{i},\square}$, which is the inner inductance.

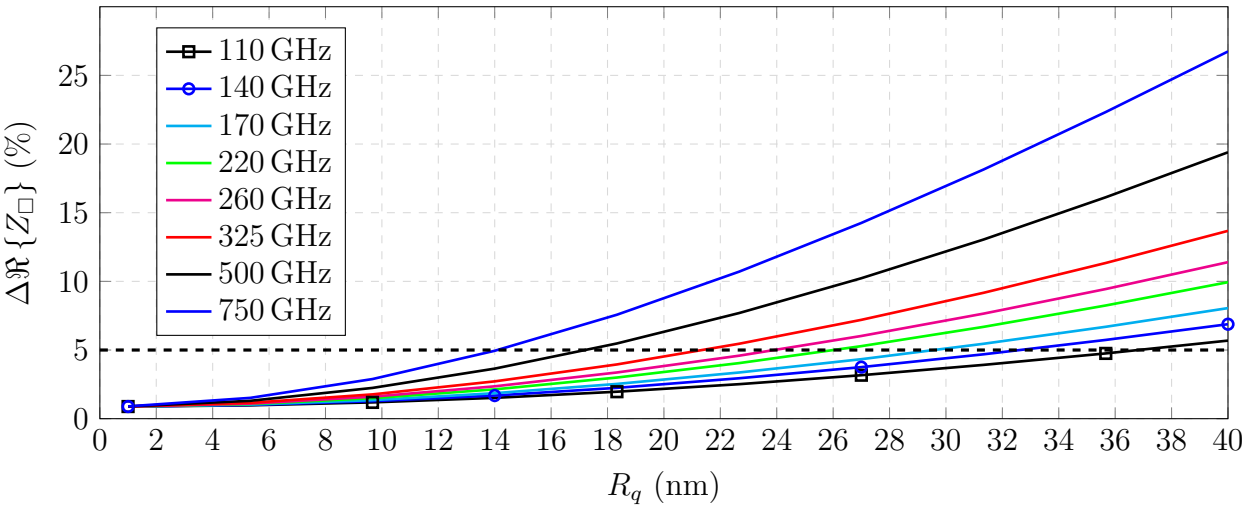

Figure 21 Relative deviation $\Delta\Re\{Z_\square\}$ between rough and smooth case in %

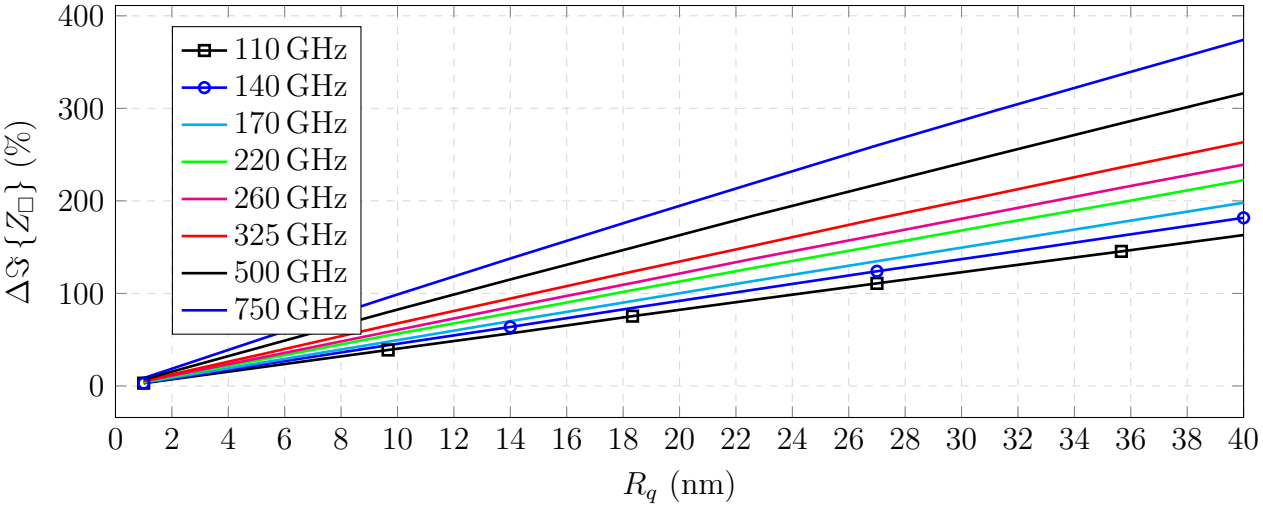

Figure 22 Relative deviation $\Delta\Im\{Z_\square\}$ between rough and smooth case in %

Figs. 21 and 22 show the relative deviation between the rough and smooth $Z_\square$ depending on R_q for the considered frequency band limits. From the real part, a 5 % margin can therefore be derived for each band, indicating the need for lower R_q with increasing operation frequencies.

Although the deviation within the imaginary part of $Z_\square$ in Fig. 22 exceeds 100 % for relatively small R_q already, it is worth to mention, that it only contributes to the inner inductance term L_i which is much smaller than the outer inductance L_o ($L_i \ll L_o$) and is therefore only a fraction of the total inductance for most practical transmission lines. Furthermore, the 5 % limit in $\Re\{Z_\square\}$ is not directly related to the attenuation of a specific transmission line, since the conductor circumference must be considered according to the cross section geometry [48].

While the layout of a CPW allows for various implementations depending on the substrate material, manufacturing aspects and others, rectangular waveguides are typically produced

in standardized dimensions according to their identifier WR-XX in Table 9. This allows for precise predictions of the surface roughness impact which is shown in Figs. 23 and 24.

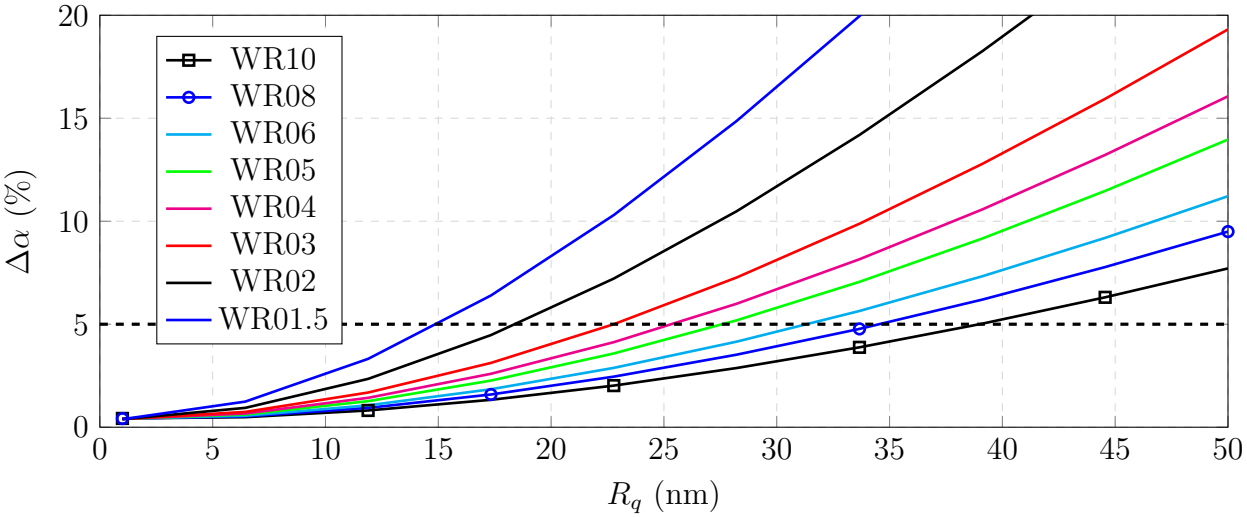

Figure 23 Relative deviation $\Delta\alpha$ between rough and smooth RWG in %.

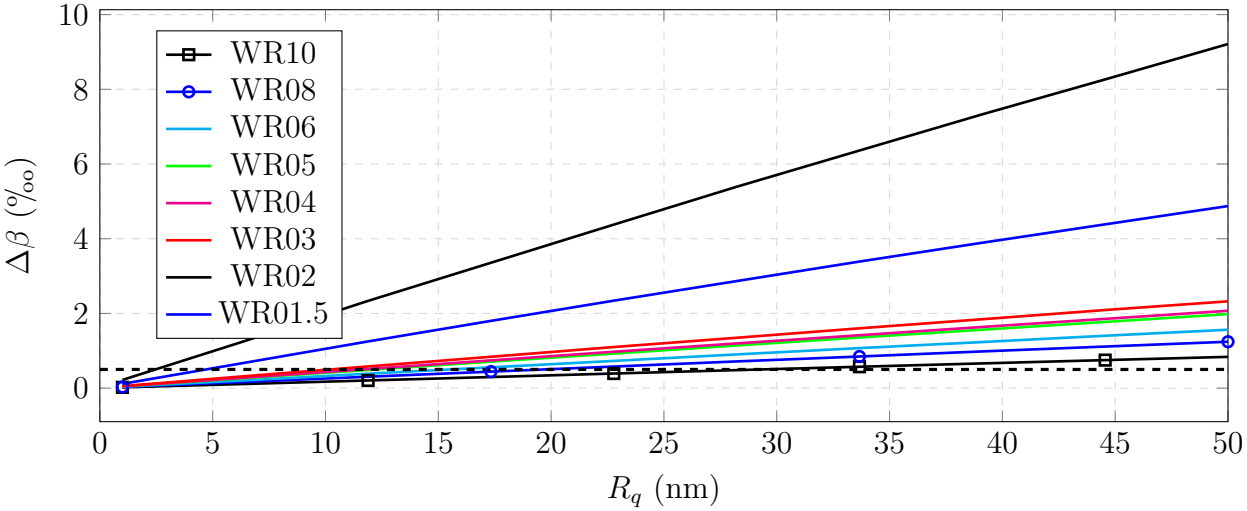

Figure 24 Relative deviation $\Delta\beta$ between rough and smooth RWG in ‰.

Note, that the deviation in β is provided in ‰ as it is rather small as compared to the impact on α. However, it comes along with a small shift of the cutoff frequency f_c towards lower values.

The R_q-margins for CPWs can be provided for certain cases only, since CPW lines can be fabricated in a much greater variety compared to standardized RWG. Exemplarily, a CPW implemented on Al_2O_3 substrate ($\varepsilon_r = 9.7$) is considered with the cross section geometry as provided in Fig. 25.

In addition to the phase coefficient β, in this case, also the effective relative permittivity is considered according to:

$$\varepsilon_{\mathrm{r,eff}} = \left(\frac{c_0}{v_{\mathrm{ph}}}\right)^2 \tag{2}$$

The corresponding R_q margins are provided in Figs. 26 to 31 for attenuation and phase coefficient for different substrate thicknesses of $h = 100\,\mu\mathrm{m}$ and $h = 10\,\mathrm{mm}$, respectively.

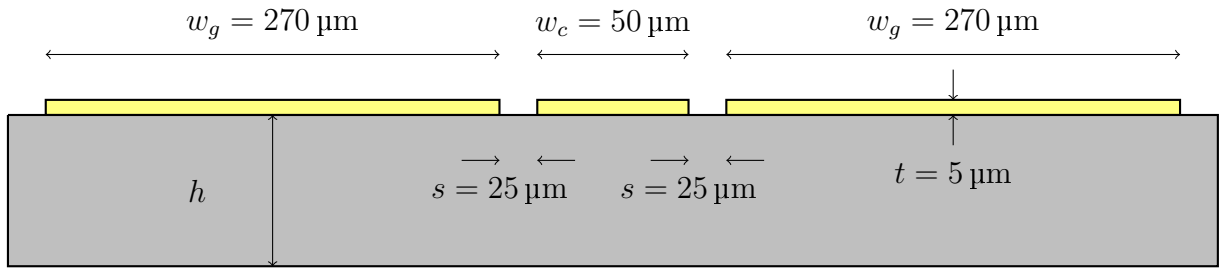

Figure 25 Cross section geometry of a CPW structure as considered in this comparison.

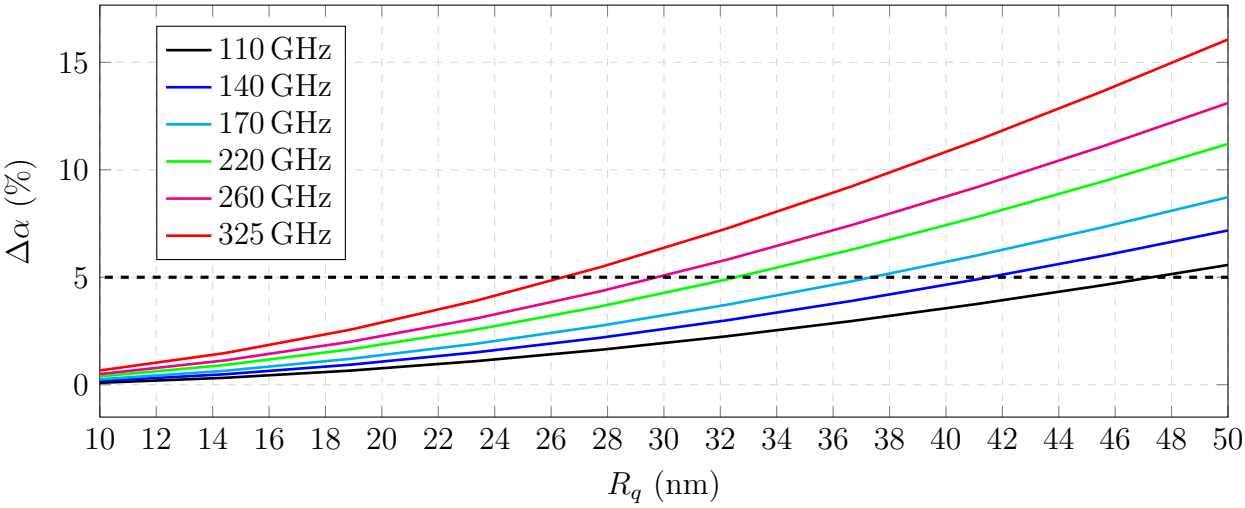

Figure 26 Relative deviation $\Delta\alpha$ between rough and smooth CPW in % for $h = 100\,\mu\text{m}$.

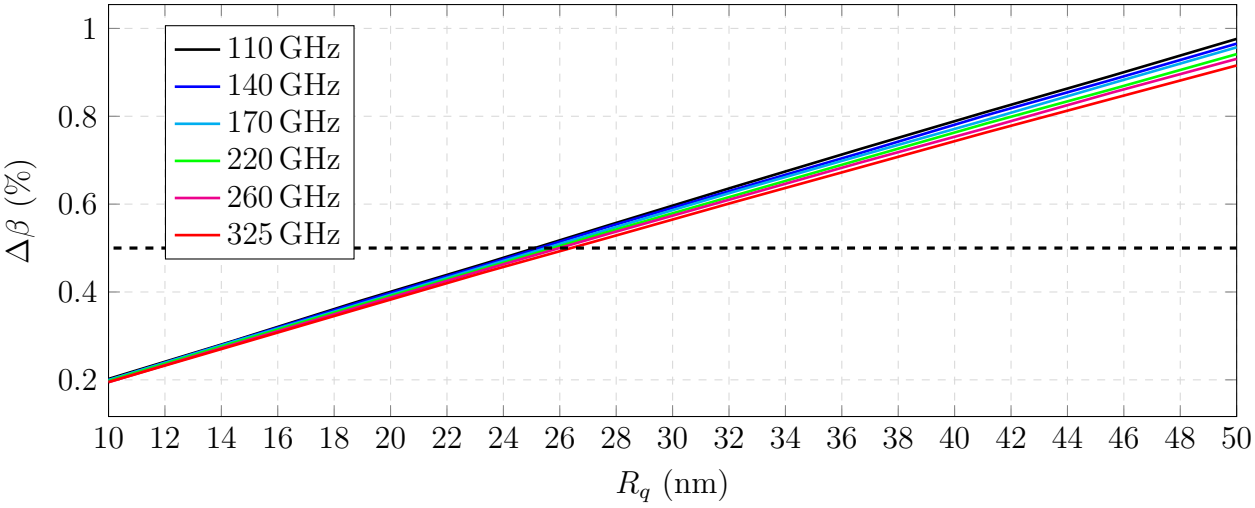

Figure 27 Relative deviation $\Delta\beta$ between rough and smooth CPW in % for $h = 100\,\mu\text{m}$.

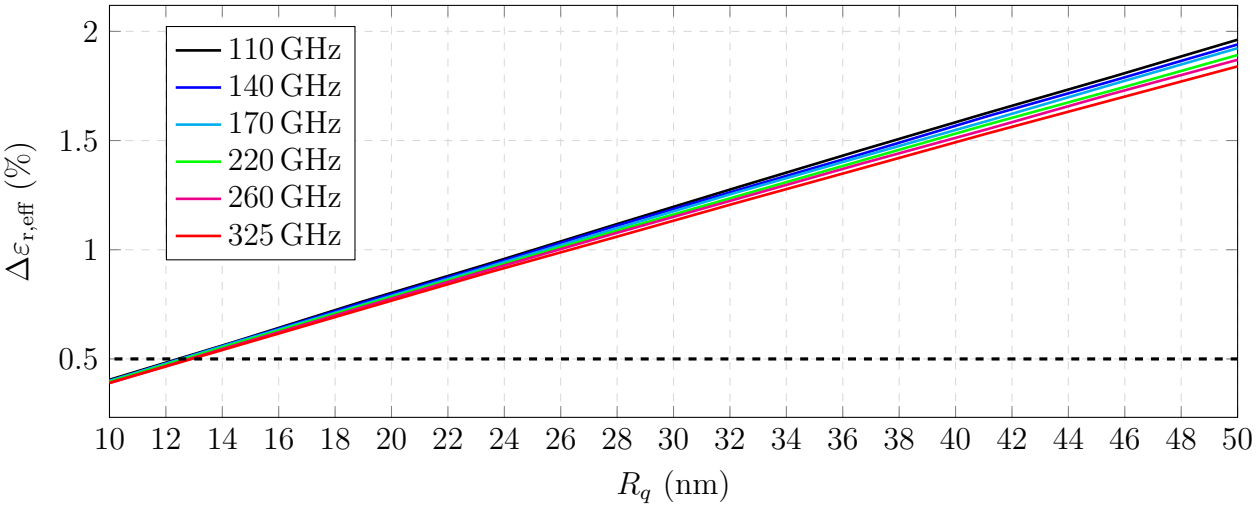

Figure 28 Relative deviation $\Delta\varepsilon_{r,eff}$ between rough and smooth CPW in % for $h = 100\,\mu m$.

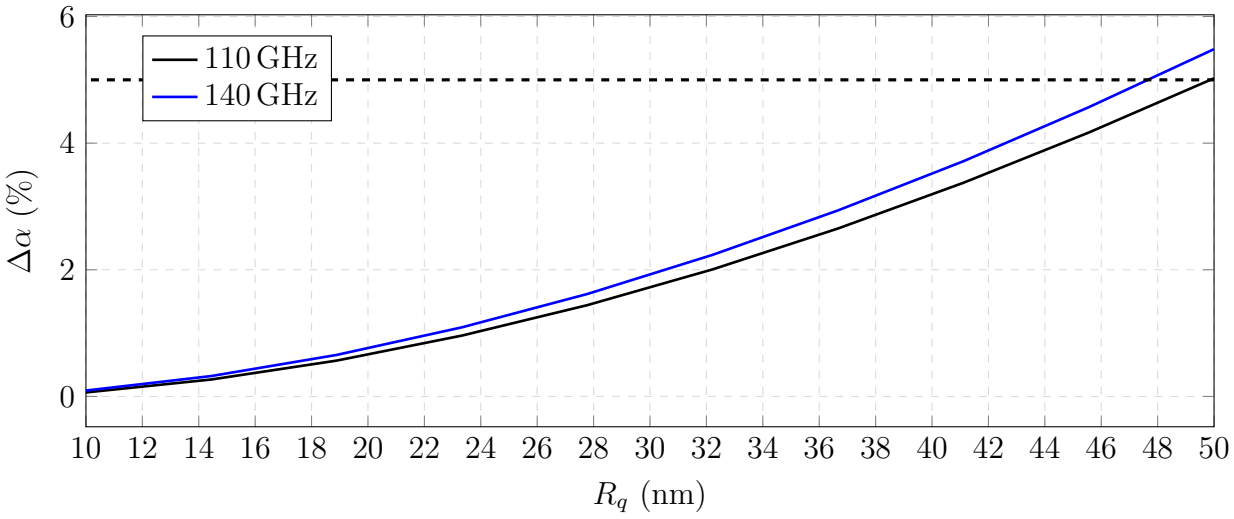

Figure 29 Relative deviation $\Delta\alpha$ between rough and smooth CPW in % for $h = 10\,mm$.

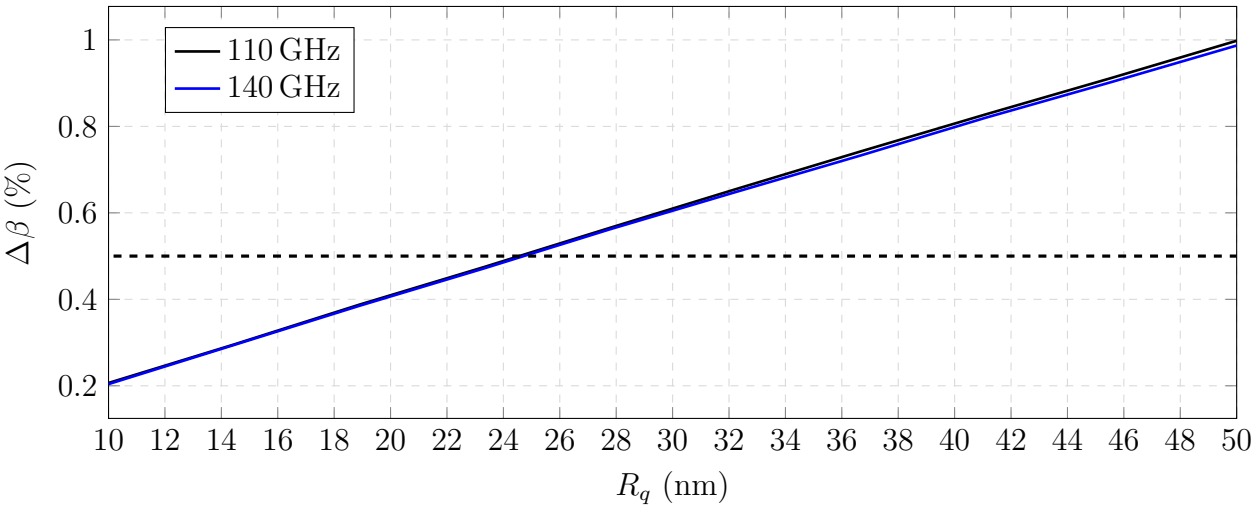

Figure 30 Relative deviation $\Delta\beta$ between rough and smooth CPW in % for $h = 10\,mm$.

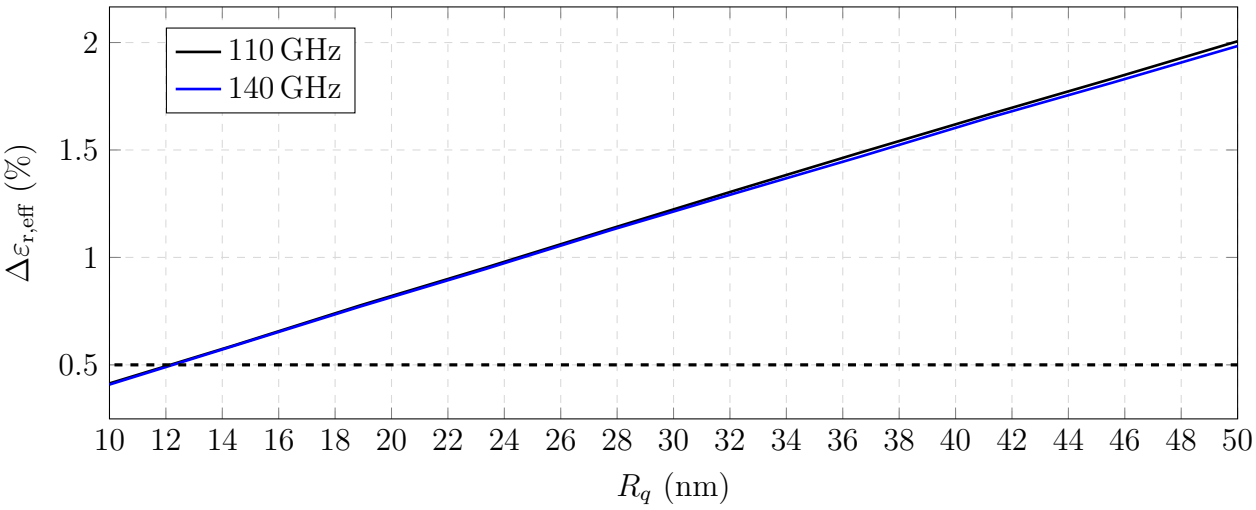

Figure 31 Relative deviation $\Delta\varepsilon_{\mathrm{r,eff}}$ between rough and smooth CPW in % for $h = 10\,\mathrm{mm}$.

3.4 Importance of positioning accuracy

Conventional RF test structures require probing pads whose dimensions are around $50\times50\ \mu m^2$ to accommodate the probe tip geometry (example: pitch of 100 μm, contact area of $30\times30\ \mu m^2$). The manual positioning of the probe onto the CPW test structure generates misalignment measurement errors that impact notably on the measured impedance. In particular, these measurement errors increase in the millimeter-wave and sub-millimeter-wave regimes. The positioning accuracy is also crucial when measurement of high impedance devices such as nanoscale structures are considered. Indeed, phase-shift and magnitude errors inherent to the positioning accuracy offset the impedance to be measured. Consequently, piezo-based nano-positioning (X-Y-Z controls) and strain-sensing (Z control) strategies are used to provide automated and accurate control of the probe landing onto the test structure [49, 50].

4 Nanodevice measurements

4.1 Solving the impedance mismatch problem

Vector network analyzers have been introduced in the seventies to measure the electrical properties of materials and circuits. Since then, there has been considerable work to extend their measurement capabilities such as frequency coverage from low RF to hundreds of GHz, multi-port devices characterization, balanced, differential, harmonic, modulation and pulsed measurements. Nowadays, there is an urgent need to further extend the network analyzer capabilities to meet the specific needs of characterization tools for impedances clearly higher than the 50 Ω reference impedance of the VNA. In particular, the electrical characterization of high impedance nanodevices is a well-known scientific challenge. The main measurement limitation in these applications is the impedance mismatch between the reference impedance of the network analyzer close to 50 Ω that is too different compared to the impedance of nanodevices that is in the range of tens or hundreds of $k\Omega$. Indeed, when high impedances are considered, the VNA is insensitive to the variations of the reflection coefficient.

The issue of dealing with extreme impedance measurement has yielded a variety of measurement techniques. In 2005, the first measurements of the high frequency conductance of a metallic single walled nanotube (SWNT) with resistance below 200 $k\Omega$ inserted in a coplanar waveguide (CPW) transmission line were performed up to 10 GHz [51]. In 2010, to improve the VNA sensitivity, an individual SWNT iwas inserted in a specific high impedance Wheatstone bridge that helps to reduce the impedance mismatch between the VNA and the high-impedance nanodevice [52].

Among the alternatives to these studies, the interferometric principle commonly used in optics through Michelson or Mach Zender configurations has gained the interest from the microwave research community to measure small complex impedance contrasts. Basically, a monochromatic signal is split with one part traveling a fixed path and the other a variable one. The two resulting signals are reunited, amplified if necessary, and produce the well-known interference. In 1949, a Michelson-type microwave interferometer was introduced for the first time at the free-space wavelength of 3.2 cm for free-space dielectric characterization [53]. In 2007, microwave interferometry was applied for the first time to the measurement of high impedance devices around 1.8 GHz [54, 55]. In particular, the setup included a vector network analyzer interfaced with an interferometric setup built up with a hybrid coupler associated to low noise amplifiers. In 2011, a mechanically tunable interferometric matching network in the range 1-18 GHz built up with a power divider, a variable attenuator and a sliding-short was applied to high impedance measurements [56]. To further enhance the sensitivity in a broadband frequency range, an interferometer built up with a high-resolution programmable delay line and a motor-driven variable attenuator has been developed [57]. In 2015, an I/Q-mixer-based interferometric technique is developed for speed operation [58]. These studies have proven that RF interferometric techniques are candidates to tackle the problem of impedance mismatch.

The recommendation for high impedance measurements is to insert a tuning matching network between the measurement port of the vector network analyzer and the measurement of the port of the device under test. The tuning matching network based on microwave interferometry remains the most efficient method. This latter can be built up easily with coaxial or guided commercial equipment (couplers, power dividers, variable attenuators and phase-shifters). In addition, the method offers broadband frequency measurements.

4.2 Addressing the scale mismatch challenge

There is a natural dimensional mismatch between the size of the nanodevices and the wavelength of operation in the microwave and millimeter-wave regimes. In the RF spectrum spanning from 1 to 300 GHz, the spatial resolution is on the order of the centimeter/millimeter whereas the size of the device is in the micrometer/deca-nanometer ranges. In addition, conventional RF test structures require probing pads whose dimensions are around 50×50 μm^2 to accommodate the probe tip geometry (example: pitch of 100 μm, contact area of 30×30 μm^2). Consequently, the CPW structures must be tapered to low dimensions to connect the nano-device under investigation [51, 59]. Consequently, dedicated calibration structures with tapered dimensions and related calibration protocols must be adapted for determination of the RF impedance in the nano-device reference plane [49]. In this measurement configuration, the mechanical repeatability of the probe to test structure contact will affect drastically the measurement accuracy. It has to be mentioned that miniaturization of the GSG probing structure is an efficient solution to address direct probing at the nanoscale. Such method is still under development at the lab scale and is a promising solution to enhance the measurement accuracy. On-wafer measurements at the nanoscale make use of home-made GSG probes in silicon technology mounted on piezo-based nanopositionners and operating inside a scanning electron microscope [60, 61, 62].

The recommendation for CPW measurement at the nanoscale is to use piezo-based nanopositioning (X-Y-Z controls) to provide automated and accurate control of the probe landing onto the test structure. Dedicated CPW calibration structures and test structures must be designed to accommodate both the probe and nanodevice sizes. In addition, it is highly recommended to use e-beam lithography nanofabrication methods to achieve accurate control of the targeted dimensions. Indeed, the resulting de-embedding process is affected by the technological process variations.

4.3 Interferometric methods

A zero-reflected wave condition provides the smallest noise in S-parameter measurements of a generic DUT. To reach this wave condition, several RF interferometric techniques have been developed [63, 56, 58, 64] all aiming at cancelling the scattered $\mathbf{b}_{dut}$-wave generated by the (high $|\boldsymbol{\Gamma}_{dut}|$) DUT through the injection of an additional, compensating $\mathbf{b}_{int}$-wave signal.

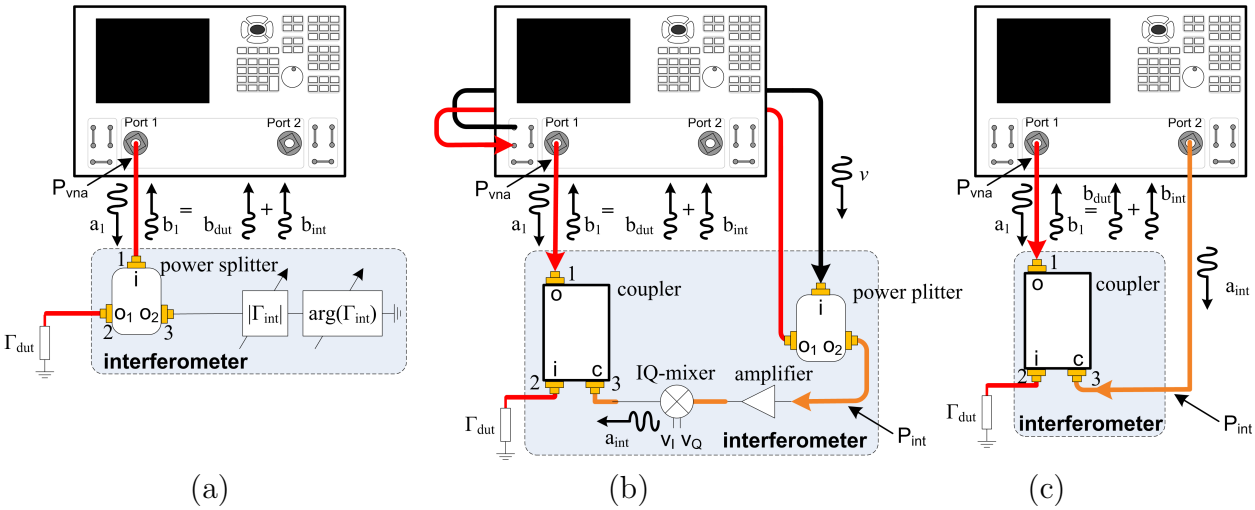

Figure 32 Schematic representations of three methods for interferometric noise suppression in $\boldsymbol{\Gamma}$ measurements: (a) single-source passive method [56], (b) single-source active method [58], (c) dual-source active method [64]. Fundamental parts in each interferometer are the 3-port signal combining component and the signal source.

Fig. 32 gives a schematic overview of the main approaches presented to date in literature.

To compare the noise-improvement performance of these various interferometric techniques, a generalized flow-graph representation is given in Fig. 33, which includes the required signal combining device to realize the RF interferometer and the relative phase fluctuations between different waves.

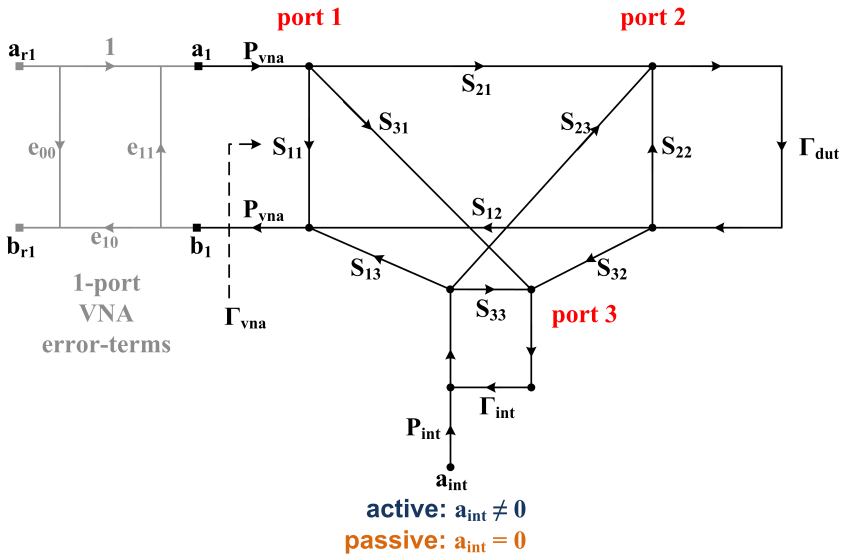

Figure 33 Flow-graph of a 1-port VNA with interferometric cancellation of the $\mathbf{b}_1$-wave using a 3-port signal-combining device. Port-2 serves as new test-port of the VNA and port-3 induces the phase-coherent $\mathbf{a}_{int}$-wave for $\mathbf{b}_1$-wave cancellation.

With this flow-graph representation both passive ($\mathbf{a}_{int} = 0$) and active interferometers ($\mathbf{a}_{int} \neq 0$) can be analyzed, as well as both classes of passive devices used as signal combining network, i.e., power dividers and transmission line couplers. The VNA is connected to the input of port-1, as shown in Fig. 33. Using classical flow-graph manipulation techniques [65, 66], the Γ_{vna}, Γ_{dut}, Γ_{int} and the various S-parameters of the combining network can be mutually related to each other.

4.3.1 Passive methods

Passive interferometric noise-reduction techniques rely on replicating the scattered **b**-wave generated by DUT reflection coefficient through a passive device (i.e., tuner). The parameter $\mathbf{a}_{int}$ in Fig. 33 thus is zero and Γ_{int} is providing the cancellation condition.

The S-parameters of the combining network given in Fig. 33 can be linked via:

$$\begin{aligned}
\Gamma_{vna} = \frac{b_1}{a_1} = P_{vna}^2 (S_{11} + 2\beta \sum_{n=1}^{\infty} \alpha^{2n-1} A^n B^n + \cdots \\
. + S_{21}^2 \sum_{n=1}^{\infty} \alpha^{2(n-1)} A^n B^{n-1} + S_{31}^2 \sum_{n=1}^{\infty} \alpha^{2(n-1)} A^{n-1} B^n) + . \\
\cdots + \frac{a_{int}}{a_1} P_{int} P_{vna} (S_{13} + S_{12} \sum_{n=1}^{\infty} \alpha^{2n-1} A^n B^{n-1} + \cdots \\
\cdots + S_{13} \sum_{n=1}^{\infty} \alpha^{2n} A^n B^n)
\end{aligned} \tag{3}$$

With:

$$A = \frac{\Gamma_{dut}}{1 - S_{22}\Gamma_{dut}} \qquad B = \frac{\Gamma_{int}}{1 - S_{22}\Gamma_{int}}$$

If we furthermore assume that:

$$n = 2 \quad S_{i,j} = S_{j,i} \quad \alpha = S_{23} = S_{32} \quad \beta = S_{21}S_{13} = S_{31}S_{12}$$

(3) can be expressed as follows:

$$\begin{aligned}
\Gamma_{vna} &= S_{11}P_{vna}^2 + S_{31}^2 B P_{vna}^2 + S_{13}\frac{a_{int}}{a_1}P_{int}P_{vna} + \cdots \\
&\cdots + A\big(S_{12}\alpha\frac{a_{int}}{a_1}P_{int}P_{vna} + 2\beta\alpha B P_{vna}^2 + S_{21}^2 P_{vna}^2 + . \\
&\cdots + S_{31}^2\alpha^2 B^2 P_{vna}^2 + S_{13}\alpha^2 B\frac{a_{int}}{a_1}P_{int}P_{vna}\big) + \cdots \\
&\cdots + A^2\big(2\beta\alpha^3 B^2 P_{vna}^2 + S_{21}^2\alpha^2 B P_{vna}^2 + \cdots \\
&\cdots + S_{12}\alpha^3 B\frac{a_{int}}{a_1}P_{int}P_{vna} + S_{13}\alpha^4 B^2\frac{a_{int}}{a_1}P_{int}P_{vna}\big)
\end{aligned} \tag{4}$$

In this case (4) simplifies to:

$$\begin{aligned}
\Gamma_{vna} &= S_{11}P_{vna}^2 + S_{31}^2 B P_{vna}^2 + S_{21}^2 A P_{vna}^2 + \big(2\beta\alpha B + S_{31}^2\alpha^2 B^2\big)A P_{vna}^2 + .. \\
&.. + \big(2\beta\alpha^3 B^2 + S_{21}^2\alpha^2 B\big)A^2 P_{vna}^2
\end{aligned}$$

And can be re-written as:

$$\Gamma_{vna} = \ S_{11}P_{vna}^2 + S_{31}^2 B P_{vna}^2 + S_{21}^2 A P_{vna}^2 + X_1 A P_{vna}^2 + X_2 A^2 P_{vna}^2 \tag{5}$$

In the cancellation condition (i.e., $\mathbf{b}_1 = 0$) this leads to:

$$a_1\big(S_{11} + S_{21}^2 A\big) + \big(X_1 A + X_2 A^2\big) = -a_1 S_{31}^2 B \tag{6}$$

The sensitivity ratio ($\partial\boldsymbol{\Gamma}_{vna}/\partial\boldsymbol{\Gamma}_{dut}$) is

$$\begin{aligned}
\frac{\partial\Gamma_{vna}}{\partial\Gamma_{dut}} &= \frac{S_{21}^2 P_{vna}^2 + 2\beta\alpha B P_{vna}^2 + \frac{a_{int}}{a_1}S_{12}\alpha P_{int}P_{vna}}{1 - S_{22}} + . \\
&\cdots + \frac{S_{31}^2\alpha^2 B^2 P_{vna}^2 + \frac{a_{int}}{a_1}S_{13}\alpha^2 P_{int}P_{vna}}{1 - S_{22}} + \cdots \\
&\cdots + \frac{2\Gamma_{dut}\big(2\beta\alpha^3 B^2 P_{vna}^2 + S_{21}^2\alpha^2 B P_{vna}^2}{1 - 2S_{22} - 2S_{22}^2\Gamma_{dut}} + \cdots \\
&\cdots + \frac{\frac{a_{int}}{a_1}S_{12}\alpha^3 B P_{int}P_{vna} + \frac{a_{int}}{a_1}S_{13}\alpha^4 B^2 P_{int}P_{vna}\big)}{1 - 2S_{22} - 2S_{22}^2\Gamma_{dut}} \quad .
\end{aligned} \tag{7}$$

From the evaluation of (7), it is evident that the sensitivity ratio ($\partial \boldsymbol{\Gamma}_{vna}/\partial \boldsymbol{\Gamma}_{dut}$) cannot exceed 1 for passive techniques due to transmission path losses. Furthermore, realizing high sensitivity for $\partial \boldsymbol{\Gamma}_{dut}$ requires transmission losses $\mathbf{S}_{21}$ to be minimal, see (5) and (6). In addition, the losses between the input and both output ports of the passive device need to be comparable ($\mathbf{S}_{21} \approx \mathbf{S}_{31}$), due to the limited magnitude of the reflection coefficient that can be provided (i.e., $|\boldsymbol{\Gamma}_{int}| < 1$) for cancellation. For this reason, it is not possible to use a broadband directional coupler to realize passive cancellation for DUTs presenting a $|\boldsymbol{\Gamma}_{dut}|$ higher than 0.1 due to the large difference between transmission and coupling losses, i.e., $\mathbf{S}_{21} >> \mathbf{S}_{31}$. The dual condition is not considered ($\mathbf{S}_{21} << \mathbf{S}_{31}$), as this would provide very low sensitivity ($\partial \boldsymbol{\Gamma}_{vna}/\partial \boldsymbol{\Gamma}_{dut}$). This effect is illustrated by using parameters of commercially available directional couplers in calculating (7) with the results shown in Fig. 34. It is evident that cancellation is only possible for $\boldsymbol{\Gamma}_{dut}$ up to 0.1 (solid line), while the remaining $\boldsymbol{\Gamma}_{dut}$-region (dotted line) is not reachable due to the passive nature of the tuner. Due to this constraint, most passive RF interferometers use power dividers, e.g., a Wilkinson power-divider [56], Fig. 32(a).

For accurate measurements over the entire range of $\boldsymbol{\Gamma}_{dut}$ values, the measurement resolution has to be constant. However, a non-zero $\mathbf{X}_1$ and $\mathbf{X}_2$ in (6) leads to unwanted $\boldsymbol{\Gamma}_{dut}$ and $\boldsymbol{\Gamma}_{int}$ dependent cross leakage, limiting the sensitivity. Hence, $\boldsymbol{\alpha}$ remains a critical parameter of the 3-port combining devices used in passive interferometers. To investigate the impact of $\boldsymbol{\alpha}$ on the measurement sensitivity, parameters of a commercially available power divider are used for calculation of (7) with the results shown in Fig. 34. Clearly, the power-divider approach suffers more from the unwanted cross talk between the two combining ports ($\boldsymbol{\alpha}$), reducing the measurement resolution. However, unlike the directional coupler, the power divider can achieve cancellation for the entire range of $\boldsymbol{\Gamma}_{dut}$ values.

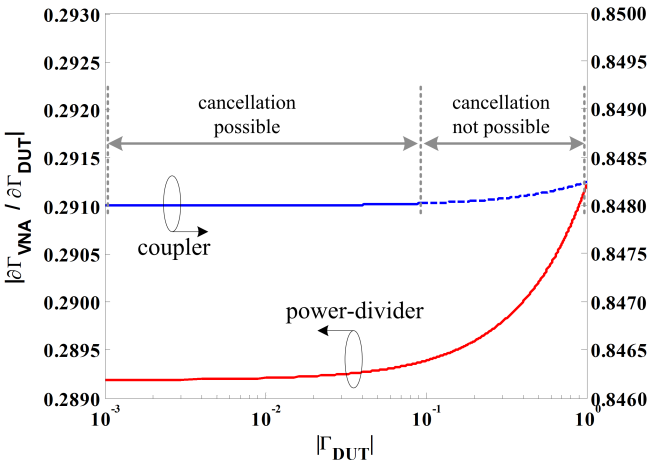

Figure 34 Simulation results for two different implementations of the 3-port signal-combining device used in passive interferometers, showing the sensitivity of the input reflection coefficient measured with the VNA ($\boldsymbol{\Gamma}_{vna}$) to variations in device reflection coefficient at the measurement port of the interferometer ($\boldsymbol{\Gamma}_{dut}$).

4.3.2 Active Methods

Active interferometric noise suppression is realized via the injection of an $\mathbf{a}_{int}$-wave (see Fig. 33) generated by employing active components. This can be either an IQ-steering technique [58] shown in Fig. 32(b) or a second, phase coherent, source [64] as shown in Fig. 32(c). Hence, active techniques are not limited to the constraint of $\mathbf{S}_{21} \approx \mathbf{S}_{31}$, required by passive ones, thus employ coupled line coupler as the combining device due to the reduced $\boldsymbol{\alpha}$, as shown in Fig. 34. If we include the effect of the relative (phase) fluctuations between the

signals $\mathbf{a}_1$ and $\mathbf{a}_{int}$ in (4) and those arising from the different propagation paths, equation becomes:

$$\begin{aligned} b_1 =& a_1\big(S_{11} + S_{21}^2 A + S_{31}^2 B + 2\beta\alpha BA + S_{31}^2\alpha^2 B^2 A + .. \\ & .. + 2\beta\alpha^3 B^2 A^2 + S_{21}^2\alpha^2 BA^2\big) P_{vna}^2 + .. \\ & a_{int}\big(S_{13} + S_{12}\alpha A + S_{13}\alpha^2 BA + S_{12}\alpha^3 BA^2 + .. \\ & .. + S_{13}\alpha^4 B^2 A^2\big) P_{int} P_{vna} \end{aligned}$$

This can be re-written as:

$$b_1 = a_1 K P_{vna}^2 + a_{int} L P_{int} P_{vna} \tag{8}$$

Single- and dual-source interferometers

Single-source interferometers have one signal source $\boldsymbol{\nu}$ that generates $\mathbf{a}_1$ and $\mathbf{a}_{int}$ signals [58], Fig. 32(b). The relation between $\boldsymbol{\nu}$ and both signals can be expressed as follows:

$$a_1 = \nu\ P_{vna}^*$$

$$a_{int} = \nu\ G_{int}\ P_{vna}^* \tag{9}$$

Here, $\mathbf{G}_{int}$ is the active gain needed to compensate for the various losses introduced by the couplers, cables and passive IQ-mixers. Furthermore, $\mathbf{P}_{vna}$ and $\mathbf{P}_{vna}^*$ present two distinct parts of the $\mathbf{a}_1$-wave signal path, where $\mathbf{P}_{vna}^*$ is also shared by $\mathbf{a}_{int}$-wave signal. This single-source method is realized by splitting the $\boldsymbol{\nu}$ signal before measurement of the $\mathbf{a}_1$-wave and $\mathbf{b}_1$-wave signals, see Fig. 32(b). The disadvantage of this method is that it suffers from separate routing of $\mathbf{a}_1$ and $\mathbf{a}_{int}$ signals, requiring the use of lengthy cables, denoted with $\mathbf{P}_{vna}$, $\mathbf{P}_{vna}^*$ and $\mathbf{P}_{int}$ in Fig. 32(b). Since the noise and drift effects of VNA test-port cables can be much larger than the VNA noise, the stability of both cables significantly limits the performance of this approach. For single-source based cancellation ($\mathbf{b}_1 = 0$), (8) can be expressed as:

$$\nu\ K\ P_{vna}^2\ P_{vna}^* = \nu\ G_{int}\ L\ P_{int}\ P_{vna}\ P_{vna}^* \tag{10}$$

In (10), the left side of the equations represents the scattered wave generated by Γ_{dut}, whereas the right side of the equation represents the scattered wave generated by the interferometer. From (10) it is evident that the cancellation condition is insensitive to variations in the $\boldsymbol{\nu}$ source. However, as both scattered waves travel through independent paths, the cancellation condition is also sensitive to unwanted instability effects originating from the use of two different cable paths $\mathbf{P}_{vna}$, $\mathbf{P}_{vna}^*$ and $\mathbf{P}_{int}$, respectively.

A similar analysis can be applied to evaluate dual-source interferometer [64] where two separate signal sources are used to generate $\mathbf{a}_1$ and $\mathbf{a}_{int}$, see Fig. 32(c). Hence, for cancellation ($\mathbf{b}_1 = 0$), (8) now becomes:

$$a_1\ K\ P_{vna}^2 = -a_{int}\ L\ P_{int}\ P_{vna} \tag{11}$$

This approach also suffers from the use of lengthy cables as separate routing of the $\mathbf{a}_1$ and $\mathbf{a}_{int}$ signals is unavoidable. An additional problem with respect to the single-source method are uncorrelated noise and drift effects originating from the different signal sources.

Simulation evaluation

To validate the **b**-wave cancellation capabilities of both active interferometric methods, (10) and (11) are evaluated via Monte Carlo simulations conducted in Advanced Design System (ADS) software. To investigate the effect of non-ideal cables and signal sources, parameter variations are assigned to the magnitude and phase components of cable paths and signal sources. The variations in cable parameters are based on an evaluation technique outlined in [67]: the magnitudes of $\mathbf{P}_{vna}$, $\mathbf{P}_{int}$, $\mathbf{a}_1$ and $\mathbf{a}_{int}$ are varied by 0.01 % and their corresponding phases are varied by 0.2 deg (both Gaussian distributions).

For the single-source interferometer, the cancellation sensitivity of (10) is investigated by propagating variations assigned to $\mathbf{P}_{vna}$ combined with $\mathbf{P}^*_{vna}$, $\mathbf{P}_{int}$ and $\mathbf{a}_1$. For the dual-source method, the cancellation sensitivity is investigated by (11) via propagating variations assigned to $\mathbf{P}_{vna}$, $\mathbf{P}_{int}$, $\mathbf{a}_1$ and $\mathbf{a}_{int}$. The results are shown in Fig. 35.

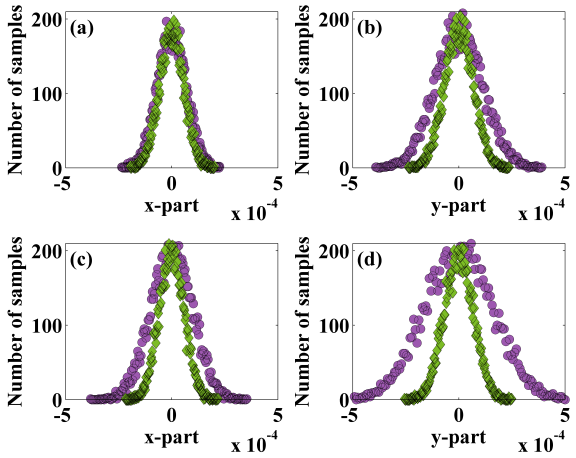

Figure 35 Monte Carlo noise simulation results from [68] for two active interferometric techniques, detailing **b**-wave cancellation sensitivity for single-source (green diamonds) and dual-source (purple circles) interferometers. In (a) and (b), the complex **b**-wave cancellation discrepancies caused by variations of cable parameters are shown. While, (c) and (d) show **b**-wave complex cancellation discrepancies caused by variations of cable and source parameters.

In Fig. 35(a)-(b), the complex **b**-wave cancellation discrepancies caused by propagation of cable parameter variations are shown. The simulation results show that the single-source method has slightly lower noise compared to the dual-source technique. The reason that the single-source method of Fig. 32(b) has marginally better noise than the dual-source method of Fig. 32(c), is the shared cable $\mathbf{P}^*_{vna}$ path in the single-source configuration.

The **b**-wave cancellation discrepancies shown in Fig. 35(c)-(d) are predominantly noticeable, when propagating $\mathbf{a}_1$ and $\mathbf{a}_{int}$ signal parameter variations combined with cable parameter variations. As expected, the **b**-wave cancellation condition for single-source configuration is insensitive to $\mathbf{a}_1$ and $\mathbf{a}_{int}$ signal parameter variations originating from $\boldsymbol{\nu}$.

Measurement comparison

As a further evaluation of the two active interferometer types, a measurement of single- and dual-source interferometers was carried out using a 4-port Keysight PNA-X (PNA5257A). This VNA has two signal sources and allows individual control of magnitude and phase components. First, stability between both signal sources used by dual-source interferometer is evaluated. Like [64], port-1 and port-3 of the VNA provide $\mathbf{a}_1$ and $\mathbf{a}_{int}$ signals, with amplitude and phase control of each signal source available through the firmware (option: 080) of the PNA-X. Both signals are subsequently measured by the receivers of port-2 and

port-4. Subsequently, the stability between $\mathbf{a}_1$ and $\mathbf{a}_{int}$ signals in single-source interferometer is evaluated using port-1 of the VNA to provide the $\mathbf{a}_1$ signal source and to serve as input for the single-source interferometer as shown in Fig. 32(b). Again, both signals are subsequently measured by the receivers of port-2 and port-4.

In both experiments, the power level of each signal source is set to -10 dBm, and subsequently $20 \cdot 10^3$ measurement values are extracted at 3 GHz from both receivers (port-2 and port-4). From these values, the ratio $\mathbf{a}_{int}/\mathbf{a}_1$ is calculated and normalized to demonstrate the stability between the two signals.

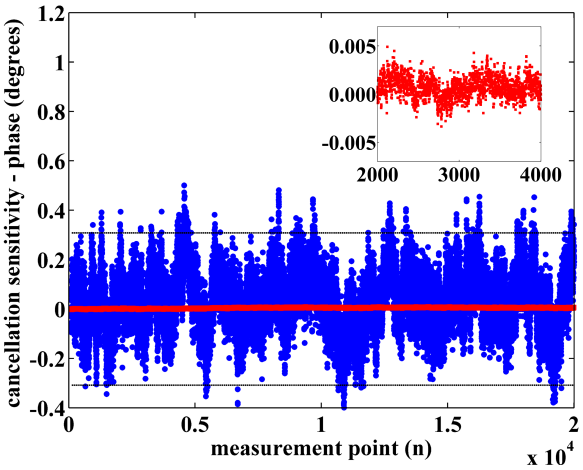

Figure 36 Measurement results from [68] showing the cancellation sensitivity for the phase-component realized with two active interferometer topologies at 3 GHz (dual-source: blue circles; single-source: red squares, and inset). The black line depicts phase-component stability of **b**-wave measured using method outlined in (9).

The linear magnitude stability of $\mathbf{a}_{int}/\mathbf{a}_1$ for both methods is found to be comparable and smaller than $1 \cdot 10^{-4}$. The result of the relative phase stability between $\mathbf{a}_1$ and $\mathbf{a}_{int}$ signals is shown in Fig. . As expected, these results demonstrate the much higher phase stability of the single-source configuration compared to the dual-source method [64]. Moreover, as shown in Fig. 36, the model predictions, plotted as black dashed line, accurately correlate with the experimentally found phase fluctuations for the dual-source method.

5 Uncertainties in on-wafer measurements

5.1 Introduction

The evaluation of uncertainties in VNA measurements is a challenging task because of

1. the multivariate nature of the measurand. S-parameters are two-dimensional quantities, expressed either in magnitude and phase or complex-valued with real and imaginary components.

2. the multistep measurement process with calibration and error correction. This leads to an elaborate measurement model.

3. The relatively large number of data points. It is not unusual to collect data at several hundred frequency points and the uncertainty might show a pronounced frequency dependence.

There has been significant progress in the last years to improve uncertainty evaluation in VNA measurements. A supplement [69] of the GUM [70] has been published, specifically dealing with multivariate and complex-valued quantities. This document serves as the basic guideline to determine uncertainties associated with estimates of S-parameters. Just recently a revised version of the EURAMET VNA Guide [28] has been published embracing the principles of the GUM supplement and promoting an uncertainty evaluation based on a measurement model, which represents the entire measurement process and takes quantities influencing the measurement into account. The EURAMET VNA Guide has been primarily written for coaxial measurements, but its basic principles are applicable for on-wafer measurements as well.

An essential part of uncertainty evaluation is the characterisation of influence quantities. This is discussed in some detail in [28] and the same influences need to be considered in on-wafer measurements too. The characterisation procedures given in [28] can generally be applied with little and straightforward modifications. Under connector repeatability different contributions specific to on-wafer positioning and alignment can be summarized, by performing the following characterizations

1. Repeated connections by keeping probes at same position and moving sample in z.

2. Repeated positioning of probe station for each measurement of same standard at same position.

3. Repeated measurement of same standard at slightly different contact points.

On-wafer measurements are affected more by crosstalk compared to coaxial measurements. The effect is strongly dependent on the distance between probes and therefore on the device under test. One way to acknowledge this effect in the uncertainty evaluation is to come up with an additional DUT uncertainty (as shown in the example in the next section), which can be characterized by the transmission coefficient as a function of distance when measuring two one-port standards. Other approaches might be possible.

In the multivariate case the propagation of measurement uncertainties is more involved, see [71]. If correlations should be taken into account properly it is unavoidable to use specialized software. Suitable software solutions, which are able to handle the uncertainty propagation of complex-valued quantities, are available nowadays [72, 73]. These tools provide general frameworks to realize custom-built implementations of S-parameter uncertainty evaluation. For software solutions that are specifically targeting S-parameter measurements see [12, 74]. These solutions already contain the VNA measurement models and support different calibration algorithms, i.e. programming is not necessary.

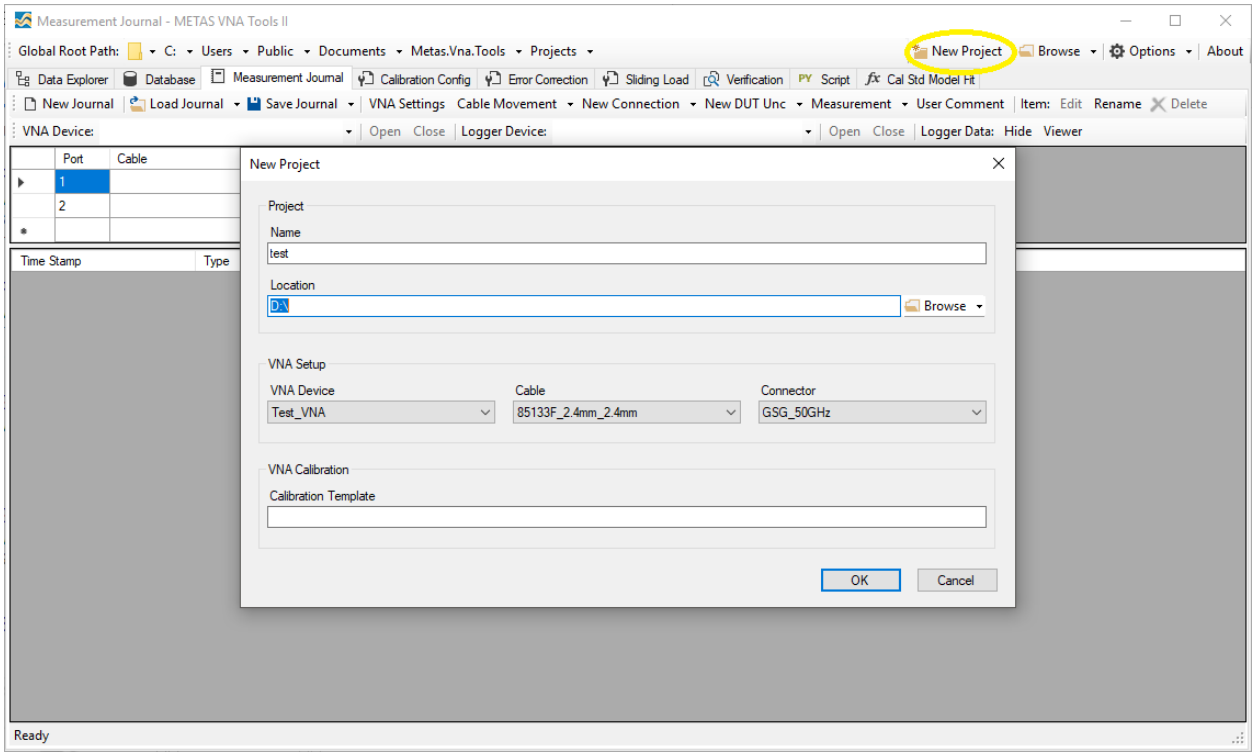

Figure 37 Basic setup of new project.

One of these solutions is the software VNA Tools II. Originally developed for coaxial VNA measurements it has been recently extended to support on-wafer measurements as well. In the next section the different steps in an on-wafer measurement with VNA Tools II are explained. An overview of the features of VNA Tools II is given in [75]. Further information and user guidance can be found at [12]. Measurement models, calculations and data formats are documented in publicly available documents, which can be downloaded from the website as well.

5.2 VNA Tools II on-wafer example

5.2.1 Introduction

This example shows the use of the VNA Tools software to perform an SOLT on-wafer measurement. The following typical steps are covered:

1. Definition of a new project.
2. Collection of measurement data and record of the measurement process in the Measurement Journal.
3. Configuration of VNA calibration and computation of error coefficients.
4. Error correction of the raw measurement data.
5. Use of data explorer for visualization.

5.2.2 New project and basic definitions

The first step in VNA Tools II is to define a new project. This defines the location, where the data files of the project are stored and some basic settings. It can be specified in the navigation bar on the top. By selecting `New Project` the dialog in Fig. 37 opens. The entries under `Name` and `Location` will define the global root path. Under `VNA Setup` a VNA

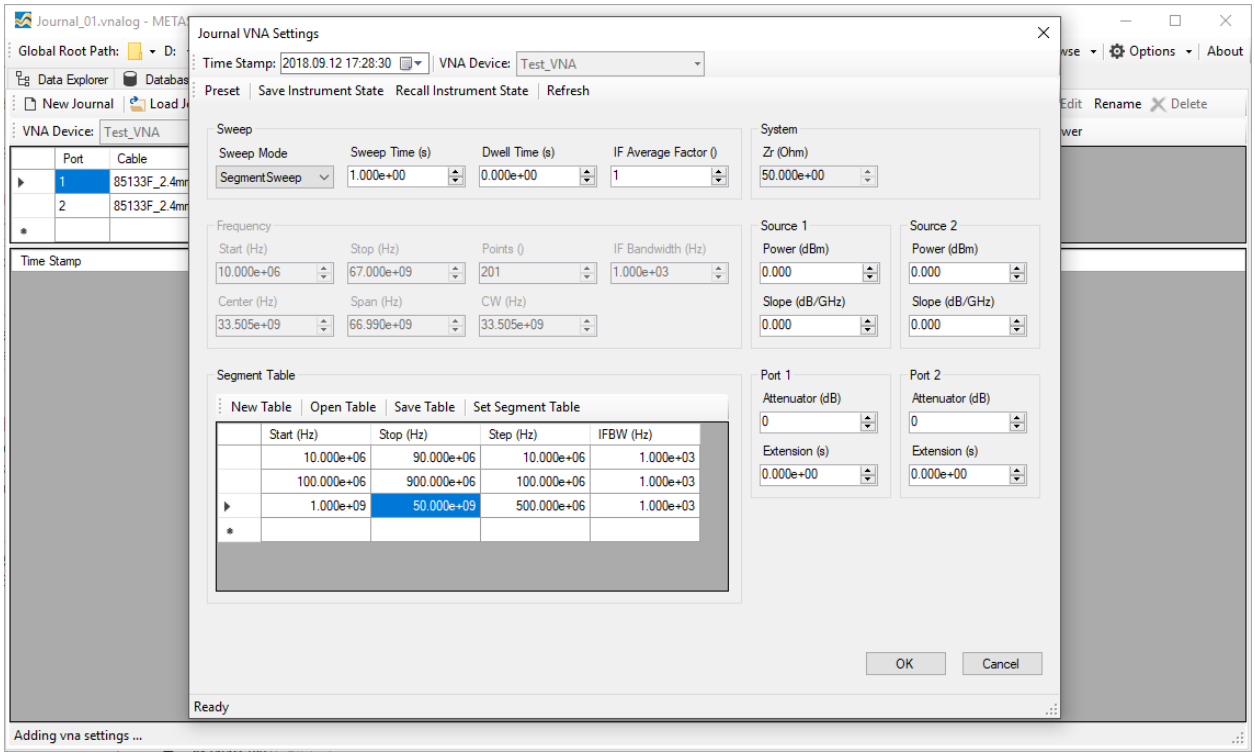

Figure 38 VNA Settings.

device, test port cable and probe can be selected. In this example a Test VNA is selected, which usually serves just for test purposes. Clicking `OK` will store these entries and close the dialog.

By selecting `VNA Settings` VNA device parameters can be set in a separate dialog, see Fig. 38. The dialog allows to set some parameters and specify the sweep mode, which in this case is a segmented sweep. The sweep is defined by the entries in the segment table, e.g. the maximum frequency is set to 50 GHz and the IFBW to 10 Hz. By clicking `Set Segment Table` the values will be saved to the VNA. By clicking `OK` the VNA Settings are saved to the measurement journal.

Selecting `Custom DUT Unc` in `New DUT Unc` opens the dialog in Fig. 39 to account for crosstalk between probes during measurements. The values entered as transmission uncertainties are dependent on distance and probe type. In this example all measurements are done on the same substrate, with the same probes and the same distance between probes. The size of the uncertainty contribution is therefore the same for each measurement, but uncorrelated when changing from one standard to another. When clicking `OK` the first two entries, VNA Settings and Custom DUT Unc can be seen in the measurement journal.

5.2.3 Measurements

For the simultaneous measurement of the opens of both ports an uncertainty contribution due to crosstalk between probes needs to be taken into account. This is generated by clicking on `New DUT Unc` and selecting from the drop-down menu `Custom`, see Fig. 40. Increase the number in the `Index` field when measuring a new standard. Use same index if measuring the same standard again. This keeps track of the correlation. Click `OK` to generate the uncertainty contribution. It will show up in the measurement journal. To start the measurement the boxes under `New Connection` need to be checked for both ports, see Fig. 41. Because both probes are kept at a fixed position during the measurements no uncertainty contributions due to cable movement need to be accounted for. The boxes under `Cable Movement`

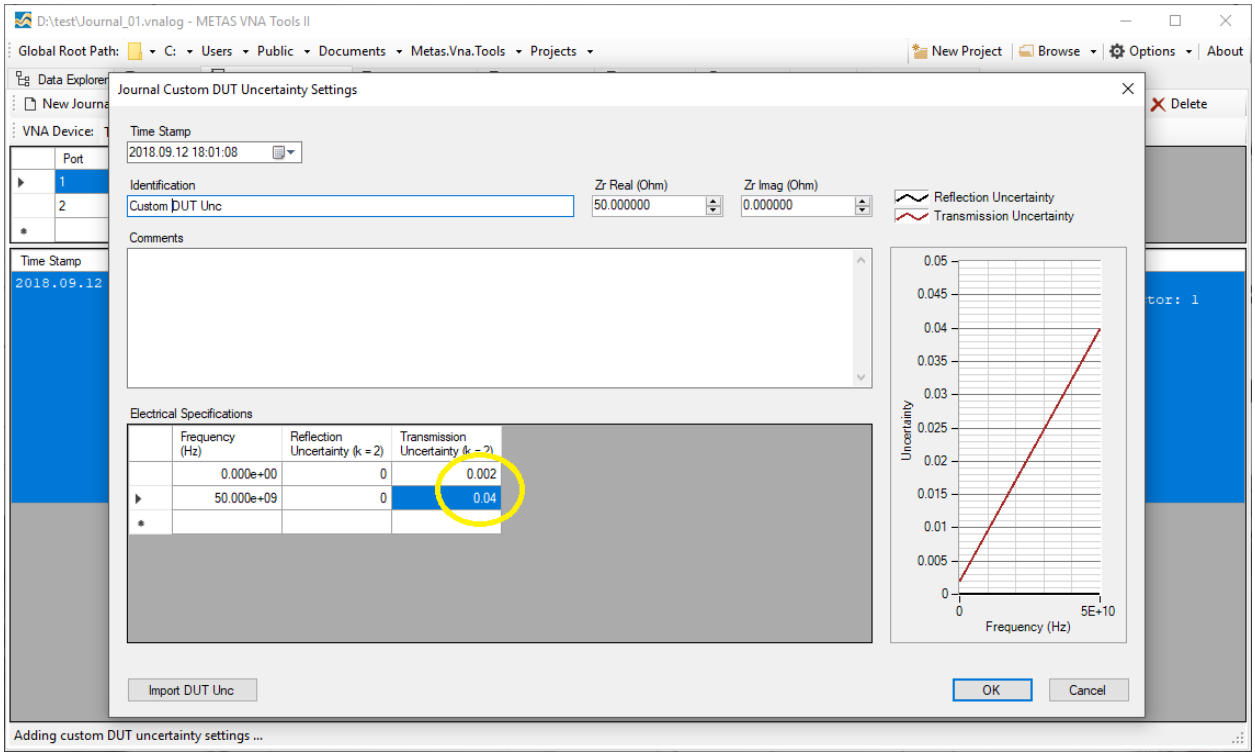

Figure 39 Setting custom DUT uncertainty.

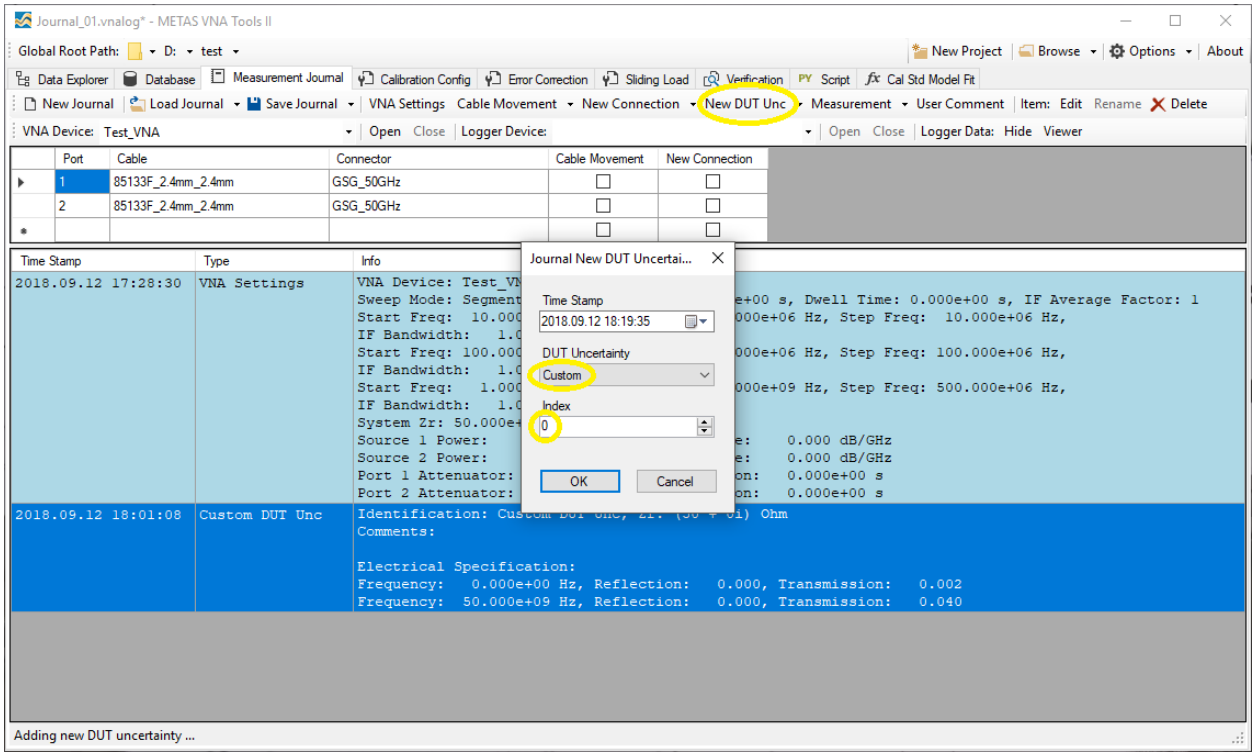

Figure 40 Selecting custom DUT uncertainty to create an uncertainty contribution due to cross talk.

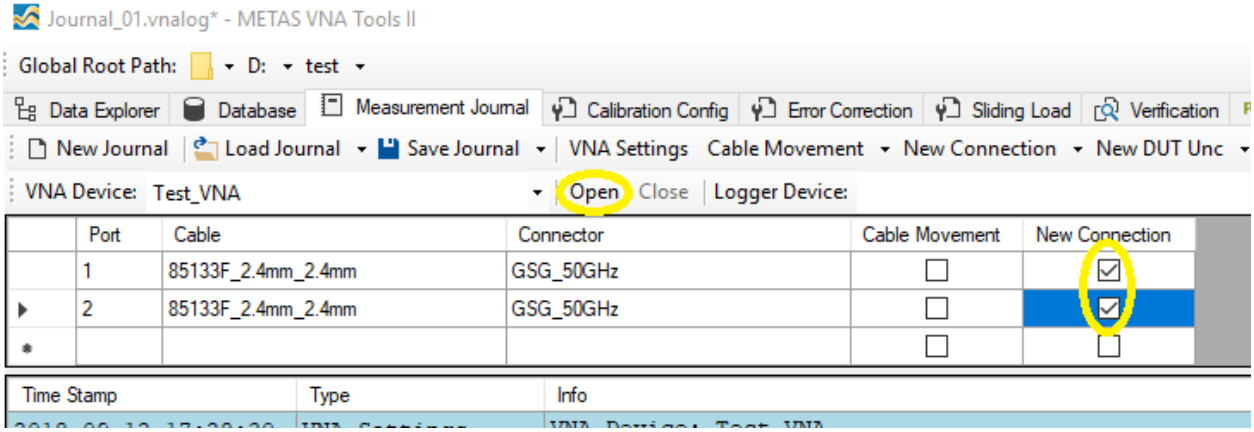

Figure 41 Cable movements and new connections before measurements are indicated by checking boxes.

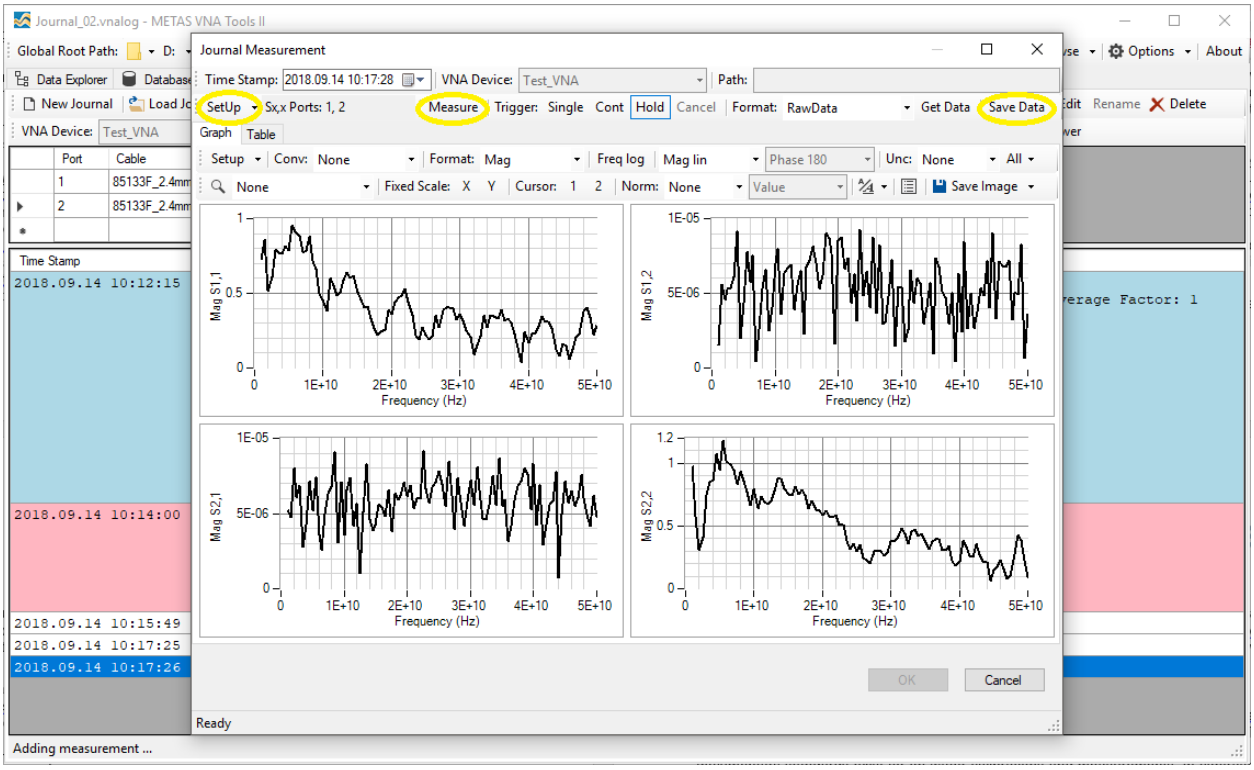

Figure 42 Measurement dialog box.

therefore remain unchecked. As soon as one of the probes is moved before a measurement the corresponding box needs to be checked. Selecting `Open` next to the `VNA Device` field, see Fig. 41, will open the connection to VNA. Selecting `Measurement` opens the dialog in Fig. 42. In this dialog the setup needs to be specified in the drop-down menu `Setup`, in this case `Sx,x Ports: 1,2`. Clicking on `Measure` will initiate the measurement and the data will be displayed in the graph. The measurement of the open in this example is showing noise contributions for S_{21} and S_{12}. When satisfied with the measurement the data can be stored with `Save Data`. The same procedure will be repeated for the measurement of short, load and through. In the final measurement step the DUT, in this case a line, is measured, see Fig. 43. When the measurements are finished the measurement journal can be saved by clicking `Save Journal`.

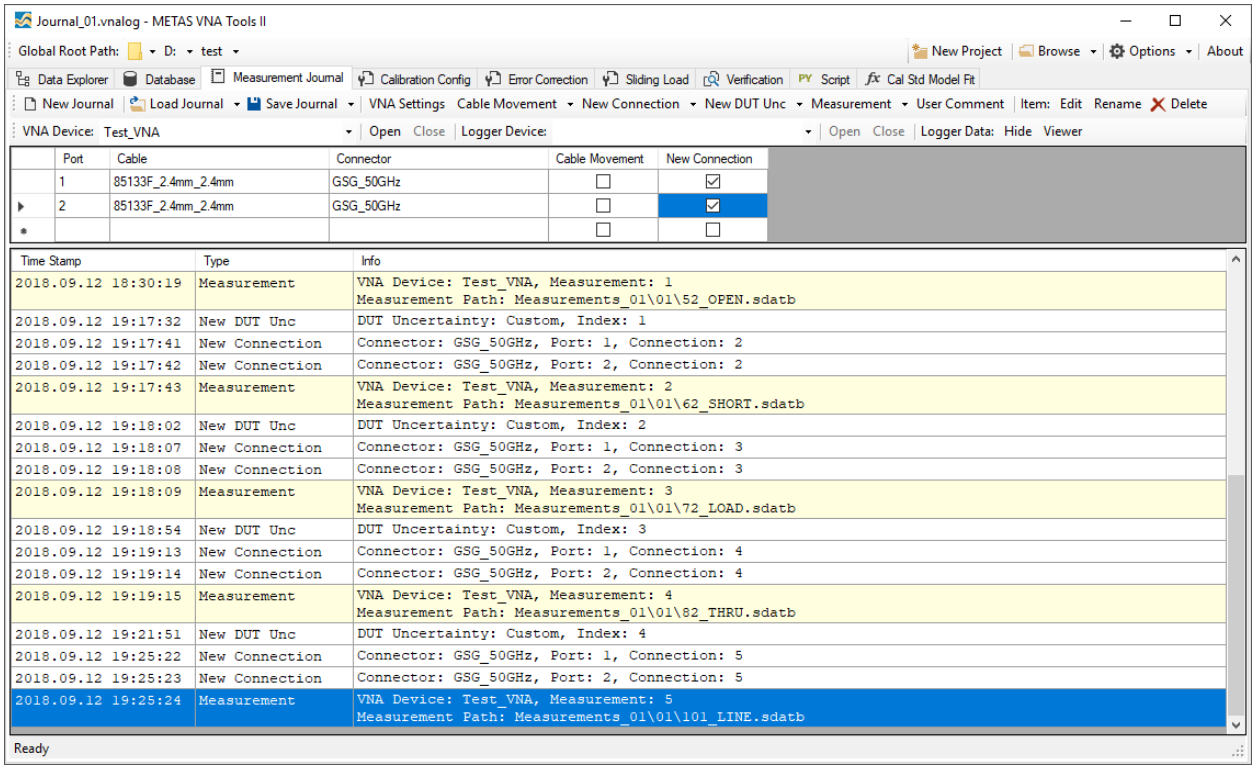

Figure 43 After final measurement of DUT performed.

5.2.4 Calibration configuration

After clicking on the tabs `Calibration Config` and `New Config` we select SOLT in the drop-down menu as the calibration type, see Fig. 44 After clicking on `OK` the template can be filled in by linking measurement data, in column `Raw Measurement`, and definitions, in column `Definition`, of the calibration standards, see Fig. 45. In the same dialog the measurement journal needs to be specified, in this case Journal_01.vnalog. With `Save Config` the calibration configuration can be saved to a file SOLT_01.calcfg. By clicking on `Start Computation` the error coefficients are computed and stored as SOLT_01.calb.

5.2.5 Error correction

After selecting the tab `Error Correction` the dialog in Fig. 46 opens The fields need to be populated with the location of measurement journal, error coefficients, raw measurements and output folder. With `Save Config` the configuration will be saved to a file SOLT_01.corcfg. Clicking on `Start Computation` will initiate the error correction and store error corrected S-parameter files in SOLT_01_out.

5.2.6 Data Explorer

By selecting the tab `Data Explorer` the measurement results can be visualized as shown in Fig. 47. The Data Explorer has a data browser on the left. By clicking on data files they will be displayed on the right. There are different basic display modes, which can be selected with `Graph`, `Table`, `Point` and `Covariance`. As for setup and format there are various selections as well. Uncertainties can be tuned on or off. Data can as well be exported to other file formats.

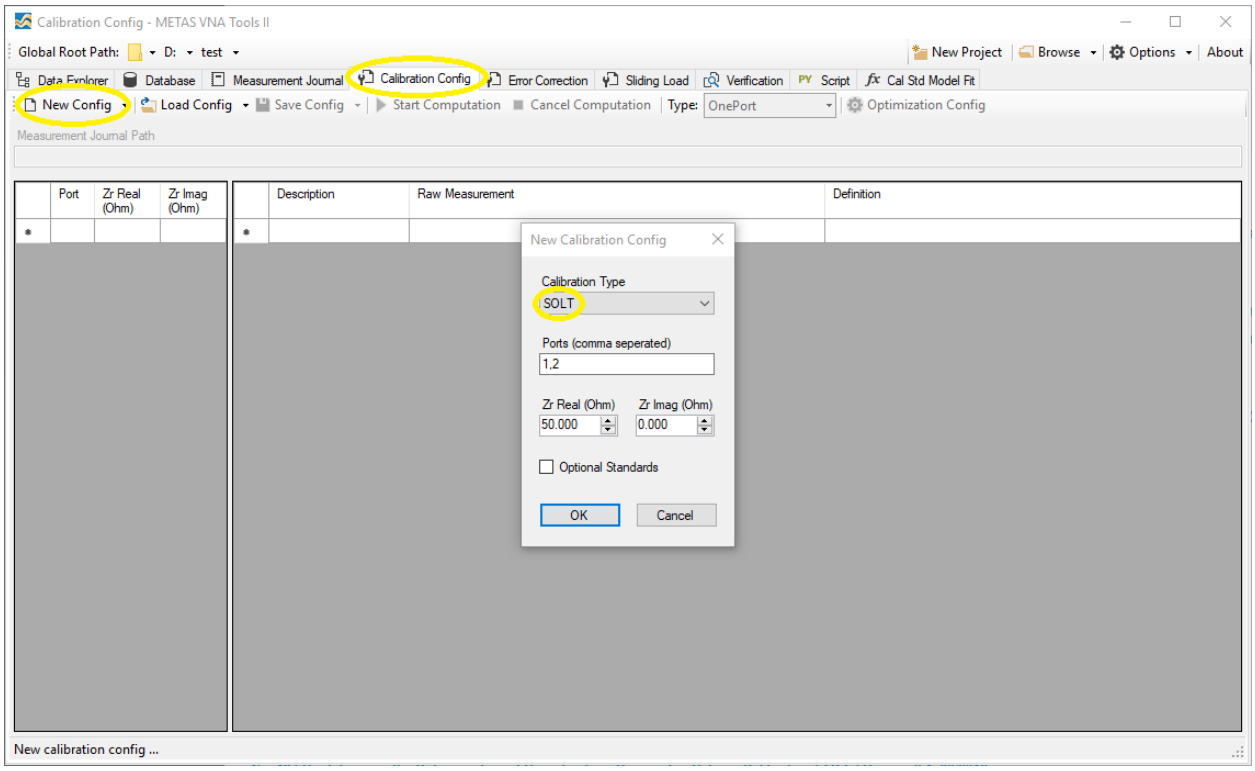

Figure 44 Selection of calibration type.

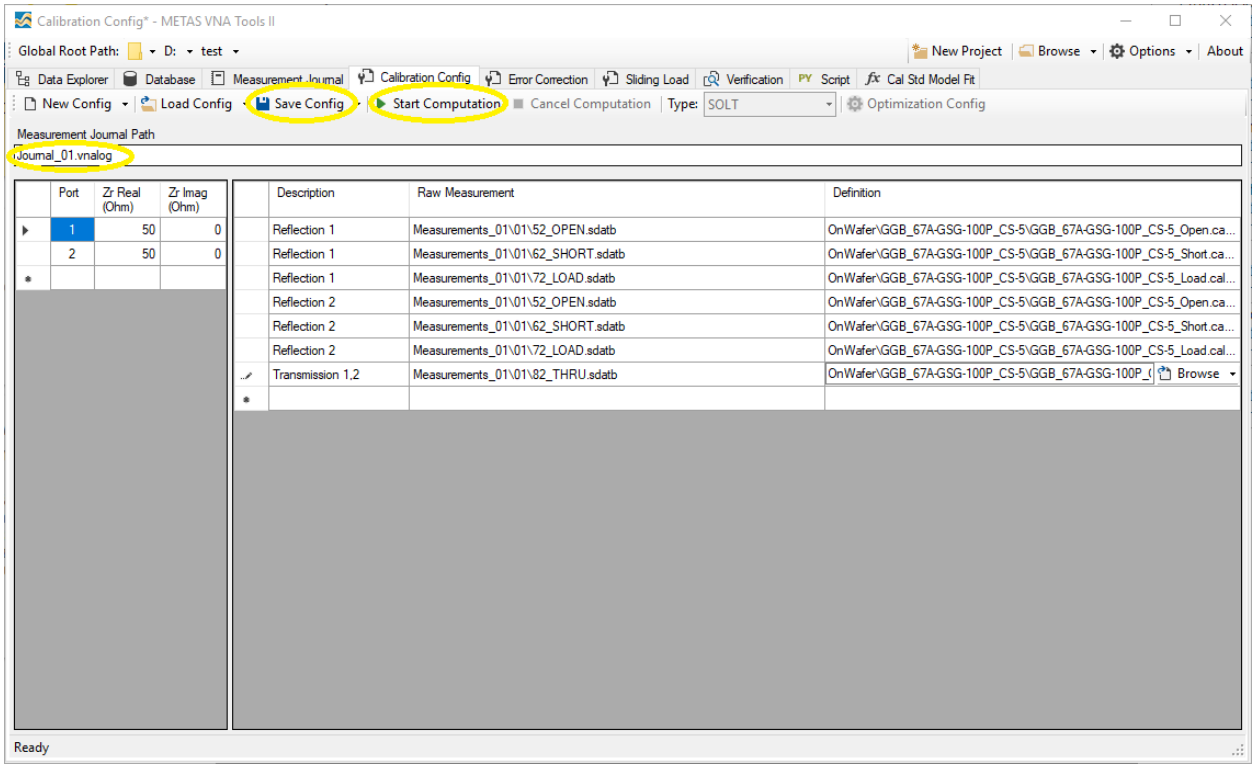

Figure 45 Calibration Configuration.

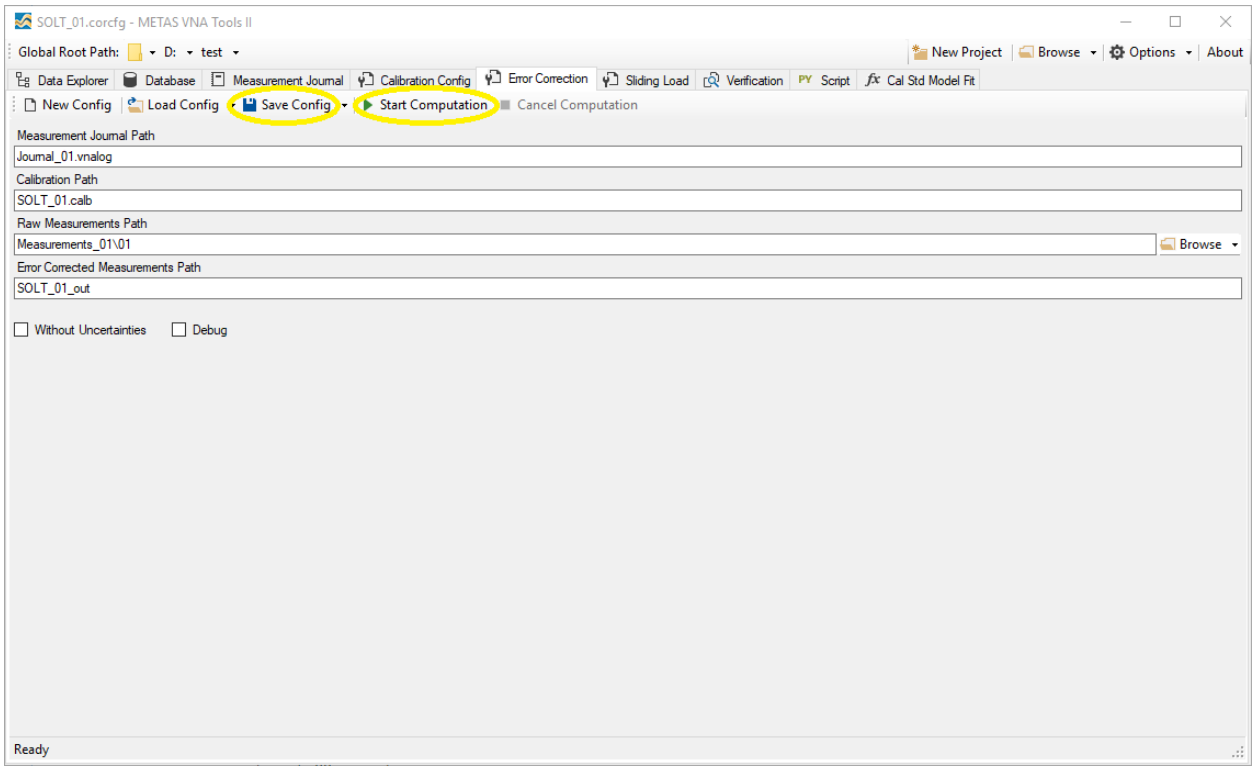

Figure 46 Error Correction.

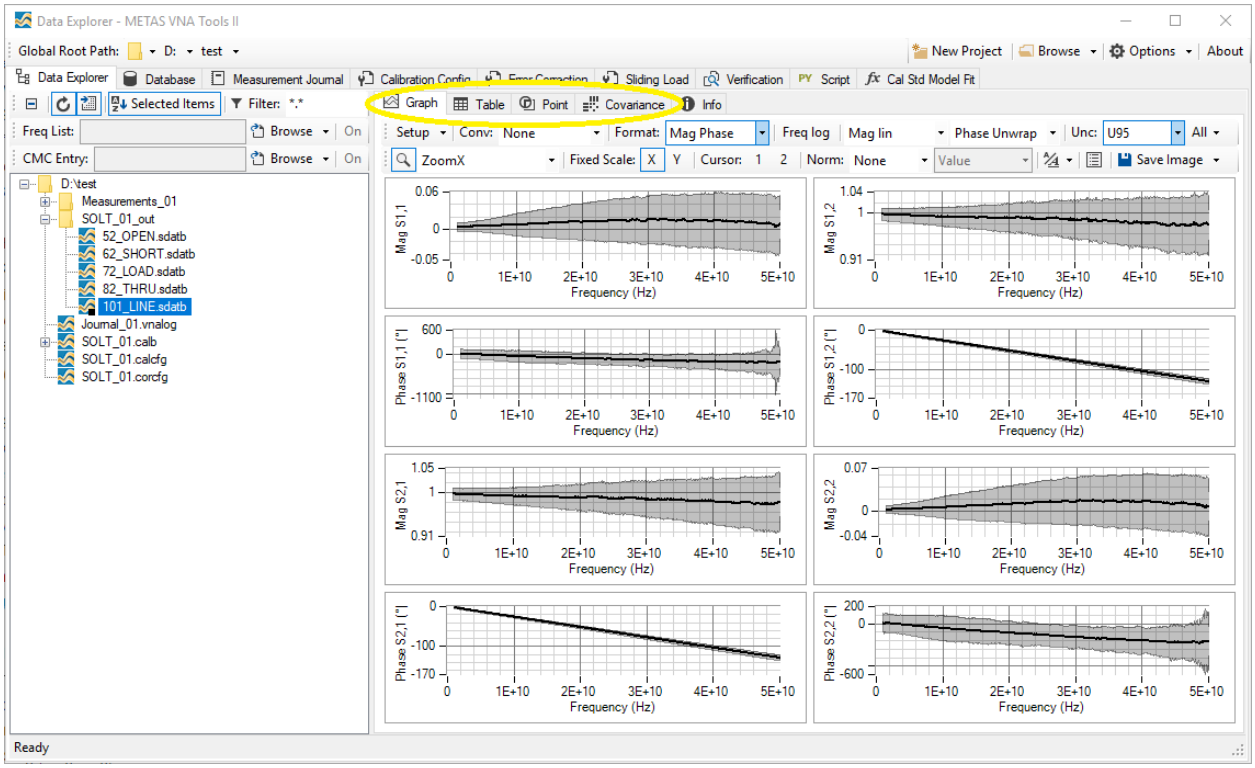

Figure 47 Data Explorer.

5.3 Uncertainty budget examples

In the following uncertainty results for three typical devices on a fused silica substrate are shown for the case of a multiline TRL calibration (from [11]), covering a large portion of the impedance range measurable by a VNA: a nominally 15 dB matched attenuator (termed 'attenuator'), a 7065 μm-long mismatched line (termed 'mismatch'), and a 2-port open (high-reflect device, termed 'open')).

5.3.1 Expanded uncertainties

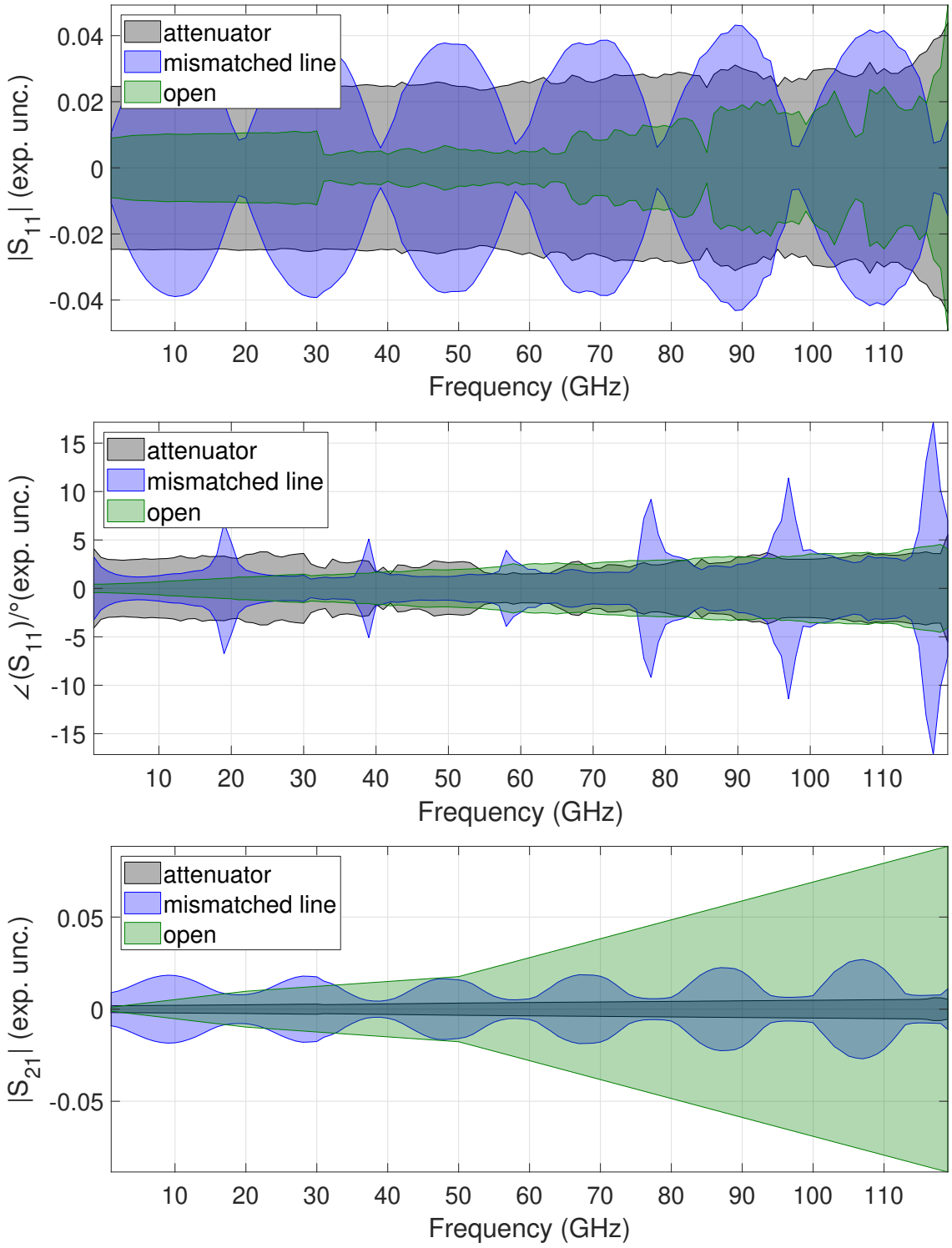

Figure 48 Expanded uncertainty intervals at a coverage probability of 95% (k=2).

Figure 48 shows expanded uncertainty intervals at a coverage probability of 95% (k=2) of reflection and transmission S-parameters for all three devices considered. All S-parameters were normalized to the system reference impedance of 50 Ω.

To this end, the characteristic impedance Z_0 of the line standards was determined from the measured propagation constant γ using the low-loss approximation of constant capacitance per unit length C and negligible conductance per unit length G described in [76], i.e. $Z_0 = \gamma/(j\omega C + G) \approx \gamma/(j\omega C)$.

The capacitance per unit length C is treated as independent uncertain quantity in our current budget calculations, as it can be determined either from measurement [77] or from model calculations. Here, we used the models of [78] and [45], which both gave nearly identical results. Surface roughness effects were negligible because of the low value of R_q.

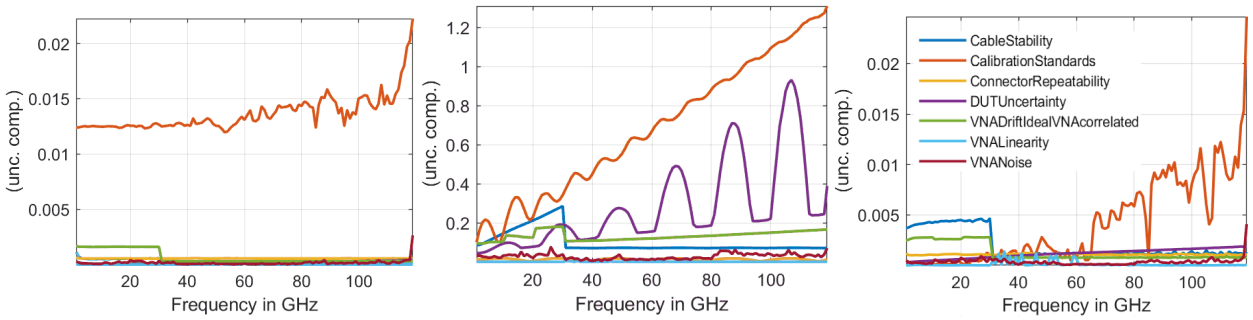

(a) $|S_{11}|$ of attenuator device. **(b)** $\angle S_{21}$ of mismatched line device. **(c)** $|S_{11}|$ of open device.

Figure 49 Uncertainty budget components of three devices over frequency.

5.3.2 Uncertainty budgets

For the three selected devices, exemplary uncertainty budgets for selected measurement quantities are shown in Fig. 49. In most cases shown the budget is dominated by the calibration standard uncertainties (red curve), which include the uncertainties of the renormalization step to 50 Ω. Within the calibration standard uncertainties, the uncertainties in C and in ε_{r} are usually the dominant factor. The latter is also a consequence of the rather conservative uncertainty estimation for ε_{r} in [11]. However, for certain constellations, also the uncertainties in the line lengths can be the biggest contributor, e.g in the case of $\angle S_{21}$ of the mismatched line.

For the open device, cable stability becomes dominant in the budget of $|S_{11}|$ up to 30 GHz. For all three devices and the quantities shown, VNA drift has a significant impact at low frequencies up to 30 GHz, which is a direct consequence of the VNA architecture used. In the magnitude and phase of S_{21}, the influence of the DUT uncertainty approximation becomes significant at increasing frequencies for medium- to high-reflect devices. This becomes also evident from the mismatch and open results shown in Fig. 48 (bottom graph).

In summary, the graphs shown in Fig. 49 together with corresponding graphs of sub-budgets (e.g. for calibration standard uncertainties, not shown here) allow for a better understanding of the impact of the different input quantities. This can provide immediate understanding which quantities one needs to focus on in order to achieve lower uncertainties.

6 Conclusions and Outlook

This Best Practice Guide represents a summary of state-of-the-art recommendations for performing on-wafer measurements together with a selection of the latest research results obtained over a period of three years during the PlanarCal project. In this project, traceability up to 110 GHz has been achieved for the case of multiline TRL calibrations on membrane technology and fused silica substrates. This traceability path can be applied to other configurations of measurement hardware, substrate materials and probes, as long as single-mode propagation is ensured. Some of the uncertainties shown in this Guide can be significantly reduced by improving on the measurements of the wideband frequency-dependent material properties, which is a subject of future research.

The work performed in PlanarCal also lays the foundations for establishing traceability in adjacent fields such as active device characterization, multiport, differential and pulsed measurements. One obvious extension of the PlanarCal work is to address traceability at frequencies beyond 110 GHz, where a number of additional challenges need to be solved. The latter topic will be addressed in a new EMPIR follow-up project, provided funding will be available.

Nanodevice challenges are found in the context of emerging technologies that include quantum confinement, spin transport, molecular or correlated materials, which place increasingly stringent requirements on metrology. Accurate measurements of dimensions, characterization of materials and reliable electrical performances of structures and devices are critical for advances in fundamental nanoscience, design of new nanomaterials, and progresses in manufacturing of next-generation nanodevices. To reach this objective in the field of high frequency characterizations, it is necessary to overcome some bottlenecks to fit the microwave measurement setup to the nano-world, particularly those concerned by the scale and impedance mismatches between the usual microwave instruments and the nanometric devices.

7 Acknowledgements

The authors acknowledge support by the European Metrology Programme for Innovation and Research (EMPIR) Project 14IND02 “Microwave measurements for planar circuits and components”. The EMPIR program is co-financed by the participating countries and from the European Union’s Horizon 2020 research and innovation program.

References

[1] European Metrology Programme for Innovation and Research JRP Number 14IND02, "Microwave measurements for planar circuits and components," https://planarcal.ptb.de.

[2] E. Lourandakis, *On-wafer Microwave Measurements and De-embedding.* Artech House, 2016.

[3] S. A. Wartenberg, *RF measurements of die and packages.* Artech House, 2002.

[4] L. Martens, *High-frequency characterization of electronic packaging.* Springer Science & Business Media, 2013, vol. 1.

[5] R. B. Marks, "A Multiline Method of Network Analyzer Calibration," *IEEE Trans. on Microwave Theory and Techniques*, vol. 39, no. 7, pp. 1205–1215, 1991.

[6] F. J. Schmückle, T. Probst, U. Arz, G. N. Phung, R. Doerner, and W. Heinrich, "Mutual interference in calibration line configurations," in *2017 89th ARFTG Microwave Measurement Conference (ARFTG)*, June 2017, pp. 1–4.

[7] G. N. Phung, F. J. Schmückle, R. Doerner, W. Heinrich, T. Probst, and U. Arz, "Effects Degrading Accuracy of CPW mTRL Calibration at W Band," in *2018 IEEE/MTT-S International Microwave Symposium - IMS*, June 2018, pp. 1296–1299.

[8] G. N. Phung, F. J. Schmückle, R. Doerner, T. Fritzsch, and W. Heinrich, "Impact of parasitic coupling on multiline TRL calibration," in *2017 47th European Microwave Conference (EuMC)*, Oct 2017, pp. 835–838.

[9] M. Spirito, C. D. Martino, and L. Galatro, "On the Impact of Radiation Losses in TRL Calibrations," in *2018 91st ARFTG Microwave Measurement Conference (ARFTG)*, June 2018, pp. 1–3.

[10] U. Arz, S. Zinal, T. Probst, G. Hechtfischer, F. J. Schmückle, and W. Heinrich, "Establishing traceability for on-wafer S-parameter measurements of membrane technology devices up to 110 GHz," in *2017 90th ARFTG Microwave Measurement Symposium (ARFTG)*, Nov 2017, pp. 42–45.

[11] U. Arz, K. Kuhlmann, T. Dziomba, G. Hechtfischer, G. Phung, F. J. Schmückle, and W. Heinrich, "Traceable Coplanar Waveguide Calibrations on Fused Silica Substrates up to 110 GHz," *IEEE Transactions on Microwave Theory and Techniques*, 2019. [Online]. Available: https://ieeexplore.ieee.org/stamp/stamp.jsp?tp=&arnumber=8693763

[12] METAS VNA Tools, available at www.metas.ch/vnatools.

[13] M. Zeier, J. Hoffmann, and M. Wollensack, "Metas.UncLib — A measurement uncertainty calculator for advanced problems," *Metrologia*, vol. 49, no. 6, p. 809, 2012.

[14] D. K. Rytting, *Network Analyzer Error Models and Calibration Methods*, 62nd ARFTG Conference Short Course Notes, December 2-5, 2003, Boulder, CO.

[15] H. Eul and B. Schiek, "Thru-Match-Reflect: One Result of a Rigorous Theory for De-Embedding and Network Analyzer Calibration," in *1988 18th European Microwave Conference*, Sept 1988, pp. 909–914.

[16] A. Davidson, K. Jones, and E. Strid, "LRM and LRRM Calibrations with Automatic Determination of Load Inductance," in *36th ARFTG Conference Digest*, vol. 18, Nov 1990, pp. 57–63.

[17] G. F. Engen and C. A. Hoer, "Thru-Reflect-Line: An Improved Technique for Calibrating the Dual Six-Port Automatic Network Analyzer," *IEEE Transactions on Microwave Theory and Techniques*, vol. 27, no. 12, pp. 987–993, Dec 1979.

[18] L. F. Tiemeijer, R. J. Havens, A. B. M. Jansman, and Y. Bouttement, "Comparison of the "pad-open-short" and "open-short-load" deembedding techniques for accurate on-wafer RF characterization of high-quality passives," *IEEE Transactions on Microwave Theory and Techniques*, vol. 53, no. 2, pp. 723–729, Feb 2005.

[19] L. Galatro and M. Spirito, "Analysis of residual errors due to calibration transfer in on-wafer measurements at mm-wave frequencies," in *2015 IEEE Bipolar/BiCMOS Circuits and Technology Meeting - BCTM*, Oct 2015, pp. 141–144.

[20] S. Padmanabhan, L. Dunleavy, J. E. Daniel, A. Rodriguez, and P. L. Kirby, "Broadband Space Conservative On-Wafer Network Analyzer Calibrations With More Complex Load and Thru Models," *IEEE Transactions on Microwave Theory and Techniques*, vol. 54, no. 9, pp. 3583–3593, Sept 2006.

[21] U. Arz and D. Schubert, "Coplanar microwave probe characterization: Caveats and pitfalls," in *67th ARFTG Microwave Measurement Conference (ARFTG)*, June 2006, pp. 214–218.

[22] T. Probst, S. Zinal, R. Doerner, and U. Arz, "On the Importance of Calibration Standards Definitions for On-Wafer Measurements up to 110 GHz," in *2018 91st ARFTG Microwave Measurement Symposium (ARFTG)*, Jun 2018, pp. 106–109.

[23] M. Spirito, L. Galatro, G. Lorito, T. Zoumpoulidis, and F. Mubarak, "Improved RSOL planar calibration via EM modelling and reduced spread resistive layers," in *2015 86th ARFTG Microwave Measurement Conference*, Dec 2015, pp. 1–5.

[24] L. Chen, C. Zhang, T. J. Reck, C. Groppil, A. Arsenovic, A. Lichtenberger, R. M. Weikle, and N. S. Barker, "Terahertz micromachined on-wafer probes: Repeatability and robustness," in *2011 IEEE MTT-S International Microwave Symposium*, June 2011, pp. 1–4.

[25] M. Wollensack, J. Hoffmann, J. Ruefenacht, and M. Zeier, "VNA Tools II: S-parameter uncertainty calculation," in *79th ARFTG Microwave Measurement Conference*, June 2012, pp. 1–5.

[26] FormFactor, Inc., "Cascade WinCal XE," https://www.formfactor.com/product/probes/calibration-tools/wincal-xe/.

[27] M. Wollensack, J. Hoffmann, D. Stalder, J. Ruefenacht, and M. Zeier, "VNA tools II: Calibrations involving eigenvalue problems," in *2017 89th ARFTG Microwave Measurement Conference (ARFTG)*, June 2017, pp. 1–4.

[28] *Guidelines on the Evaluation of Vector Network Analysers (VNA)*, Calibration guide no. 12, version 3.0 ed., EURAMET, 2018, available at https://www.euramet.org/publications-media-centre/calibration-guidelines/.

[29] D. F. Williams, F. J. Schmückle, R. Doerner, G. N. Phung, U. Arz, and W. Heinrich, "Crosstalk Corrections for Coplanar-Waveguide Scattering-Parameter Calibrations," *IEEE Trans. Microw. Theory Techn.*, vol. 62, no. 8, pp. 1748–1761, Aug 2014.

[30] M. Wollensack and J. Hoffmann, "METAS VNA Tools II - Math Reference V1.8," www.metas.ch, 2017.

[31] T. Probst, R. Doerner, M. Ohlrogge, R. Lozar, and U. Arz, "110 GHz on-wafer measurement comparison on alumina substrate," in *2017 90th ARFTG Microwave Measurement Symposium (ARFTG)*, Nov 2017, pp. 13–16.

[32] D. F. Williams, R. B. Marks, and A. Davidson, "Comparison of On-Wafer Calibrations," in *38th ARFTG Conference Digest*, vol. 20, Dec 1991, pp. 68–81.

[33] D. F. Williams and R. B. Marks, "Compensation for Substrate Permittivity in Probe-Tip Calibration," in *44th ARFTG Conference Digest*, vol. 26, Dec 1994, pp. 20–30.

[34] D. K. Walker and D. F. Williams, "Compensation for geometrical variations in coplanar waveguide probe-tip calibration," *IEEE Microwave and Guided Wave Letters*, vol. 7, no. 4, pp. 97–99, Apr 1997.

[35] A. A. Savin, V. G. Guba, A. Rumiantsev, B. D. Maxson, D. Schubert, and U. Arz, "Adaptive estimation of complex calibration residual errors of wafer-level S-parameters measurement system," in *84th ARFTG Microwave Measurement Conference*, Boulder, USA, 2014, pp. 1–4.

[36] A. A. Savin, "Second-Order Error Correction of a Pre-calibrated Vector Network Analyzer for Wafer-Level Measurements," in *Proceedings of the 47th European Microwave Conference*, Nuremberg, Germany, 2017, pp. 743–746.

[37] *The international vocabulary of metrology - basic and general concepts and associated terms (VIM), 3rd edn.*, BIPM, IEC, IFCC, ILAC, IUPAC, IUPAP, ISO and OIML, 2012, JCGM 200:2012; available at https://www.bipm.org/utils/common/documents/jcgm/JCGM_200_2012.pdf.

[38] *Accuracy (trueness and precision) of measurement methods and results - Part 2: Basic method for the determination of repeatability and reproducibility of a standard measurement method*, International Organization for Standardization, 1994, ISO 5725-2:1994.

[39] R. G. Clarke, C. Li, and N. M. Ridler, "An intra-laboratory investigation of on-wafer measurement reproducibility at millimeter-wave frequencies," in *2017 90th ARFTG Microwave Measurement Symposium (ARFTG)*, Nov 2017.

[40] R. G. Clarke, X. Shang, N. M. Ridler, R. Lozar, T. Probst, and U. Arz, "A comparison of on-wafer scattering-parameter measurements at millimeter-wave frequencies," *submitted to IEEE Microwave and Wireless Components Letters.*

[41] S. A. Wartenberg, "Selected topics in RF coplanar probing," *IEEE Transactions on Microwave Theory and Techniques*, vol. 51, no. 4, pp. 1413–1421, April 2003.

[42] Cascade Microtech, "Application Note AN-1115: Infinity Probe – Mechanical Layout Rules," https://www.cascademicrotech.com/files/INFINITYRULES_APP.pdf.

[43] R. Lozar, M. Ohlrogge, R. Weber, A. Tessmann, A. Leuther, X. Shang, N. Ridler, T. Probst, and U. Arz, "A comparative study between on-wafer and waveguide module S-parameter measurements," *submitted to IEEE Transactions on Microwave Theory and Techniques.*

[44] A. Davidson, E. Strid, and K. Jones, "Achieving greater on-wafer S-parameter accuracy with the LRM calibration technique," in *34th ARFTG Conference Digest*, vol. 16, Nov 1989, pp. 61–66.

[45] F. Schnieder, T. Tischler, and W. Heinrich, "Modeling Dispersion and Radiation Characteristics of Conductor-Backed CPW With Finite Ground Width," *IEEE Transactions on Microwave Theory and Techniques*, vol. 51, no. 1, pp. 137–143, Jan. 2003.

[46] G. Gold and K. Helmreich, "A Physical Surface Roughness Model and Its Applications," *IEEE Transactions on Microwave Theory and Techniques*, vol. 65, no. 10, pp. 3720–3732, Oct 2017.

[47] K. Lomakin, G. Gold, and K. Helmreich, "Analytical Waveguide Model Precisely Predicting Loss and Delay Including Surface Roughness," *IEEE Transactions on Microwave Theory and Techniques*, vol. 66, no. 6, pp. 2649–2662, June 2018.

[48] G. Gold and K. Helmreich, "Modeling of transmission lines with multiple coated conductors," in *2016 46th European Microwave Conference (EuMC)*, Oct 2016, pp. 635–638.

[49] K. Daffé, G. Dambrine, F. von Kleist-Retzow, and K. Haddadi, "RF wafer probing with improved contact repeatability using nanometer positioning," in *2016 87th ARFTG Microwave Measurement Conference (ARFTG)*, May 2016, pp. 1–4.

[50] Q. Yu, M. F. Bauwens, C. Zhang, A. W. Lichtenberger, R. M. Weikle, and N. S. Barker, "Improved Micromachined Terahertz On-Wafer Probe Using Integrated Strain Sensor," *IEEE Transactions on Microwave Theory and Techniques*, vol. 61, no. 12, pp. 4613–4620, Dec 2013.

[51] T. M. Wallis, A. Imtiaz, H. Nembach, K. A. Bertness, N. A. Sanford, P. T. Blanchard, and P. Kabos, "Calibrated broadband electrical characterization of nanowires," in *2008 Conference on Precision Electromagnetic Measurements Digest*, June 2008, pp. 684–685.

[52] L. Nougaret, G. Dambrine, S. Lepilliet, H. Happy, N. Chimot, V. Derycke, and J.-P. Bourgoin, "Gigahertz characterization of a single carbon nanotube," *Applied Physics Letters*, vol. 96, no. 4, p. 042109, 2010. [Online]. Available: https://doi.org/10.1063/1.3284513

[53] B. A. Lengyel, "A Michelson-Type Interferometer for Microwave Measurements," *Proceedings of the IRE*, vol. 37, no. 11, pp. 1242–1244, Nov 1949.

[54] M. Randus and K. Hoffmann, "A simple method for extreme impedances measurement," in *2007 70th ARFTG Microwave Measurement Conference (ARFTG)*, Nov 2007, pp. 1–5.

[55] ——, "A simple method for extreme impedances measurement - experimental testing," in *2008 72nd ARFTG Microwave Measurement Symposium*, Dec 2008, pp. 40–44.

[56] K. Haddadi and T. Lasri, "Interferometric technique for microwave measurement of high impedances," in *2012 IEEE/MTT-S International Microwave Symposium Digest*, June 2012, pp. 1–3.

[57] H. Bakli and K. Haddadi, "Quantitative determination of small dielectric and loss tangent contrasts in liquids," in *2017 IEEE International Instrumentation and Measurement Technology Conference (I2MTC)*, May 2017, pp. 1–6.

[58] G. Vlachogiannakis, H. T. Shivamurthy, M. A. D. Pino, and M. Spirito, "An I/Q-mixer-steering interferometric technique for high-sensitivity measurement of extreme impedances," in *2015 IEEE MTT-S International Microwave Symposium*, May 2015, pp. 1–4.

[59] H. Votsi, I. Roch-Jeune, K. Haddadi, C. Li, G. Dambrine, P. H. Aaen, and N. Ridler, "Development of a reference wafer for on-wafer testing of extreme impedance devices," in *2016 88th ARFTG Microwave Measurement Conference (ARFTG)*, Dec 2016, pp. 1–4.

[60] K. Haddadi, A. E. Fellahi, J. Marzouk, S. Arscott, C. Boyaval, T. Lasri, and G. Dambrine, "Robotic on-wafer probe station for microwave characterization in a scanning electron microscope," in *2015 IEEE MTT-S International Microwave Symposium*, May 2015, pp. 1–3.

[61] A. E. Fellahi, K. Haddadi, J. Marzouk, S. Arscott, C. Boyaval, T. Lasri, and G. Dambrine, "Integrated MEMS RF Probe for SEM Station—Pad Size and Parasitic Capacitance Reduction," *IEEE Microwave and Wireless Components Letters*, vol. 25, no. 10, pp. 693–695, Oct 2015.

[62] K. Daffe, J. Marzouk, A. E. Fellahi, T. Xu, C. Boyaval, S. Eliet, B. Grandidier, S. Arscott, G. Dambrine, and K. Haddadi, "Nano-probing station incorporating MEMS probes for 1D device RF on-wafer characterization," in *2017 47th European Microwave Conference (EuMC)*, Oct 2017, pp. 831–834.

[63] M. Randus and K. Hoffmann, "A Method for Direct Impedance Measurement in Microwave and Millimeter-Wave Bands," *IEEE Transactions on Microwave Theory and Techniques*, vol. 59, no. 8, pp. 2123–2130, Aug 2011.

[64] H. Votsi, C. Li, P. H. Aaen, and N. M. Ridler, "An Active Interferometric Method for Extreme Impedance On-Wafer Device Measurements," *IEEE Microwave and Wireless Components Letters*, vol. 27, no. 11, pp. 1034–1036, Nov 2017.

[65] J. C. Tippet and R. A. Speciale, "A Rigorous Technique for Measuring the Scattering Matrix of a Multiport Device with a 2-Port Network Analyzer," *IEEE Transactions on Microwave Theory and Techniques*, vol. 30, no. 5, pp. 661–666, May 1982.

[66] M. Davidovitz, "Reconstruction of the S-matrix for a 3-port using measurements at only two ports," *IEEE Microwave and Guided Wave Letters*, vol. 5, no. 10, pp. 349–350, Oct 1995.

[67] R. R. M. Spirito, F. Mubarak and L. Galatro, *An interferometric IQ-mixer/DAC solution for active, high speed vector network analyser impedance renormalization*, eur. Patent PCT/NL2018/050055, Jan. 25, 2017.

[68] F. Mubarak, R. Romano, L. Galatro, V. Mascolo, G. Rietveld, and M. Spirito, "Noise Behavior and Implementation of Interferometer Module Based Broadband VNA," *submitted to IEEE Transactions on Microwave Theory and Techniques.*

[69] *Evaluation of measurement data - Supplement 2 to the "Guide to the expression of uncertainty in measurement" - Extension to any number of output quantities*, BIPM, IEC, IFCC, ILAC, ISO, IUPAC, IUPAP and OIML, 2011, jCGM 102:2011; available at http://www.bipm.org/en/publications/guides/.

[70] *Evaluation of Measurement Data - Guide to the expression of uncertainty in measurement*, BIPM, IEC, IFCC, ILAC, ISO, IUPAC, IUPAP and OIML, 2008, jCGM 100:2008; available at www.bipm.org/en/publications/guides/gum.html.

[71] M. Garelli and A. Ferrero, "A Unified Theory for S-Parameter Uncertainty Evaluation," *IEEE Trans. Microwave Theory & Tech.*, vol. 60, no. 12, pp. 3844 – 3855, 2012.

[72] M. Zeier, J. Hoffmann, and M. Wollensack, "Metas.UncLib - a measurement uncertainty calculator for advanced problems," *Metrologia*, vol. 49, pp. 809 – 815, 2012.

[73] B. D. Hall, "Object-oriented software for evaluating measurement uncertainty," *Meas. Sci. Technol.*, vol. 24, p. 055004, 2013.

[74] NIST Microwave Uncertainty Framework, available at www.nist.gov/ctl/rf-technology/related-software.cfm.

[75] M. Zeier, J. Hoffmann, J. Ruefenacht, and M. Wollensack, "Contemporary evaluation of measurement uncertainties in vector network analysis," *tm - Technisches Messen*, vol. 84, no. 5, pp. 348 – 358, 2017.

[76] R. B. Marks and D. F. Williams, "Characteristic impedance determination using propagation constant measurement," *IEEE Microwave and Guided Wave Letters*, vol. 1, no. 6, pp. 141–143, June 1991.

[77] D. F. Williams and R. B. Marks, "Transmission line capacitance measurement," *IEEE Microwave and Guided Wave Letters*, vol. 1, no. 9, pp. 243–245, Sept 1991.

[78] W. Heinrich, "Quasi-TEM description of MMIC coplanar lines including conductor-loss effects," *IEEE Transactions on Microwave Theory and Techniques*, vol. 41, no. 1, pp. 45–52, Jan. 1993.